

Development of Digital Architectures for Pixelated Readout of Time Projection Chambers: Q-Pix

Dissertation by
Kevin Keefe

A DISSERTATION SUBMITTED TO THE GRADUATE DIVISION OF THE UNIVERSITY
OF HAWAI'I AT MĀNOA IN PARTIAL FULFILLMENT OF THE REQUIREMENTS FOR
THE DEGREE OF
DOCTOR OF PHILOSOPHY
IN
PHYSICS



KE KULANUI O HAWAI'I MA MĀNOA
Mānoa, Hawai'i

2023

Dissertation Committee:

Kurtis Nishimura

Chairpersons

Jason Kumar, John Learned, Robert Wright, Peter Sadowski, Gary Varner

Keywords: Field Programmable Gate Array, Time Projection Chamber, Neutrino Oscillation

© 2023

Kevin Keefe
ORCID: 0000-0001-5794-879X

All rights reserved except where otherwise noted

ACKNOWLEDGEMENTS

ABSTRACT

The Standard Model (SM) of physics has proven annoyingly successful in past decades, despite several measurements which hint at its incomplete description of nature. The hunt for New Physics (NP) continues at higher energies ($>> 1\text{GeV}$) with larger detectors ($\approx 10kT$). One such future detector is The Deep Underground Neutrino (DUNE) detector. DUNE (as any beam detector) is a combination of two detectors, a near-detector (ND) and a far-detector (FD) for long-baseline neutrino oscillation measurements. The DUNE FD will be a large scale ($\approx 40kT$) Liquid Argon Time Projection Chamber (LArTPC). This 40-kT scale detector requires high precision in both timing ($<< \mu\text{s}$) and spatial resolutions ($\approx 1\text{mm}$) for vertex reconstruction of interesting neutrino events.

This dissertation discusses recent progress and characterization of a novel implementation of a new pixelated LArTPC readout technology. This novel readout is based on a pixel-level charge-integrate-reset circuit: Q-Pix. We present the basic pixel-level readout circuit and the implications of such an implementation when applied at kiloton LArTPC scales. We also show results from the first prototype implementation based on the Q-Pix readout, which was designed using only off-the-shelf electronics. One problem with any pixelated readout is the ability to handle a large number of unique data channels, which in the case of the DUNE FD is $\approx 10^8$. To address the scaling problem, we have developed and tested a modular digital back-end prototype as a proof of concept. In this dissertation, we discuss nominal system requirements to achieve the DUNE-FD APA scale for radiogenic background sensitivity, as well as pixel-level calibration techniques for both timing and charge. Simulations have also been performed based on projected radiogenic backgrounds and high-energy neutrino beamline events, providing initial estimates of the digital back-end requirements in both the quiescent and active states. Finally, based on these results from the simulations and prototypes presented here, we discuss the nominal digital back-end readout constraints of a fully realized Q-Pix implementation for a DUNE-FD APA .

TABLE OF CONTENTS

| | |
|---|-----|
| Acknowledgements | iii |
| Abstract | iv |
| Table of Contents | v |
| List of Illustrations | vii |
| List of Tables | xvi |
| Chapter I: Introduction | 1 |
| 1.1 The State of Things: The Standard Model | 1 |
| 1.2 The Problem: Moving Beyond the Standard Model | 7 |
| 1.3 Modern Tracking Detectors | 10 |
| 1.4 Ways Forward | 12 |
| 1.5 Neutrino Tracking Detectors in the Current Century | 19 |
| 1.6 Future Detectors | 20 |
| Chapter II: A Novel Readout Technique for TPCs: Q-Pix | 23 |
| 2.1 Q-Pix: The Circuit Level Design | 23 |
| 2.2 How Q-Pix fits into a DUNE-FD APA | 34 |
| 2.3 The digital back-end | 36 |
| 2.4 Q-Pix and Light Detection | 40 |
| 2.5 Q-Pix at "Low" Energy: Supernova Studies | 40 |
| Chapter III: The First Prototype: First Resets and Leakage Measurements | 42 |
| 3.1 Simplified Analog Q-Pix: System Design | 42 |
| 3.2 The SAQ Prototype Design | 42 |
| 3.3 Noise Measurements | 43 |
| 3.4 Xenon Gas Lamp Measurements | 45 |
| 3.5 Results and Discussion | 45 |
| Chapter IV: Digital Back-end Viability Studies | 52 |
| 4.1 Digital Design Overview | 52 |
| 4.2 The Digital Finite State Machine | 59 |
| 4.3 The Parameter Space of the Digital System | 60 |
| 4.4 The Digital Back-end problem | 61 |
| 4.5 Constraining the digital back-end Design | 63 |
| 4.6 Frequency Calibration of Local Oscillators | 75 |
| 4.7 The Digital Prototype Design | 79 |
| 4.8 Timing Stability | 83 |
| 4.9 Power and Current Characteristics | 83 |
| 4.10 Analysis of Systematics for Different System Implementations | 83 |
| 4.11 Towards the Integration of the Aggregator Node | 84 |

| | |
|--|-----|
| 4.12 Comments on A Super-DAQ-Node | 84 |
| 4.13 The Back-End Summary | 84 |
| Chapter V: The Q-Pix Back-end and Simulation Studies for Future Q-Pix Prototypes | 85 |
| 5.1 The Tile Simulation Framework | 86 |
| 5.2 The Tile Parameters | 90 |
| 5.3 Simulating The Tile Readout | 93 |
| 5.4 Physical Simulation Studies | 102 |
| 5.5 Neutrino Beam Studies | 110 |
| 5.6 Neutrinos, Backgrounds, and Routing | 114 |
| 5.7 Summary and Further Studies | 115 |
| Chapter VI: Summary and Outlook | 128 |
| Bibliography | 130 |
| Appendix A: SVSC OS1 | 136 |
| Appendix B: SVSC OS2 | 137 |

LIST OF ILLUSTRATIONS

| <i>Number</i> | | <i>Page</i> |
|---------------|--|-------------|
| 1.1 | Image of Fundamental Particles in the Standard Model, taken from CERN website [1]. All known matter and particle interactions involves combinations of the particles shown here. | 3 |
| 1.2 | Image based on the 2008 P5 report [2]. The white text labeled within each frontier describes the search for some physics beyond the SM within that frontier. | 8 |
| 1.3 | Image of a Time Projection Chamber (TPC). Charge is accumulated within the volume as ions are removed from the fiducial volume from another charged ion as it passes through the material. An uniform electric field drifts the free now electrons towards the anode plane. The collection and readout of charge on this anode plane is what is recorded within the detector. Image is taken from [3]. | 12 |
| 1.4 | Representation of the mass hierarchy scales. This is a representation of the two possible orderings of neutrino masses, due to the uncertain sign of m_{13} . It is also interesting to observe that the absolute mass scale is not measured since oscillation measurements only give difference mass squares. Image was taken from [4]. | 18 |
| 1.5 | Representation of the Near and Far Detectors for the DUNE experiment. The Near Detector is located within the image labeled as the Particle Detector. One of the key purposes for the Near Detector is to tag outgoing particles from the proton beam. Image was taken from [5]. | 21 |
| 2.1 | Image of Basic Q-Pix Readout circuit. Currently this front-end circuit is being designed as custom analog ASIC which has 16 channels. Image is taken from [6]. | 24 |
| 2.2 | Example reconstruction of the reset time difference (RTD) based on the Q-Pix readout design. Image is taken from [6]. | 28 |
| 2.3 | Example reconstruction of the reset time difference (RTD) based on the Q-Pix readout design. delta-Q was chosen to be $0.3fC$. Image is taken from [6]. | 29 |

| | | |
|-----|---|----|
| 2.4 | Arbitrary sin-wave based current input. Maximum amplitude is chosen to be close to I_{max} . Reset Charge is chosen to be 1 fC and digital clock frequency of 30 MHz. Since the amplitude is close to the maximum, and the clock measuremts are necessarily discrete, the exact current can not be measured from reset-to-reset. However, an example of a savgol filter is performed on the resets after the fact, shown in blue, with near agreement of the large input. An use-case of this kind of digital filtering would be applied to large current values only, and not for low current inputs, where the pure timestamp difference provides better results. | 31 |
| 2.5 | Reconstruction of Sub figures CDF of charge as a function of time (a) and difference (b). | 32 |
| 2.6 | Image taken from [7], Fig 1.12 of section 1.8. Image shows an overlay the the relevant charge collection wires within a SP DUNE LArTPC. | 35 |
| 2.7 | A simple caption [7] | 36 |
| 2.8 | Images taken from [8]. | 41 |
| 3.1 | The SAQ Setup model based on ???. | 43 |
| 3.2 | The SAQ Setup model based on ???. | 44 |
| 3.3 | The SAQ Setup model based on ???. | 45 |
| 3.4 | Picture of the TPC and DAQ setups at Wellesley University. | 46 |
| 3.5 | The SAQ circuit in a Spice Simulation. The IVC [9] chip chosen as the off-the-shelf integrator for this experiment. The main selection choice for this part is due to its low input bias current $\ll 750$ fA. | 47 |
| 3.6 | An image of the data acquisition board from Digilent, Zybo Z7-20. This board was chosen for its multiple configurable input channels, as well as the Zynq-based archiecture of the onboard FPGA. Additionally, the use of the ethernet provides 1 GB transfer speeds, which is more than sufficient for the application. | 48 |
| 3.7 | The SAQ GUI with real time plotting of incoming resets to the Zybo board. | 49 |
| 3.8 | Drift Current Measurements to go here. | 50 |
| 3.9 | First diffusion measurement in P-10 gas performed at Wellesy University. | 51 |

| | | |
|------|--|----|
| 4.1 | Diagram of the Digital node. The controlling sections of the logic for the digital node are QpixComm, QpixDataProc, QpixRoute, and QpixRegFile. The Comm layer is responsible for routing packets between the physical layer and handles the parsing of incoming data packets. The DataProc layer is responsible for recording timestamp data during a reset from the analog front-end. The RegFile contains configuration information, such as routing. QpixRoute determines the controlling state machine that, based on register configurations, determines what packets are sent to which neighboring nodes. | 53 |
| 4.2 | Example of Datum words and their allocation as currently implemented in the simulation and first prototypes. | 58 |
| 4.3 | Diagram of the Digital node's FSM which determines how to respond to incoming packets. | 59 |
| 4.4 | Example of an Corner Base-Node configuration. The base-node is colored and highlighted in red. | 65 |
| 4.5 | Example of the fully connected routing configuration for a tile (FCT). Each Node represents a digital channel which must be aggregated, and the red and blue connections distinguish directions of communication. The red connection lines indicate pathways away from the base node, whereas the blue lines represent connection paths towards the base-node in the upper-left. | 67 |
| 4.6 | Minimal Occupancy Path of a FCT. This routing path ensures that the number of input connections equal the number of output paths for the node. | 70 |
| 4.7 | Minimal Delay Path of a FCT. This routing path ensures that the minimum number of transactions occur from every node in the FCT to reach the base-node. For any node along any column this is equivalent to the sum of the row and column of that node. | 71 |
| 4.8 | Minimal Routing Path of a FCT. This routing path ensures that the number of input connections equal the number of output paths for the node. | 73 |
| 4.9 | Example of an Edge base-node configuration. The base-node is colored and highlighted in red. | 74 |
| 4.10 | | 80 |
| 4.11 | Example of frequency calibrations for the FPGA Adjacent to the Zybo. | 80 |
| 4.12 | | 81 |
| 4.13 | | 82 |
| 4.14 | | 82 |

| | | |
|-----|---|----|
| 5.1 | Composition of an example 4×4 tile. Each node in the tile represents a digital ASIC which contains two FIFOs. One FIFO is used to store timestamps from reset data, which we refer to as the local FIFO. The other FIFO we call the remote FIFO and is used to store all packet transactions from neighbor nodes. The local FIFO is 48 bits wide, where 32 bits come from the timestamp and 16 bits are from the pixels. The remote FIFO is 60 bits wide, since it must store all relevant bits for the 64 bit packet word, where there are 4 unused bits. | 87 |
| 5.2 | Example timeline for simulation time steps and injected hits. Before the simulation begins hits are added into a Hit Container for each node. When the simulation begins the time is incremented by a single time step ($\tau = 1\mu s$). The time increments until it is larger than the time of any of the injected hits. The values of the timestamps are then moved from the Hits container into the local FIFO, where the timestamp that is recorded is the soonest clock cycle after the "true" time of the injected hit. When the data are ready to be transmitted from the local FIFO, the time is then updated by transaction time. An example of this procedure is shown in Figure 5.3. | 89 |
| 5.3 | Flow chart of the simulation process method which occurs for every simulation time step. The simulation contains a queue of packet transactions. The queue is sorted by ascending time, so that the earliest transaction completed time is processed first. Each transaction contains a packet, a node, and the time the packet arrives. When the node receives the packet, it can optionally create more transactions, depending on the node's state and the packet. Any additional transactions are added to the simulation queue, and are time sorted. The simulation then increments the time for all other nodes within the tile. This procedure repeats until all nodes in the tile research designated time, which for the results presented here is 11 seconds. | 91 |
| 5.4 | Distribution of ASIC frequencies used in the 8×8 tile, and in the example FIFO buffer depths for this chapter. The numbers plotted above each ASIC row and column indicate the relative frequency of this ASIC compared to the nominal 30MHz mean. For example, a number of 112 indicates an ASIC which is 12% faster than 30MHz, a frequency of $\approx 33.6 MHz$. | 94 |

| | | |
|------|---|-----|
| 5.5 | Example of timing ASIC state transitions in the simulation framework. The x-axis represents time in μs , and the different y-axis labels represent different ASICs within a 3×3 tile shown. The y-axis also indicates the relative frequencies of the ASICs in the tile, where the node at (0,0) has the fastest frequency, which is 12% faster than 30 MHz. The blue regions indicate that the ASIC is in the idle state. The first orange state indicates that this ASIC (2,2) received a register request from the aggregator node and is now sending its local data, concluding in the purple state, which is sending the event end word. The Packets drift apart in time as they are sent from slower to faster ASICs. Shown here is the possiblity of packet drift due to asynchronous packet transfers that depends on the magnitude of the frequency drift between neighbor ASICs. | 96 |
| 5.6 | A snake packet transaction example is shown. The broadcast is received by the further node (2,2) and 10 data words are sent, followed by a event end word. Each packet tranverses through all nodes in the tile where remote packets are sent immediately. | 97 |
| 5.7 | A left packet transaction example is shown. The packet transfers begin with the furthest node (2,2) receives a broadcast from the aggregator. The data are then sent to the "left" and then "up" towards the base node, and finally to the aggregator node. | 98 |
| 5.8 | A trunk packet transaction example of two data words and a single event end word is shown. This routing method allows for the fastest possible transaction time since it minimizes the edge lengths between the base node and all other nodes within the tile. In this 3×3 example shown, the base node is at (1,0), or in the middle. | 98 |
| 5.9 | Example local FIFO distribution of a $\approx 3\text{GeV } \nu_e$ event. The numbers over each tile represent the total number of writes which occured to each local FIFO in the array. Even with the lowered resolution (each ASIC accounts for 16 pixels), different tracks are noticeable based on the FIFO depths. The maximum scale for the heatmap is chosen to be 512 resets. | 99 |
| 5.10 | Example of local (a) and Remote (b) fifo depths of the example neutrino event from 5.3 after processing. The colorbar to highlight the maximum number of transactions is used to indicate remote transactions which were happening for 2% of the total readout time of 10 seconds. The node which has the largest remote buffer depth corresponds to the ASIC with the slowest frequency as shown in Figure 5.2. The reason for this excess of buffer depth is due to packet buildup on the slow ASIC. | 100 |

| | | |
|------|---|-----|
| 5.11 | Example of local (a) and Remote (b) fifo depths of the example neutrino event from 5.3 after processing. The ASIC which has the largest remote buffer depth also corresponds to the ASIC with the lowest frequency as shown in Figure 5.2. | 101 |
| 5.12 | Example of local (a) and Remote (b) fifo depths of the example neutrino event from 5.3 after processing. The ASIC which has the largest packet buildup occurs at (4,1). This ASIC also corresponds to the ASIC which has the lowest frequency along the trunk column as shown in Figure 5.2. | 102 |
| 5.13 | A simulated push architecture with 20 injected hits at different times. The time of the injected reset is indicated by the green points. Before the simulation is run a node has its hits injected into a storage (orange) list. Then, at each simulation time step ($\tau_{step} = 1\mu s$) the list is examined to see if a new hit will be written. When a hit is found the relative time of the node can move forward in time to when this packet will be completed in time, while all other writes can occur to the local FIFO. This is why the first local FIFO depth increases initially by one despite 10 nearly adjacent injected hits. On the next time step, the depth then moves to nine; the simulation has sent the first of the 10 packets, and records nine. This example correctly shows a maximum local FIFO depth of nine. | 103 |
| 5.14 | Full 1000 second of radiogenic background source simulation input into all pixels within the APA. A close examination of the resets can reveal the additional resets from the backgrounds which are location dependent. The majority of the uneven distribution of resets occur at the location of the APA bars due to the ^{40}K isotope. | 106 |
| 5.15 | Baseline noise input for the digital simulation from all radiogenic sources and background leakage current. This figure shows the total resets in the 10 second window for the 16×16 tile. The other tile size configurations (4×4 , 8×8 , 10×14) also use these reset data for background noise. All tiles start with the top left node as their origin node. | 107 |
| 5.16 | All 4096 pixels in the 16×16 tile for 1000 seconds of radiogenic data. The y-axis represents a different pixel, and the x-axis is a log-scale time axis with even bin widths. There are two clusters of resets for different time intervals. The first large cluster of resets occurs at $\approx 10^{-7}$ seconds and is due to a single radiogenic decay event causing additional resets. The second large cluster of resets occurs at ≈ 10 seconds. This second cluster of resets is caused from the first reset of a new radiogenic decay event. The ability to perform a charge calibration per pixel may depend on accurately resolving the mean for this "long period" RTD. | 108 |

- 5.17 All 4096 pixels in the 16×16 array for 1000 seconds of radiogenic data. These data are the same as those shown in Figure 5.4, where all pixel RTDs are binned together. There are two clusters of resets on two different time scales. The first cluster of resets near at $\tau_{rtd} \simeq \mathcal{O}(10^{-7})$ is due to events which produce more than one reset. The second cluster of resets near at $\tau_{rtd} \simeq \mathcal{O}(10^1)$ are from a "waiting" period where there is no charge buildup from decays and only background noise. The dominant source of electrons on each pixel is from the ^{39}Ar , with a non-zero contribution from leakage. The leakage current value used in this simulation is 10 aA. 109
- 5.18 Both figures indicate a comparison of the amount of electrons deposited on all pixels in the tile shown in Figure 5.4. Plot (A) represents the total number of electrons on a log scale. As expected, ^{39}Ar contributes the majority of background charge. The leakage current used is 10 aA, and represents about 10% of the total contribution of electrons. This implies that leakage currents from the front circuit which are ≈ 100 aA will contribute nearly as much electrons to the steady-state RTDs as the radiogenic backgrounds. 110
- 5.19 Flux spectrum of neutrinos from the neutrino beam used in this study. This figure is taken from [87]. Highlighted in blue is the reconstructed energy range of neutrinos that are used to seed the interaction with the APA LAr's volume. 112
- 5.20 Rate of CC neutrino interactions based on flavor as a function of true neutrino energy. Figure is taken directly from [10]. Right is shown the neutrino interaction distribution for the forward horn current. The left image is for the reverse horn current. Both images assume an average exposure rate of 1.2 MW from LBNF beam. 113
- 5.21 Same ν_e interaction at Z-position = 180cm, which is in the middle of the drift length of the APA. Image (A) has the incident ν_e momentum rotated upwards ($\theta_z = +90^\circ$). Image (B) has the incident ν_e had momentum along the beam direction ($\theta_z = 0^\circ$). Since there are five different z-positions, and five different θ_z values, each of the 3900 ν_l interactions are repeated 25 times. These two plots show two of those 25 examples. 115

| | | |
|------|---|-----|
| 5.22 | The same ν_e event as the one shown in Figure 5.21-(A). The plot is zoomed into to the region of interest where the bin widths represent the pixels dimensions in the collection plane. The energy of this ν_e was 546.1 MeV, and considering that each reset requires 0.1475 MeV, the maximum number of resets this event could produce is ≈ 4368 . The histogram records 3733 total resets. The most active pixel received 144 resets. When the pixels are binned into ASICs (4×4 pixels) the maximum number resets an ASIC received is 347. | 116 |
| 5.23 | Example ν_e events for different z-position of the vertex with $\theta_z = 0$ held constant. Plot (A) bins the maximum value of local FIFO depth for all 3900 events (ν_l energies between 250 MeV - 10 GeV) for variable z-position and $\theta_z = 0$. Plot (B) shows the running integral for each histogram shown in plot (A). The integral continues until 99% of all events are counted. This process is repeated for all 200 possible parameter choices as discussed in Table 5.5. | 117 |
| 5.24 | Example ν_e events for different θ_z with the vertex held constant with z-position = 180cm. This is a similar plot to Figure 5.23 with the exception that θ_z is varied and the z-position is held constant at z = 180 cm. A striking difference to note here is the run away effect of the large values of θ_z | 118 |
| 5.25 | Comparison of Buffer depths as a function of energy for different parameters of θ_z and z-position. There is a large variance between the true ν_l incident energy and the actual energy deposited in the LAr. This is the reason why only the means are plotted for each energy bin. | 119 |
| 5.26 | A comparison of ASIC resets vs the energy deposited into the LAr. Plot-(B) shows for Z-position=10 cm ends at ≈ 2 GeV since no ν_e events deposit this much energy into the LAr. Both plots indicate that the | 119 |
| 5.27 | Plot-(A) shows a comparison of the energy deposited into the LAr as a function of the input neutrino, which in this case is ν_e . Plot-(B) shows a projection against the y-axis for a single bin. The maximum allowed total energy deposited is limited to the total energy of the input neutrino. However, the lower bound for all energies is still, obviously, zero. Therefore, as the input neutrino energy increases the upper bound also increases. The mean value of Plot-(B) indicates that even for a maximum allowed total energy of 5 GeV the mean (average) energy deposited per event is 1479 MeV. Most interactions deposit less than 2 GeV into the LAr, as shown in Figure 5.27. | 120 |

| | | |
|------|--|-----|
| 5.28 | A relationship between the total number of resets detected in the APA and the energy deposited for ν_e interactions is shown. The solid red line indicates the maximum number of resets that could be measured for a given energy. The small distribution of energies below zero correspond to events that produced no resets. The energy deposited goes above the the threshold limit of 10 GeV. These events carry extra energy from additional leptons which are from pile-up at the DUNE-ND from the FNAL beam. These data are not included in the energy deposited analysis, or in the integrals as shown in Figure 5.21. These high energy deposit events are also not included in the FIFO depth analysis, since these events are beyond the energy range for oscillation measurements. These events are also removed from Figure 5.27. | 121 |
| 5.29 | Comparison of Buffer depths as a function of energy for different parameters of θ_z and z-position. The most important result is shown in Plot-(A), which clearly indicates that only two different parameters account for the distribution of larger local FIFO depths. As expected, θ_z affects the localization of charge over individual ASICs which affect the local FIFO depth. Plot-(B) shows the distribution of resets indicated by different z-positions. Plot-(B) differs in that the second distribution of resets contains elements from each of the different z-positions. | 122 |
| 5.30 | Comparison of Buffer depths as in incoming prototype and horn current direction from neutrino beam. | 123 |
| 5.31 | Information on the 4 by 4 tile. | 124 |
| 5.32 | Information on the 4 by 4 tile. | 125 |
| 5.33 | Information on the 4 by 4 tile. | 126 |
| 5.34 | Information on the 16 by 16 tile. | 127 |
| 6.1 | Full Schematic of the upcoming Q-Pix analog front-end ASIC. | 129 |

LIST OF TABLES

| <i>Number</i> | <i>Page</i> |
|---|-------------|
| 1.1 Description of the discovery of quarks. Notice that as the mass increases for a particular quark the year of discovery also increases. This is a property of how we create and observe the quarks in our accelerators, and also the reason why physicists continue to want to build bigger ones. Interesting physics happens at higher and higher energies, which require larger and more expensive detectors to probe these energy scales. Note that the lighter quark masses are not well understood for other experimental reasons, and the presented data are rounded to three significant figures based on [11]. | 4 |
| 1.2 Description of the quantum numbers of the fundamental lepton families. There are three unique families within the leptons: electron, muon, and tau. The charge carrier as well as the neutrino each carry a value of one for this number. Their anti-particle counterparts carry -1 of this number. | 5 |
| 1.3 Relative strength chart of the four fundamental forces of nature. Although gravity is not included within the SM it is included, as well as its theoretical force carrier the graviton. | 6 |
| 1.4 Relevant Liquid Argon parameter information. Values are taken from [12], with temperature $T_s = 87K$ and electric field $E_f = 0.5kVcm^{-1}$ | 13 |
| 1.5 Known Oscillation Parameters of Interest. Values are taken from the global fit [13]. The values shown assume normal mass ordering for neutrinos and include atmospheric Super-Kamikonde Data. | 19 |
| 1.6 Comparison of which type of detectors are useful for measuring which values of neutrino oscillation. | 19 |
| 2.1 Selected Requirements of DUNE-FD TPC electronics and Expected QPix Design goals of first generation ASIC development for comparison. TPC electronic data and rationale are taken from [7] | 37 |
| 2.2 Design Parameters | 38 |
| 2.3 Q-Pix based Requirements, which can be compared against 2.2. Results here are necessarily speculative, but provide a design goal baseline. | 39 |
| 4.1 The address values are not sequential because some registers have become deprecated through development. | 56 |
| 4.2 Description of the bit values within the register request word. | 56 |

| | | |
|-----|--|-----|
| 4.3 | Data word composition. | 57 |
| 4.4 | The address values are not sequential because some registers have become deprecated through development. | 61 |
| 4.5 | FPGA calibration results based on hard interrogations at a frequency of 4 Hz. | 81 |
| 4.6 | FPGA calibration results based on hard interrogations at a frequency of 0.1 Hz. . . . | 83 |
| 5.1 | The different tile parameters that are used for the effective tile search. The frequency drift relates the relative distribution of the frequency of adjacent oscillators. The tile size determines how many digital nodes are within a single tile. The routing configurations are described in detail in the previous chapter, and refer to how local data words are sent to the aggregator. The two different architectures define how the node enters the transmit local state. The push architecture enters whenever a new reset is acquired, whereas the pull architecture enters only when a data request is received from the aggregator. | 92 |
| 5.2 | Example results obtained from the three simulation examples for the pull architectures shown in the previous figures. The value of interest in determining the required remote FIFO depths for each ASIC is the maximum depth that occurred on any node. A memory optimized routing configuration is one that would introduce the least strain on the remote buffer depths for a given local buffer depth input. | 101 |
| 5.3 | The radiogenic background distribution is the same as that found in previous work [14]. For each 1000 second analysis the pre-rounded values are scaled up by a factor of 100 to achieve the correct normalization of events for each isotope. A key difference between the backgrounds is the origin or source of each background. Of special note is ^{40}K whose source location is the APA beams, and whose resets can be distinctly seen in Figure 5.4 as the slightly more active (yellow) region of the APA. Due to this source alone, it is likely that precise auto-calibration for charges will likely have to account for the pixel location within the APA. | 104 |

| | | |
|-----|---|-----|
| 5.4 | The different neutrino simulation parameters which are passed into Geant4 based simulation. The original interaction products are generated using GENIE [15] v2.12.10. The output products of the neutrino interaction produced from GENIE are then configured using the different parameters described above. We select ν_l events for different energies in bin-widths of 250 MeV; We follow the same bin width as is done in [16] for their neutrino oscillation analysis. A selection of 100 events for each ν_l is taken within each energy bin, for a total of 3900 ν_l events for each horn current direction, z-position, and θ_z selection. Since there are two current directions, four ν_l , five z-positions, and five θ_z positions, a total of 780,000 neutrino events are simulated. | 114 |
| 5.5 | Transaction Data | 116 |
| 5.6 | Buffer Data | 117 |
| 5.7 | Transaction Fit Results | 118 |

Chapter 1

INTRODUCTION

This chapter outlines and highlights useful background that will be explored in further detail in upcoming chapters as well as provides an outline for the thesis.

We begin with an overview of the standard model, and how both its success and short comings drive larger and more expensive detectors. These detectors must reach for ever newer limits, in both precision and scale, due to the robust nature of the Standard Model. To elucidate the issues at the forefront of the Standard Model we provide a brief history, with an emphasis on the detectors and experiments which helped lead to its current status. Next, we become more specific and discuss DUNE which is a example of a new, large, and expensive detector which aims to push beyond the Standard Model. Finally, we finish this section on a discussion on the developments of new tracking detectors and highlight their relevance to the work presented here.

1.1 The State of Things: The Standard Model

What is the universe made of? What are the fundamental building blocks of matter? Since time immemorial thinkers have questioned the nature of the universe and wondered what the basic building blocks of nature are. The answer to these fundamental questions is the motivation for particle physics.

In the history of science, it is easy to argue that the most successful of all models is the Standard Model of Physics. The Standard Model (SM) [17–19] was originally developed in the mid to late 1970’s and is the model responsible for unifying the weak, strong, and electromagnetic forces together. It was gradually developed in the 1970’s as a result of the boom in particle detectors in the mid and late 1960’s. It has made remarkable predictions about the existence of elusive neutrinos, quarks and vector bosons before their discovery, and more.

The comprehensive and extensive list of known particles as well as various cross-sections, lifetimes, and other known information can be found from the bi-annually published Particle Data Group (PDG) [11]. The SM has been experimentally tested to limits unlike any other theory.

In this section we briefly describe the SM and highlight some (certainly not all) key aspects of its

formulation as understood today. The SM has stood the test of time, despite many known failures and holes in its predictions. Therefore, we hope to elaborate a bit on its status involving predictions and unknown parameters to help the reader better appreciate the significance of looking for physics beyond the SM.

The Basics of the Standard Model

The SM itself dictates what the fundamental constituents of matter and energy are. Like any theory in science, its purpose is to explain observed phenomena. In this case, the observed phenomena are not simply the origin of all observable particles and their masses, but also a description of all observable interactions.

The interactions described by the SM involve the fundamental particle interactions via three of the four known fundamental forces observed in nature: the electromagnetic, weak, and strong forces. The missing fourth force is one of the major shortcomings of the SM: its inability to incorporate a quantum description of gravity. The discussion of the renormalization of quantum gravity is beyond the scope of the work presented here, so we will only mention that it needs to be achieved.

All currently known fundamental particles are represented in Fig. 1.1. These particles represent the today’s best knowledge of the building blocks of all observed matter in the universe.

The Quarks

The quarks represent particles in the top left of Figure 1.1.

Quarks are the fundamental particles which constitute the “normal” heavy particles, such as protons and neutrons. The quarks also have unique anti-particle partners, which brings the total number of quarks up to 12. Like all antiparticles, the anti-quark partners have the same mass as the normal partners, with all the quantum numbers reversed.

A unique feature of quarks compared to leptons is that no “free” quark has ever been observed. This means that all current direct observations of quarks are in bound states. Most commonly, the quarks combine in pairs or triplets to form mesons and baryons, respectively. Even more complicated assemblies can be made of additional quarks, such as tetra and penta quarks, as long as all the quantum numbers are unique for each quark.

The mesons contain a quark and an anti-quark, whereas the baryons contain three quarks. Collectively, all particles constituted by any combination of quarks are known as hadrons. In 1961

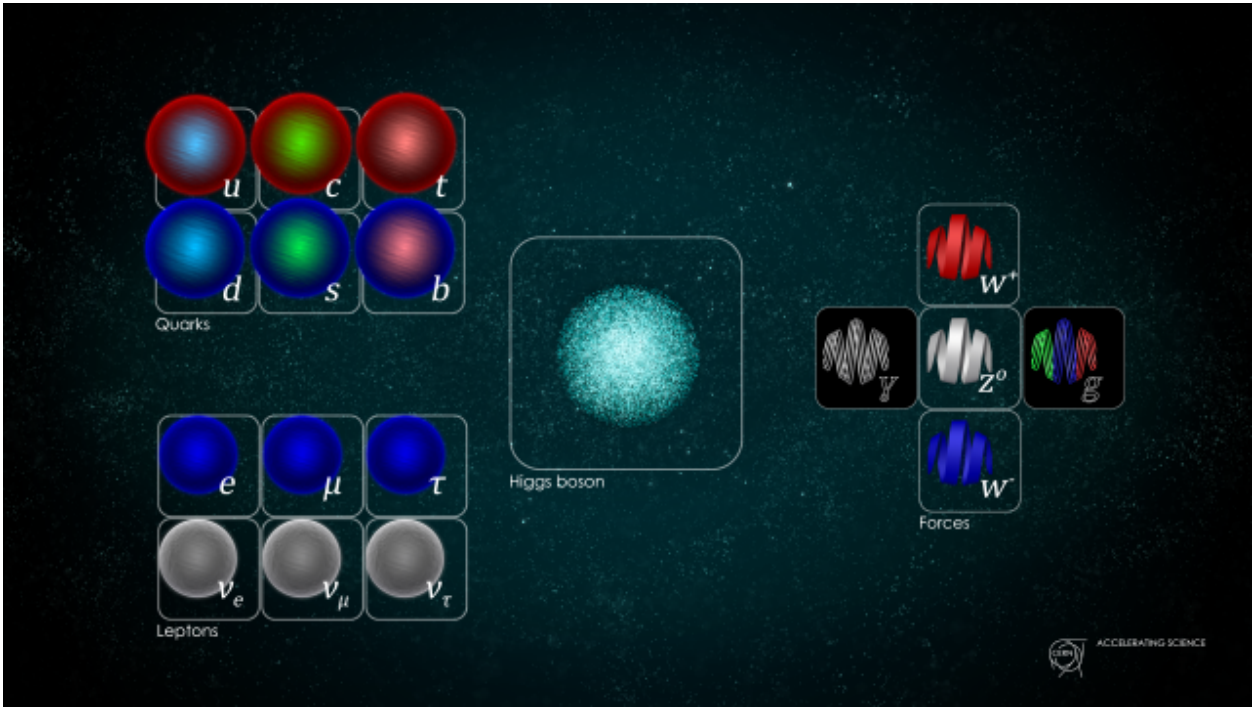


Figure 1.1: Image of Fundamental Particles in the Standard Model, taken from CERN website [1]. All known matter and particle interactions involves combinations of the particles shown here.

Murray Gell-Mann proposed his “eight-fold way” [20] which provided a method of grouping the hadrons.

Since quarks are not freely observable a common place to infer their existence (and to create heavier hadrons) are in particle accelerators. The most well known particle accelerator is the Large Hadron Collider (LHC) in Geneva. These Particle accelerators generate extremely high energy ($\approx \mathcal{O}(10TeV)$) protons which when collided can generate new composite hadrons of any mass so that the total energy is conserved.

Since quarks, due to their color, readily combine to create more easily observed composite particles. The Quark model was then proposed by Gell-Mann in 1964 [21]. This model is a group theory concept (known as SU(3) symmetry) and is the means for which the fundamental particles (quarks) combine into the composite particles (hadrons) which are more readily and easily measured today. Eventually experiments conducted at the Stanford Linear Accelerator (SLAC) between 1967-1973 verified the existence of these quarks and Gell-Mann won the Nobel Prize in 1969.

The rescue of the quark model came with the measurement of [22]. The J/ψ particle indicated the existence of a fourth since then unmeasured quark, which we now know as the charm (c).

| Quark | Charge | Mass (MeV) | Year Discovered | Ref. |
|---------|----------------|------------|-----------------|---------------|
| up | $\frac{2}{3}$ | 2.16 | 1968 | SLAC [23, 24] |
| down | $-\frac{1}{3}$ | 4.67 | 1968 | SLAC [23, 24] |
| strange | $-\frac{1}{3}$ | 93.4 | 1968 | SLAC [23, 24] |
| charm | $\frac{2}{3}$ | 1270 | 1974 | SLAC [22] |
| bottom | $-\frac{1}{3}$ | 4180 | 1977 | Fermilab [25] |
| top | $\frac{2}{3}$ | 173000 | 1995 | Fermilab [26] |

Table 1.1: Description of the discovery of quarks. Notice that as the mass increases for a particular quark the year of discovery also increases. This is a property of how we create and observe the quarks in our accelerators, and also the reason why physicists continue to want to build bigger ones. Interesting physics happens at higher and higher energies, which require larger and more expensive detectors to probe these energy scales. Note that the lighter quark masses are not well understood for other experimental reasons, and the presented data are rounded to three significant figures based on [11].

The Leptons

The leptons represent particles in the bottom left of Figure 1.1.

The first lepton discovered, and the most commonly recognized, is the electron which was discovered by J. J. Thomson. Just like the quarks, the leptons come in three families (electron, μ , τ). Also like the quarks, the leptons have charge, mass, and flavour which means they can decay.

Unlike the quarks the leptonic particles do not have a color quantum number and therefore do not combine together to create composite particles. Additionally, free leptons are observed, e.g. the electron.

The most difficult to measure fundamental particles of within the SM are the neutrinos. This is because these leptons carry no net charge. However, since they carry flavour and can decay (or be absorbed) and they also carry their respective lepton number, the neutrinos in the family can be identified by measuring their partner.

For example, a common process to observe an anti-electron neutrino ($\hat{\nu}_e$) is through inverse beta-decay (IBD) following the reaction:

$$\hat{\nu}_e + p \rightarrow e^+ + n \quad (1.1)$$

| Lepton | Charge | N_e | N_μ | N_τ |
|------------|--------|-------|---------|----------|
| e^- | 1 | 1 | 0 | 0 |
| ν_e | 0 | 1 | 0 | 0 |
| μ | 1 | 0 | 1 | 0 |
| ν_μ | 0 | 0 | 1 | 0 |
| τ | 1 | 0 | 0 | 1 |
| ν_τ | 0 | 0 | 0 | 1 |

Table 1.2: Description of the quantum numbers of the fundamental lepton families. There are three unique families within the leptons: electron, muon, and tau. The charge carrier as well as the neutrino each carry a value of one for this number. Their anti-particle counterparts carry -1 of this number.

This IBD reaction is a common measurement tool for identifying neutrinos because of the distinguishable detection signature of the produced particles. The positron (e^+) annihilates quickly ($\approx \mathcal{O}(ns)$) and will produce back-to-back 511 keV photons. The produced neutron, on the other hand, wobbles around much longer ($\mathcal{O}(us)$) before being captured, which produces scintillation light of energy proportional to the neutrons energy when captured.

The muon (μ) was discovered by Anderson and Neddermeyer in 1936 by observing cosmic ray showers [27].

The tau (τ) was discovered by SLAC in 1975 [28].

The first measurements of the neutrinos in each family were much harder than their charged partners. The electron neutrino (ν_e) and the muon neutrino (ν_μ) are observed in decay interactions.

The tau neutrino (ν_τ) was exceptionally difficult to measure. Like the previous neutrino partners, the ν_τ is discovered by looking for the creation of its partner (τ) during a CC interaction. As a comparison the τ has a lifetime of only 10^{-13} s whereas the muon life time $T_\mu \approx \mathcal{O}(1\mu s)$ or seven orders of magnitude shorter!

The first successful experiment came in 2000 [29]. DONUT utilized a much more complicated emulsion detector to collect tracks from a 800 GeV proton beam offline. The exxperiment collected a total of 203 neutrino interactions, of which it found evidence for a total of only four interactions.

| Force | Scale | Theory | Carrier | Ref. |
|-----------------|------------|--------------------|------------|----------------|
| Strong | 10 | Chromodynamics | gluon | TASSO [30] |
| Electromagnetic | 10^{-2} | Electrodynamics | photon | Planck? |
| Weak | 10^{-13} | Flavourdynamics | W^\pm, Z | CERN [32],[33] |
| Gravity | 10^{-42} | General Relativity | graviton | ?? |

Table 1.3: Relative strength chart of the four fundamental forces of nature. Although gravity is not included within the SM it is included, as well as its theoretical force carrier the graviton.

The Forces - Vector Bosons

All forces within the standard model (electromagnetism, weak, and strong) are governed via a “carrier” particle. These carrier particles are represented on the center-right of 1.1.

The electromagnetic force is governed by particle exchanges of a photon. Other than perhaps gravity, which isn’t explained by the SM, this is the most well known and described force. All particles which carry charge interact via this force. Therefore the neutrinos are the only particles within the quarks and leptons which do not interact at all with the electromagnetic force (this is why detecting them is so hard). The full theoretical description of this force is governed by Quantum-Electrodynamics (QED).

The weak-nuclear force is governed by particles exchanges of one of the three particles in the center: W^\pm and Z . This force involves a change in flavor of a particle, and involves both quarks and leptons. It is also responsible for all decay processes. The theoretical description of these mechanics are called Quantum-Flavourdynamics (QFD).

The strong-nuclear force is governed by the exchange of the gluon (g). This force is responsible for color changes of matter and describes why nuclei are held together. Since this force only involves exchanges of a gluon, the leptons are therefore unaffected since these particles carry no color quantum number. The full theoretical description for the strong-nuclear force is Quantum-Chromodynamics (QCD).

The gluon was discovered in at the TASSO experiment 1979 [30, 31].

Measurements of the intermediate bosons were much harder. The W^\pm boson were measured in 1983 [32]. Followed by the Z boson which was measured shortly afterwards in the same experiment [33].

The Higgs - Scalar Boson

The last particle to be discovered in the SM was the Higgs particle. The Higgs particle was originally predicted in 1964 by Peter Higgs [34]. This particle is important to describe how mass is given to the elementary particles described by the SM. Finally, in 2012 the Large Hadron Collider (LHC) was able to infer the massive Higgs particle [35].

1.2 The Problem: Moving Beyond the Standard Model

Despite its (SM) numerous achievements in predictive power and experimental verification we know today that it has crucial shortcomings. The Standard Model (SM) [17–19] has no ability to account for Dark Matter or Dark Energy in the universe, nor the distribution (or the hierarchy) of neutrino masses, nor is it able to relate how gravity interacts with the other fundamental forces of nature (Unification). It also doesn't account for some 'basic' properties it has, such as: why are there only three generations of leptonic particles (electron, muon, and tau)? These short-comings offer hints for where to search for physics. Physicists have known about these short comings from the conception of the Standard Model and have (to no avail) sought out what's next.

With a plethora of hints to search for New Physics (NP), it can be useful to organize the efforts of search. In 2008 the Particle Physics Project Prioritization Panel (P5) did just this and labeled the three frontiers of physics: the cosmological, energy, and intensity frontiers. Each of these frontiers offer different kinds of challenges and serve as guides to look for physics beyond the SM.

Searches at High Energy

The energy frontier is concerned with the origin of mass. The Large-Hadron Collider (LHC) [35] experiment is the archetypal experiment aimed at solving problems within this frontier. The LHC itself consists of other large-scale tracking and calorimetry experiments such as ATLAS [36] and CMS [37].

Large particle accelerators are used to generate source particles of ever increasing energy. Due to the conservation of mass, the higher the energy of the particle accelerated the higher the mass (energy) of the particles created after certain collisions can be.

There also exist lepton colliders [38] which offer unique areas of search along this frontier too. More detailed descriptions of such collider experiments are beyond the scope of the work presented here, and further reading may be pursued from the extremely detailed technical design reports cited here of Belle-II and the ATLAS experiments.

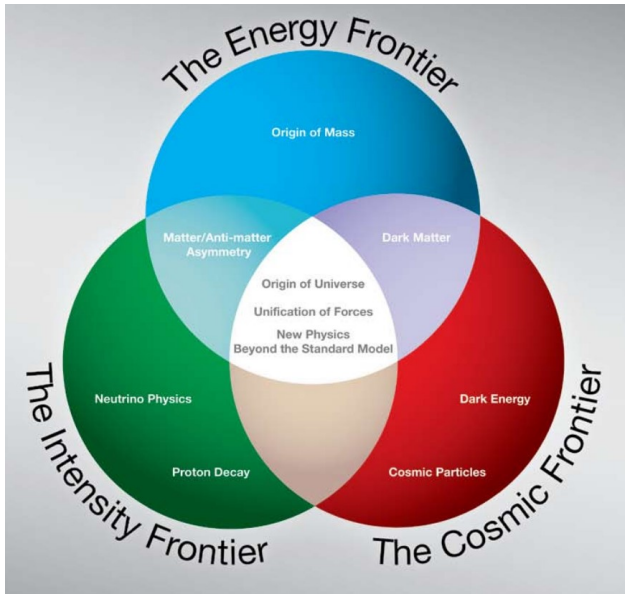


Figure 1.2: Image based on the 2008 P5 report [2]. The white text labeled within each frontier describes the search for some physics beyond the SM within that frontier.

Other Searches

The cosmological frontier aims to search for NP on extremely large time and distance scales by relying on observational techniques. Cosmological measurements have shown that majority of the universe's matter is not visible to light, and so we call it dark matter. Additionally, the universe is expanding at an accelerated rate, which we can tell from the blueshift of distance galaxies. Likewise, cosmologists have also discovered that the universe is expanding due to some invisible energy in the universe, and so we call it dark energy.

The search for these dark causes of the universe lie within the realm of the cosmological frontier.

Dark energy currently resides as the explanation for the observed accelerated expansion of the universe. Dark matter is commonly used to explain the deviation of the rotational frequency of galaxy clusters.

The third (and final) frontier we'll discuss is the Intensity frontier. The Intensity Frontier of Physics ([2]) is one which today requires very large and very precise measurements to gain the statistics to declare an observation. In order to address the issues posed within this frontier the large scale detectors hunting for New Physics (NP) have continued to grow in size, energy sensitivity, and importantly cost: [39].

As compared to the energy frontier which normally relies on creating new particles from accelerators

the Intensity Frontier often searches for rare events, like a proton decay.

Neutrino searches also lie within this frontier. Neutrinos are notoriously difficult to detect and measure since they can only be probed via the weak-nuclear force, and even then only indirectly since they carry no charge themselves.

How did we get here?

Many times since the early 20th century it was thought that the goal of physics was accomplished. However, during each of these moments of false triumph some new detector was built to take a new measurement; thus, the door to new understanding of nature is never closed. This section provides a brief and (necessarily) incomplete history of significant measurements and detector developments relevant to particle physics in the creation of the SM. In order to clear an obstacle, it is often helpful to remember the previous ones.

A Century of New Physics

At the turn of the 20th century particle physics was in its infancy. In 1900 Max Planck first introduces the concept of energy quanta for the first time concerning photons to eliminate the infamous ultra-violet catastrophe problem introduced by statistical mechanics. JJ Thomson used a single cathode-ray tube to discover the electron and the nucleus, and won for himself the Nobel Prize in 1906. Milikan's famous oil-drop experiment won him the Nobel Prize in 1923.

However, as each of these new discoveries solved problems only more questions were produced. Once the nucleus was discovered to contain only protons and neutrons, the natural question arose: what holds all of the positive charge together in the center. Thus, physicists cleverly named the new force which was stronger than the electromagnetic force: the Strong Force.

The bubble chamber was then invented in 1952 by Donald Glaser [40]. These detectors proved significant in the discover of the W and Z bosons and ultimately allowed the unification of the electromagnetic and weak forces to form the electroweak theory.

Next the spark chamber eventually lead to the gradual development of the wire-spark chamber. In 1968 Georges Charpak developed the Multi-Wire Proportional Chamber (MWPC) for which he (much later) won the Nobel Prize in 1992. From this key insight a new detector concept was made possible.

Finding Neutrinos

Hints at the existence of neutrinos began early last century. More than 100 years ago Chadwick was able to show that the energy spectrum from a decaying electron was continuous [41]. This unknown cause of the spectrum even lead some physicists to belief that perhaps the conservation of energy was violated. Wolfgang Pauli instead predicted a particle which he originally called the neutron to also be a decay product, but not easily observable. This third particle in the decay would explain the energy spectrum of the electron. Quickly however the particle name neutron was taken by a different neutral particle in 1932 [42] The discovery of the neutron and the continuous spectrum of beta decay forced Pauli to come up with a new theory attempting to describe beta decay [43].

Originally physicists held little hope that such an elusive particle would ever be detected. However, the motivation to save this conservation law lead Wolfgang Pauli to the first prediction (1930) of the neutrino; the reason that the energy was a spectrum from the electron was that some of the energy was “taken up” by the neutrino. Finally, some 26 years later in 1956 was the first observation of the electron neutrino [44].

The discovery of the electron neutrino ν_e was the first of the three families to be discovered. A few years later the first reactor neutrino (ν_μ) was observed at Brookhaven National Laboratory (BNL) [45].

The first measurement of the τ neutrino (ν_τ) happened much later in 2001 [29]. this detector used nuclear emulsions.

Daya Bay [46] has also established measurements of electron anti-neutrino ($\bar{\nu}_e$) disappearance.

After this first discovery is when the answers, followed by more questions, came. Since then, many large-scale experiments have been dedicated to measuring the three generations of neutrinos. [46–53]

All reliable information we have about neutrinos come from these large scale detectors.

Originally the mass of the neutrino predicted by the SM was massless. That was until the Solar-neutrino anomaly measured significantly less neutrinos than predicted [54]. The solution for this was oscillation.

1.3 Modern Tracking Detectors

It could be said that any definition defining a “new” age of a types of detectors is subjective. Nevertheless, we proceed to define that modern particle detectors were the age that began to use modern electronics, or electronics after the development of the metal–oxide–semiconductor field-effect transistor (MOS-FET). If there was any invention which was able to drive the development of

computers and measuring electronics, it was the transistor. Therefore, the beginning of the modern particle detection age began with the transistor, and it saw to the end of the spark chamber and bubble chamber detectors.

Multi-Wire Proportional Chamber

The middle of the 20th century saw a dramatic increase in the ability and reduction of the cost of electronics. These (then) new electronics allowed for fast digitizing measurements of voltage or current. Thus, new proportional counter detectors were capable of using computers to do the measuring or counting of the events within the detector. The rate at particles could then be detected increased by orders of magnitude.

Using the fast digitizers and closely spaced wires Georges Charpak (1924-2010) created the first-Wire MWPC in 1968 [55]. This new detector was one which paved the way for modern detector development, for which Charpak won the 1992 Nobel Prize.

Time Projection Chambers

Time Projection Chambers (TPC) [56] have been shown to be extremely useful in high energy physics experiments due, in part, to their high resolution in both timing and spatial dimensions. This detector was originally used in the Position-Electron Project PEP-4 experiment which measured electron-positron collisions from the 29 GeV electron beam produced at the Stanford Linear Accelerator (SLAC). The first TPC design used high pressure gas and was able to measure 1000s of particle tracks per second (compared to 1-10) and provide full 3-D event reconstruction.

It did not take long for other experimentalists to generalize this concept to different elements or even to liquid.

Noble Gases and Time Projection Chambers

The technology of TPCs has greatly matured since their original inception. in many kinds of detectors across HEP. TPCs can also incorporate two phases of a substance (liquid and gas), called Dual Phase (DP) TPCs.

the Xenon-1T is a dark matter experiment which is a dual-phase TPC [57].

The LUX experiment is a single phase TPC also hunting for dark matter.

A specific kind of TCP is a Liquid Argon Time Projection Chamber (LArTPC) [58].

Recent work on LArTPCs ([59–61].)

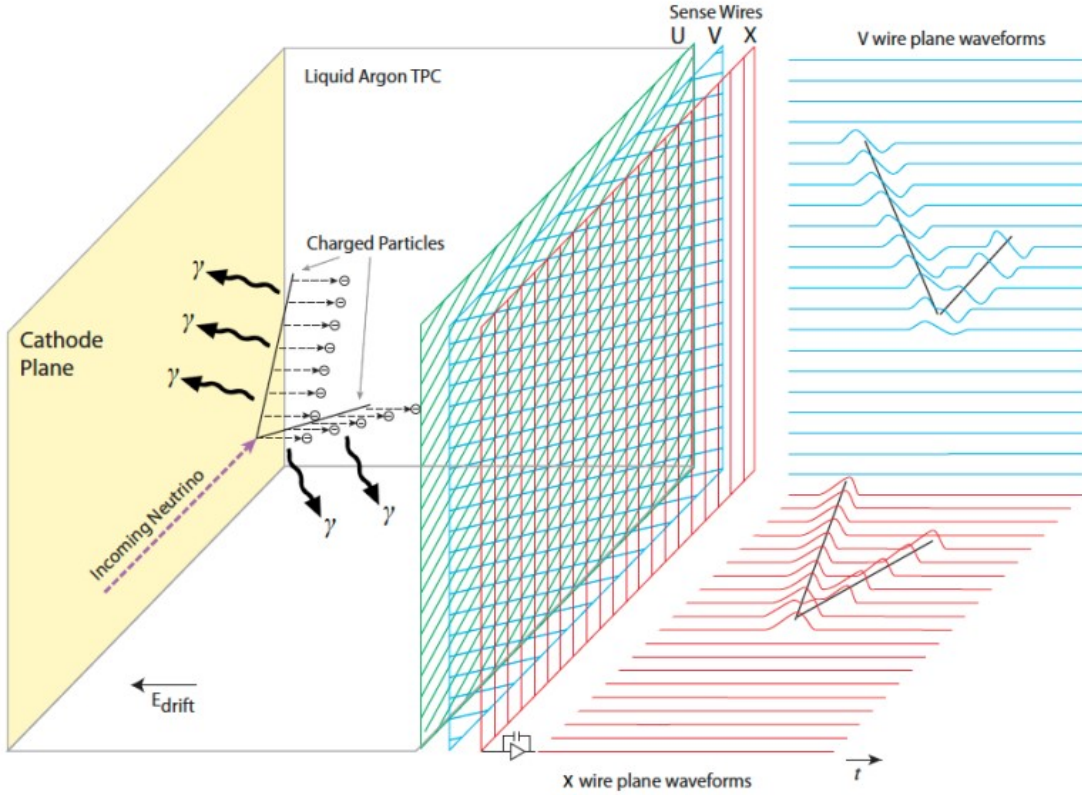


Figure 1.3: Image of a Time Projection Chamber (TPC). Charge is accumulated within the volume as ions are removed from the fiducial volume from another charged ion as it passes through the material. An uniform electric field drifts the free now electrons towards the anode plane. The collection and readout of charge on this anode plane is what is recorded within the detector. Image is taken from [3].

Energy resolution of the LArTPCs within DUNE are still unknown to within a factor of 4 [62].

1.4 Ways Forward

Despite the passing of generations of detectors and developments in electronics the SM remains. For nearly 50 years now the SM is still our best model at describing nature as we know it, despite also knowing that there must be more. Here in this section we describe in some more detail current searches at the intensity frontier where physicists are looking to go beyond the SM.

We give special attention to neutrino oscillation at the end of this section since later chapters simulation studies will be based off results hoping to measure this effect.

| Property | Symbol | Value | Unit |
|---|-------------------|---------|-------------|
| Density | ρ | 1.3973 | gcm^{-3} |
| Fano Factor | F | 0.107 | - |
| Dielectric Constant | ϵ | 1.505 | - |
| electron drift velocity | v_e | 0.1601 | $cm/\mu s$ |
| Ionization Energy of single e^- | W_i | 23.6 | eV/e^- |
| Ionization Energy of single e^- from photon | W_{scint} | 19.5 | eV/γ |
| Minimum Specific energy loss | $(dE/dX)_{MIP}$ | 2.12 | MeV/cm |
| Hadronic Interaction Length | λ_{int} | 85.7 | cm |
| Scintillation Emission Wavelength | λ_{scint} | 128 | nm |
| Longitudinal Diffusion Coeffecients | D_L | 6.6270 | cm^2/s |
| Transverse Diffusion Coeffecients | D_T | 13.2327 | cm^2/s |

Table 1.4: Relevant Liquid Argon parameter information. Values are taken from [12], with temperature $T_s = 87K$ and electric field $E_f = 0.5kVcm^{-1}$.

Hadron Decay

Does a proton decay? This is the fundamental question for physicists studying hadron decay. The SM predicts that the proton itself is stable, so it should never decay. Therefore, the search for proton decays offers a path for physics beyond the SM. Attempts to unify all the fundamental forces of nature into a unified theory are called Grand Unified Theories (GUTs), and according to many GUTs, the proton does indeed decay.

Current measurements on the proton lifetime indicate that its lifetime is on the order of magnitude (or above) 10^{34} years. Even at its most frequent, this is an exceedingly rare event considering that the lifetime of the universe is $\approx \mathcal{O}(10^{10}yrs)$

Since these events are so rare, extremely large detectors with large numbers of protons inside of them are required to constantly observe many protons. An example of a second generation proton decay studies is the Imaging Cosmic and Rare Underground Signals(ICARUS) experiment [63].

There are at least two prominent decay chains that are expected to be dominant, depending on the Grand-Unification-Theory (GUT) that hopes to go beyond the SM. The first one is:

$$p^+ \rightarrow e^+ + \pi^0 + 2\gamma \quad (1.2)$$

This interaction is easily detectable in cherenkov based detectors due to the emission of both the gammas as well as the high energy of the emitted positron. In fact, the worlds best estimate for proton lifetime comes from this decay-chain [64].

Other Supersymmetric GUT models predict instead [65]:

$$p^+ \rightarrow K^+ + \nu \quad (1.3)$$

In this case the Kaon is generally moving too slow to be measurable by cherenkov detectors. However, a TPC style detectors are still sensitive to its signature charge deposition. This is an interesting reaction since the worlds best limits are currently provided by the Super-Kamiokande experiment, which is itself a cherenkov based detector in water.

These searches are interesting, if albeit difficult, both due to the rareness of such an event. If any detector was able to clearly measure even a single proton decay, that would provide direct evidence for physics beyond the SM. Future detectors that will continue to probe for nucleon decay are DUNE, Hyper-Kamiokande, and JUNO [3, 39, 66].

Supernova Studies

A supernova occurs when a massive star runs out of the necessary elemental fuel for fusion at its core. When this happens the inward pull of gravity due to the mass of the star overcomes the reduced outward pressure from the nuclear fusion.

It has been nearly 30 years since the last observed neutrinos from a galactic core collapse supernova, SN 1987A [67]. Sensitivity to supernova neutrinos is crucial for understanding the mechanisms that govern particles at these extreme densities and pressures. Interestingly, because neutrinos are so weakly interacting, it is possible to observe their signature and arrival before the photons arrival of a Type-II supernova.

The principal interaction chain observable in a TPC is:

$$\nu_e + {}^{40} Ar \rightarrow e^- + {}^{40} Kr^+ \quad (1.4)$$

A LArTPC is sensitive to ν_e by measuring the signture of both the e^- and ${}^{40} Kr^+$.

Neutrino Oscillation

Another possible route beyond the Standard Model is the detailed study of neutrinos.

Here we provide a general description of a model to describing neutrino oscillation. We elucidate the measureable parameters which govern this oscillation and describe how these values are currently measured in experiments today.

Of all known particles the most elusive (hardest to detect and measure) is the neutrino. For this reason the least is known about the neutrino. What we do know about the neutrino is there are three flavors each associated with their leptonic partners: the electron, muon, and tau.

Tokai to Kamioka (T2k) [68] has well established neutrino oscillation measurements.

It came as a welcome shock that neutrino oscillation was first measured. This oscillation indicates that a neutrino as it moves through space can change its state; a electron neutrino can oscillate into a muon neutrino or even a tau neutrino. This happens because the mass eigenstate and flavor eigenstates which govern the neutrino are not equal.

The standard notation which relates the mass eigenstates (ν_i) and flavor eigenstates (ν_α) ,

$$\nu_i = U_{i\alpha} \nu_\alpha \quad (1.5)$$

$$\begin{pmatrix} \nu_e \\ \nu_\mu \\ \nu_\tau \end{pmatrix} = \begin{pmatrix} U_{e1}, U_{e2}, U_{e3} \\ U_{u1}, U_{u2}, U_{u3} \\ U_{\tau 1}, U_{\tau 2}, U_{\tau 3} \end{pmatrix} \begin{pmatrix} \nu_1 \\ \nu_2 \\ \nu_3 \end{pmatrix} \quad (1.6)$$

The matrix elements within U_{li} represent the mixing coeffecients and are used to calculate the probability that a certain neutrino will oscillate from one family to another. We identify U_{ij} as the commonly known U_{PMNS} matrix, where PMNS stands for: Pontecorvo–Maki–Nakagawa–Sakata, or the four theorists who helped developed this convention. Luckily, there are not a total of nine free parameters within the SM that determine this. The U_{PMNS} matrix can be additionally rewritten following [69, 70] as:

$$U_{PMNS} = U_{sol} \times U_{rea} \times U_{atm} \times U_{maj} \quad (1.7)$$

After expanding the matrix representations, equation 1.4 becomes:

$$U_{PMNS} = \begin{pmatrix} 1 & 0 & 0 \\ 0 & C_{23} & S_{23} \\ 0 & -S_{23} & C_{23} \end{pmatrix} \times \begin{pmatrix} C_{13} & 0 & S_{13}e^{-i\delta_{CP}} \\ 0 & 1 & 0 \\ -S_{13}e^{-i\delta_{CP}} & 0 & C_{13} \end{pmatrix} \times \begin{pmatrix} C_{12} & S_{12} & 0 \\ -S_{12} & C_{12} & 0 \\ 0 & 0 & 1 \end{pmatrix} \times \begin{pmatrix} e^{i\alpha_1} & 0 & 0 \\ 0 & e^{i\alpha_2} & 0 \\ 0 & 0 & 1 \end{pmatrix} \quad (1.8)$$

We identify above the additional matrix components where historically these values are measured. Therefore, instead of nine unknown parameters for the SM, there are only six. The components C_{ij} and S_{ij} in the matrices are defined to be $\cos(\theta_{ij})$ and $\sin(\theta_{ij})$, respectively.

Then, the six parameters of the U_{PMNS} are identified as:

- θ_{13} , reactor measurements.
- θ_{12} , atmospheric measurements.
- θ_{23} , solar measurements.
- δ_{CP} , Charge-conjugation parity violation.
- α_1/α_2 , The two Majorana Phase parameters.

The Majorana phases (α_i) are sensitive in experiments that can detect the Majorana nature of neutrinos such as neutrinoless double beta decay. In neutrino oscillation measurements, these phases cancel out and are not measurable. Therefore, we ignore these two phases for the remainder of this work.

Next we demonstrate the calculation of the probability of oscillation from one mass eigenstate to another. Namely we calculate the probability $P(\mu \rightarrow e)$ which is the probability of interest in a long beamline experiment. First we identify that equation 1.4 can be rewritten to isolate the flavor-eigenstate terms (v_α) by multiplying by the adjoint of the PMNS matrix (U_{PMNS}^*). Then the relationship between the mass and flavor eigenstates become:

$$v_\alpha = U_{PMNS}^* v_i \quad (1.9)$$

The value of interest is $P(\mu \rightarrow e)$. The probability to end up in state ν_e beginning from ν_μ is:

$$P(\mu \rightarrow e) = |\langle \nu_e | \nu_\mu \rangle|^2 \quad (1.10)$$

We then use equation 1.4 to represent the matrix elements of U_{PMNS} from ν_e and ν_μ to obtain:

$$P(\mu \rightarrow e) = \left| \sum_i U_{ei} U_{\mu i}^* e^{-iE_i t} \right|^2 = \sum_i |U_{ei} U_{\mu i}^*|^2 + 2\Re \left(\sum_{i>j} U_{ej}^* U_{\mu j} U_{ei} U_{\mu i}^* e^{-i\Delta_{ij} t} \right) \quad (1.11)$$

Where we identify that the cross terms introduce a phase difference shown as Δ_{ij} in the second term in equation 1.4. This represents the neutrino oscillation term and represents the difference in the mass states of the neutrinos:

$$\Delta_{ij} = (E_i - E_j) \quad (1.12)$$

The energy of the neutrino in each state can be approximated to first order following:

$$E_i = \sqrt{p^2 + m_i^2} \approx p + \frac{m_i^2}{2p} \quad (1.13)$$

The momentum of all of the mass eigenstates is the constant. Then oscillation parameter becomes:

$$\Delta_{ij} \approx \frac{1}{2p} (m_i^2 - m_j^2) = \frac{\Delta m_{ij}^2}{2p} \quad (1.14)$$

Finally, the last two parameters which govern the neutrino oscillations are identified as the mass differences between the three mass states. Now, the frequency of the oscillation between neutrino states depends on the difference of the square their masses (Δm_{ij}^2), where three neutrino masses imply two independent differences. The mass differences provide two additional parameters are needed to fully describe neutrino mixing. The six values of interest and their current best known fits are shown in Table 1.4:

The sign of m_{13} is unknown. This leads to two possible orderings of the masses, known as normal and inverted, NO and IO respectively. The normal ordering indicates that the masses of the

Neutrino Mass Hierarchy

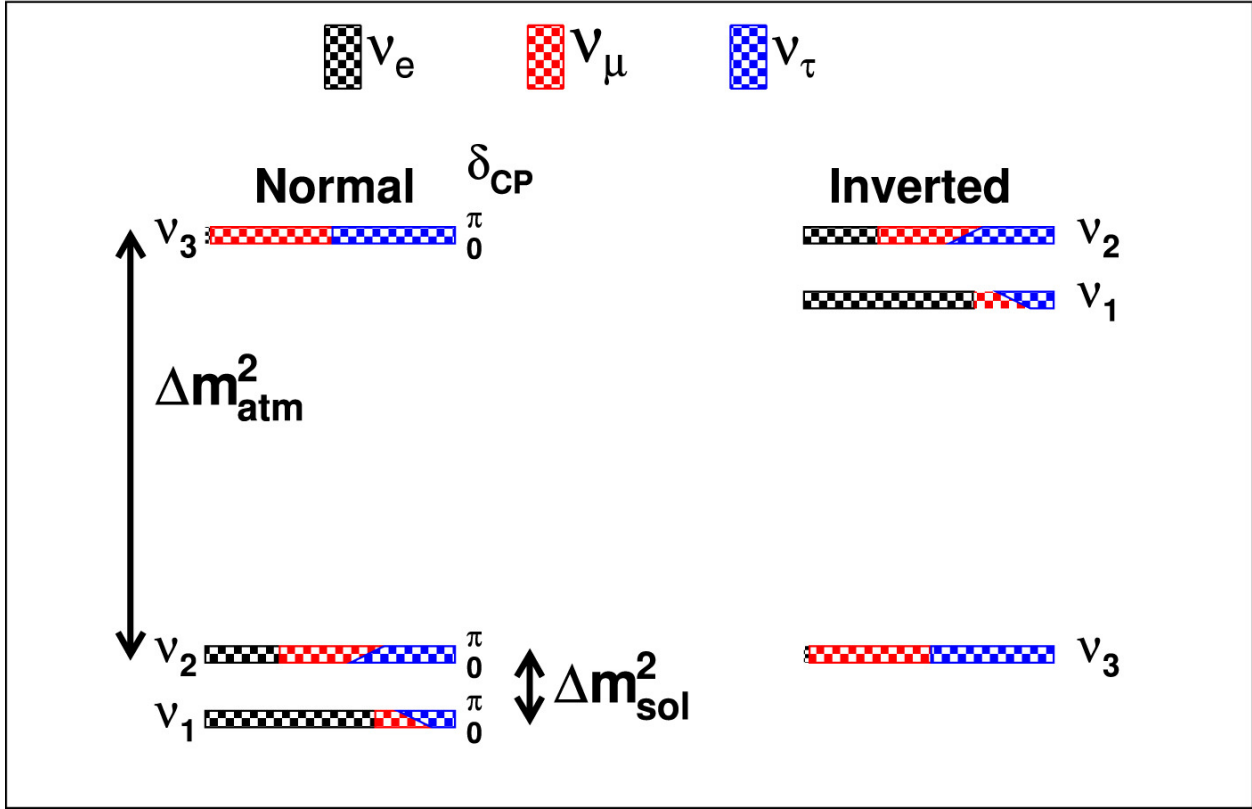


Figure 1.4: Representation of the mass hierarchy scales. This is a representation of the two possible orderings of neutrino masses, due to the uncertain sign of m_{13} . It is also interesting to observe that the absolute mass scale is not measured since oscillation measurements only give difference mass squares. Image was taken from [4].

neutrinos follow the ordering of their charged partners. That is, NO implies a mass ordering of: $\nu_e < \nu_\mu < \nu_\tau$. Whereas, the IO has a mass ordering: $\nu_\tau < \nu_e < \nu_\mu$.

Neutrino oscillations in matter are slightly different than those in vacuum [71]. The Mikheyev-Smirnov-Wolfenstein (MSW) effect [72] also contributes to differing neutrino oscillations as they move through matter of varying density, which additionally complicated the calculation. The MSW effect also affects neutrinos differently than anti-neutrinos, which is useful for measuring δ_{cp} . This resonance affect for beam-line experiments affects ν_e in the case of normal mass ordering (NO), whereas in the case of inverted mass order (IO), the $\hat{\nu}_e$ experiences resonance and is thus more likely.

| Paramater | Best Fit | Unit | Best Soruce |
|-------------------|---------------------------|----------------|-------------------------|
| θ_{13} | $8.57^{+0.12}_{-0.12}$ | na | Reactor |
| θ_{12} | $33.44^{+0.77}_{-0.74}$ | Atmospheric | |
| θ_{23} | $49.2^{+0.9}_{-1.2}$ | na | Solar |
| δ_{cp} | 197^{+27}_{-24} | na | Atmospheric+Accelerator |
| Δm_{21}^2 | $7.42^{+0.21}_{-0.20}$ | $10^{-5} eV^2$ | Solar |
| Δm_{3l}^2 | $2.517^{+0.026}_{-0.028}$ | $10^{-3} eV^2$ | Atmospheric |

Table 1.5: Known Oscillation Parameters of Interest. Values are taken from the global fit [13]. The values shown assume normal mass ordering for neutrinos and include atmospheric Super-Kamikonde Data.

| Paramater | Best Experiments | Type of Detector |
|-------------------|------------------|------------------|
| θ_{13} | | |
| θ_{12} | | |
| θ_{23} | | |
| δ_{cp} | | |
| Δm_{21}^2 | | |
| Δm_{3l}^2 | | |

Table 1.6: Comparison of which type of detectors are useful for measuring which values of neutrino oscillation.

1.5 Neutrino Tracking Detectors in the Current Century

Finally, in this last section we discuss the development of various upcoming detector technologies. There are many motivating pressures for new detectors to adopt pixelated designs. Below we discuss two contributing factors: the development of electronics and computing algorithms.

First, previously pixelated detectors have historically been more difficult because of the issues of cost and size regarding the number of readout channels. This is being addressed, in part, by the advent of newer, cheaper, and larger Field-Programmable-Gate Arrays (FPGAs). One method for reducing the electronic overhead required in pixelated detectors is to use digital multiplexing. Cheap, high channel FPGAs directly solve this problem. Other electronics development, such as the Silicon-Photomultiplier, offer much cheaper alternatives for large pixel counters compared to their historical counter-parts.

1.6 Future Detectors

[73] Another driving factor is the development of Machine Learning (ML) algorithms, particularly Convolutional Neural Network (CNN [74]). Recent industry has driven the need for CNNs to be able to correctly identify and label 2-D images of various kinds, and thus championed much of progress in this field and spawned many kinds of CNN algorithms.

Recently, it has been shown how these kinds of algorithms extend into High Energy Physics (HEP) for particle identification. A major issue at the Intensity Frontier of physics is the sheer amount of data to store and process. These ML algorithms provided a developed tool to automate the analysis of huge amounts of data ($>> 1TB$) and have been shown to be quite accurate ($> 99\%$) at particle identification in LArTPCs.

Additional work has been performed in recent years which show that LArTPCs can also utilize a pixel-based readout [75], [76].

The end of the Standard Model era is inevitable. SM simply fails to account for physics with all major frontiers for physicists to accept its completeness; we know there is much and more to learn about nature.

The 20th century saw unprecedented progress in its sophistication of its detectors from ray tubes, to spark chambers, to proportional counters, and to huge (>20 km) particle accelerators. This century shows no signs holding any less promise than its predecessor. Continued development in electronics, computing, and analysis methods will lead to more and newer frontiers of physics.

The work presented in this introduction aims to not only encapsulate the massive progress particle physics has made since the electron's discovery, but also to serve as a reminder of how extraordinarily surprising nature is. At every turn and at every point where physicists think they've arrived at the end (or at an impossible roadblock) there always remains more to discover. If we have learned anything, we have learned to knock and the door shall be opened.

The Deep Underground Neutrino Experiment

The Deep Underground Neutrino Experiment (DUNE) is a long-baseline neutrino beam experiment [3, 7, 16, 77]. DUNE, when constructed, will be composed two detectors, a near detector (ND) and a far detector (FD) which are separated by a distance of 1300 km.

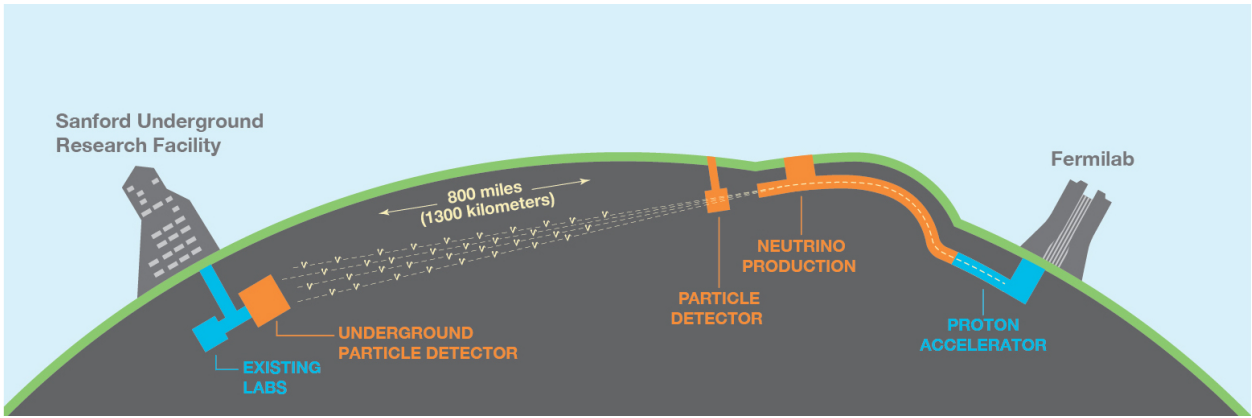


Figure 1.5: Representation of the Near and Far Detectors for the DUNE experiment. The Near Detector is located within the image labeled as the Particle Detector. One of the key purposes for the Near Detector is to tag outgoing particles from the proton beam. Image was taken from [5].

The ND is located at Fermilab and its purpose is to characterize the source neutrino beam created there. The ND serves many purposes. To name a few..TODO

The FD will be placed underground at Sanford Underground Research Facility (SURF) and be approximately 1300 km away from the ND. This detector represents an enormous engineering challenge to place such large, cold, and complicated detector. The FD will be composed of up to four separate 10 kiloton modules.

DUNE plans to offer an incredibly rich searches across the sectors listed above 1.6. We briefly discuss the relevance of some the searches below, but more detailed reading can be pursued at [16].

Two of these four modules at least will use a known wire-based readout technology and a vertical drift-readout. The two remaining modules are considered modules of opportunity and their readout technology is yet unknown. A purpose of this dissertation is show the viability of a novel readout technology.

DUNE has three main science goals, all of which are geared towards pushing beyond the standard model:

- Hadron Decay 1.4
- Core-collapse Supernovae 1.4
- Neutrino Oscillation 1.4

We will discuss the relevance of each of these items, and in chapter 2 where we will further discuss how the work presented here relates to each of these topics.

Conventional horizontal drift detection for foreseeable DUNE modules are already considered possible for lengths up to 6.5m [78].

A NOVEL READOUT TECHNIQUE FOR TPCS: Q-PIX

In this chapter, we introduce a novel pixel-based readout concept for TPCs. Pixel-based readouts offer several advantages over the traditional wire readout [79]. A key improvement offered by pixelization is true 3-D image reconstruction. This allows for sharper vertex reconstruction, improving the overall resolution of DUNE and reducing the time required for an NP measurement.

Other benefits include ease of data analysis and a reduction in the amount of data storage required. A pixel-based readout automatically captures two of the three spatial dimensions for easier analysis. In addition, the pixelated readout method presented here reduces the total data storage required and the data acquisition rate (without loss of accuracy) by potentially several orders of magnitude.

However, these advantages come at the cost of increased design complexity, as the number of readout channels increases by more than three orders of magnitude. The traditional wire-based readout within a DUNE module will have hundreds to thousands of channels, while a full DUNE module with a pixel-based readout will have tens of millions of channels. This number of channels required to provide a stable readout over the expected lifetime of DUNE (≈ 20 years), where the electronics are continuously operating at liquid argon temperatures, is probably the biggest hurdle for a pixel-based design. A goal of this dissertation is to address the channel size problem.

2.1 Q-Pix: The Circuit Level Design

The fundamental readout circuit (2.1) was first introduced by Nygren and Mei [6]. The principle of the front-end circuit operates on measuring the time of the output of a trigger which is connected to an integrating capacitor circuit. The key difference of this readout circuit is that the measured value is time, not voltage or charge. Such a design choice then allows this readout to only provide data when there is charge.

The circuit input is connected to the anode of a TPC where drifted electron charge accumulates. Voltage is then built up from the charge stored on the pixel based on the capacitance according to the equation:

$$Q_i = C_i V_i \quad (2.1)$$

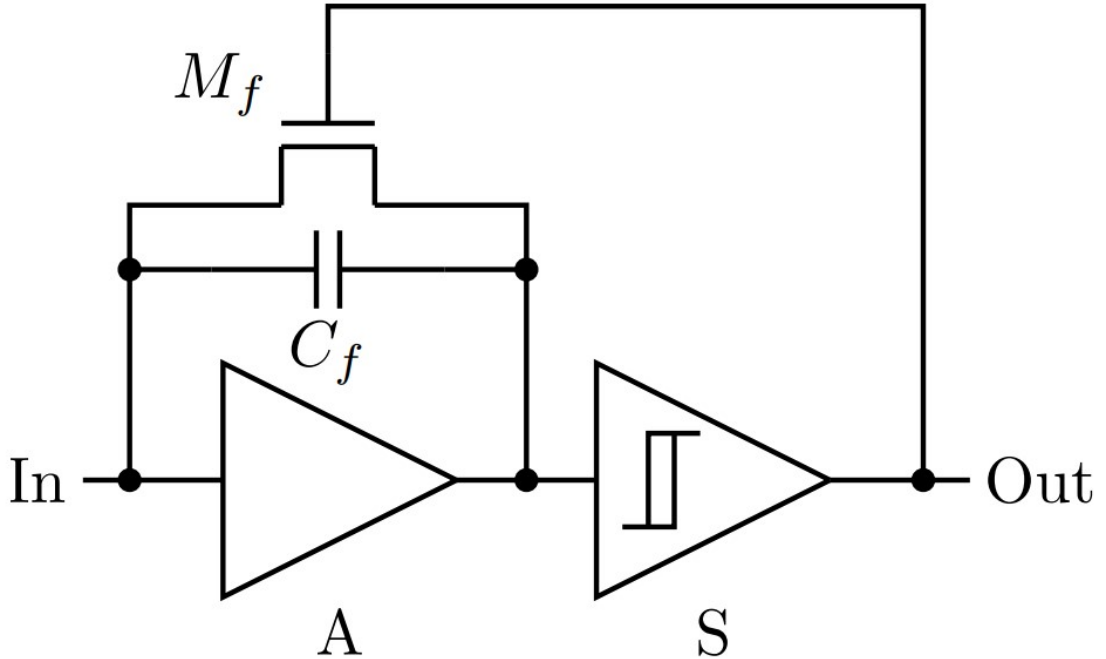


Figure 2.1: Image of Basic Q-Pix Readout circuit. Currently this front-end circuit is being designed as custom analog ASIC which has 16 channels. Image is taken from [6].

After the capacitor voltage (V_i) exceeds a set threshold value the schmitt trigger activates. The time of the trigger output is recorded by a digital logic which encodes this data as a 32 bit value. Since the capacitor reset happens at the same time as the issued trigger the digitally-recorded value is the reset time.

This timestamp value is recorded against a free running local oscillator ($f_o = 30 \text{ MHz}$). The number of free running clocks in the entire system is expected to be the number of channels (N_c) divided by the number of digitally multiplexed channels (N_d), which are taken to be 16.

Waveforms from Time Resets

Here we describe the basic principle of reconstructing the input current from a collection of reset measurements. The key insight for this readout technology is that time (instead of voltage as in a MWPC) is recorded. Therefore, measurements only taken place when there is enough charge to cause a reset which prevents continuous measurements during periods of long dead time. This

concept follows the detector concept of least action in that all measurements are detector responses.

A measurement of a reset indicates that a certain amount of charge was discharged from the integrating capacitor. Since total charge is conserved (and assume drift current around the integrator is small compared to backgrounds), we can say that the total amount of charge that accumulates onto the pixel is equal to total amount of charge discharged from each reset, plus any residual charge still on the pixel. Therefore, we can relate the total accumulated charge to the total charge discharged with the following equation:

$$Q_{in}(t) = Q_{out}(t) + Q_c(t) \quad (2.2)$$

eq:qin)

If we assume that each reset removes the same amount of charge during each reset then we can rewrite the total charge out (Q_{out}) in terms of the integer number of resets at time t ($N(t)$):

$$Q_{out}(t) = Q_o N(t) \quad (2.3)$$

eq:qout)

Where Q_o is the fixed amount of charge discharged during each reset. Equation ?? then can give us the measured current by definition ($I = \frac{dQ}{dt}$):

$$I_o = \frac{d}{dt} (Q_o \times N(t)) = Q_o \frac{dN}{dt} = \frac{Q_o f_o}{N_{clk}} \quad (2.4)$$

eq:irecon)

Where we identify $\frac{dN}{dt} = \frac{f_o}{N_{clk}}$ as the as the clock frequency (f_o) of the local clock and the difference between the two resets. Equation ?? can be used to determine the maximum current with the digital clock frequency by noting that the minimal value of N_{clk} is one. We take as the nominal expected frequency (30 MHz), capacitance (1 fF), and voltage (1 V) values to calculate an approximate max current, I_{max} :

$$I_{max} \approx 1 \text{ fF} * 1 \text{ V} * 30 * 10^6 \text{ MHz} \approx 30 \text{ nA} \quad (2.5)$$

We note that 30 nA is much greater than the expected background current from Ar³⁹ ($\mathcal{O}(10^{-18}) A$). However, more interesting events deposit more more charge. We can use the average drift speed of

electrons in a LArTPC to estimate the maximum charge density such a configuration is sensitive to:

$$\lambda_{max} = \frac{dQ}{dL} = \frac{dQ}{dt} / \frac{dx}{dt} = \frac{I_{max}}{v_{drift}} \quad (2.6)$$

We use a nominal v_{drift} speed of 1.6 mm / μ s, and convert to SI units to obtain λ_{max} in equation 2.1:

$$\lambda_{max} = \frac{3 * 10^{-8} A}{1600 \frac{m}{s}} = 1.875 * 10^{-11} \frac{C}{m} \approx 19 \frac{nC}{mm} \quad (2.7)$$

We can now use this result to calculate a maximum $\frac{dE}{dx}$ measurement:

$$\frac{dE}{dx}_{max} = \frac{dQ}{dx}_{max} \frac{dE}{dQ} = \lambda_{max} \frac{dE}{dQ} \quad (2.8)$$

We can take the ionization energy of Ar³⁹ to be $W_{ion} \approx 23.6 eV$, then:

$$W_{ion} = \frac{23.6 eV}{e^-}$$

and

$$Q = 1.602 * 10^{-19} C$$

Then $\frac{dE}{dQ}$ becomes:

$$\frac{dE}{dQ} = \frac{23.6 eV}{1.602 \times 10^{-19} C} \quad (2.9)$$

Finally, we calculate the result of equation ?? and convert to units of $\frac{GeV}{mm}$.

$$\frac{dE}{dx}_{max} = 1.875 * 10^{-11} \frac{C}{m} \times \frac{23.6 eV}{1.602 \times 10^{-19} C} \approx 2.76 \frac{MeV}{mm} \quad (2.10)$$

Next we aim to provide an estimate on the lower limit of detection for an event. What follows provides a rough estimate for a potential lower bound on signal identification in the analysis, and note that a more thorough investigation of a true lower limit would require more work and beyond the scope of the work presented here.

First, we take as a lower bound estimate that any signal detection for an event purely based on charge reconstruction must provide more resets than background due to Ar^{39} beta-decay. Since the background rate from the dominate source is expected to provide resets of frequency $\approx 1\text{Hz}$, an order of magnitude estimate for the minimal detectable current can be measured if we assume a signal-to-noise ratio (S/N) of 10. Then, a detectable signal rate should deposit enough charge to trigger a reset within a time window of $\approx 0.1\text{s}$.

Following equation ??;

$$I_{min} \approx \frac{1\text{ fF} \times 1\text{ V}}{0.1\text{s}} \approx 10\text{ fA} \quad (2.11)$$

We use I_{min} to calculate an average charge line-density above the pixel, and again assume a constant drift speed, $v_e \approx 0.1601\text{cm}/\mu\text{s}$, from table 1.3.

$$\lambda_{min} = \frac{10^{-14}\text{A}}{1600\frac{\text{m}}{\text{s}}} = 6.25 \times 10^{-18}\frac{\text{C}}{\text{m}} \approx 6.25\frac{a\text{C}}{\text{m}} \quad (2.12)$$

Finally, we calculate the minimum $\frac{dE}{dX}$ following 2.1:

$$\frac{dE}{dx}_{min} = 6.25 \times 10^{-18}\frac{\text{C}}{\text{m}} \times \frac{23.6\text{eV}}{1.602 \times 10^{-19}\text{C}} \approx 0.921\frac{\text{eV}}{\text{mm}} \quad (2.13)$$

Making a 3-D Image

One of the important features of a TPC is the ability to reconstruct full 3-D images. The intended benefit of a pixelated readout on any TPC is to show that there are improvements to reconstruction of these 3-D images.

In order to reconstruct the image of the interaction from a set of data above the pixel the required data are the reset time at a pixel i (T_{ri}), event time (T_e), and the pixel ID. We assume that T_e (as is normally used to tag events in TPCs) uses a trigger time from a secondary PMT system from the scintillation light produced by the interaction to tag an event of interest. Since the scintillation photons travel much faster than the drift electrons, we can use the T_e as the starting time.

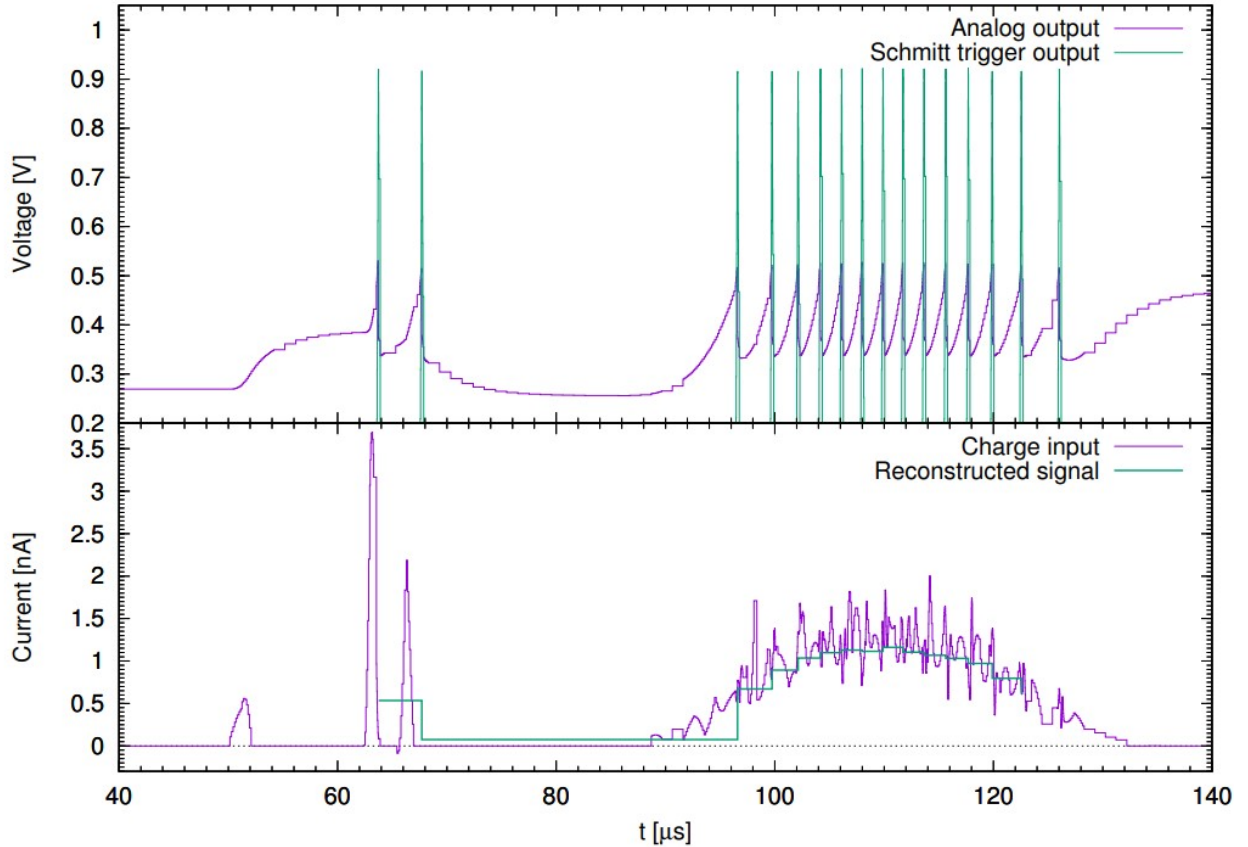


Figure 2.2: Example reconstruction of the reset time difference (RTD) based on the Q-Pix readout design. Image is taken from [6].

The pixel ID of each reset gives two of the three remaining coordinates (\hat{x} and \hat{y}). The last coordinate (\hat{z}) is reconstructed using T_{ri} .

Since the drift velocity of the electrons (v_e) is constant in a TPC the distance that the electrons traveled to reach the anode plane (\hat{z}) is determined based on only the drift time:

$$z = v_e * T_{drift} \quad (2.14)$$

However, this drift time is measured directly from the difference between the event time (T_e) and the reset time for this pixel (T_{ri}).

$$T_{drift} = T_{ri} - T_e \quad (2.15)$$

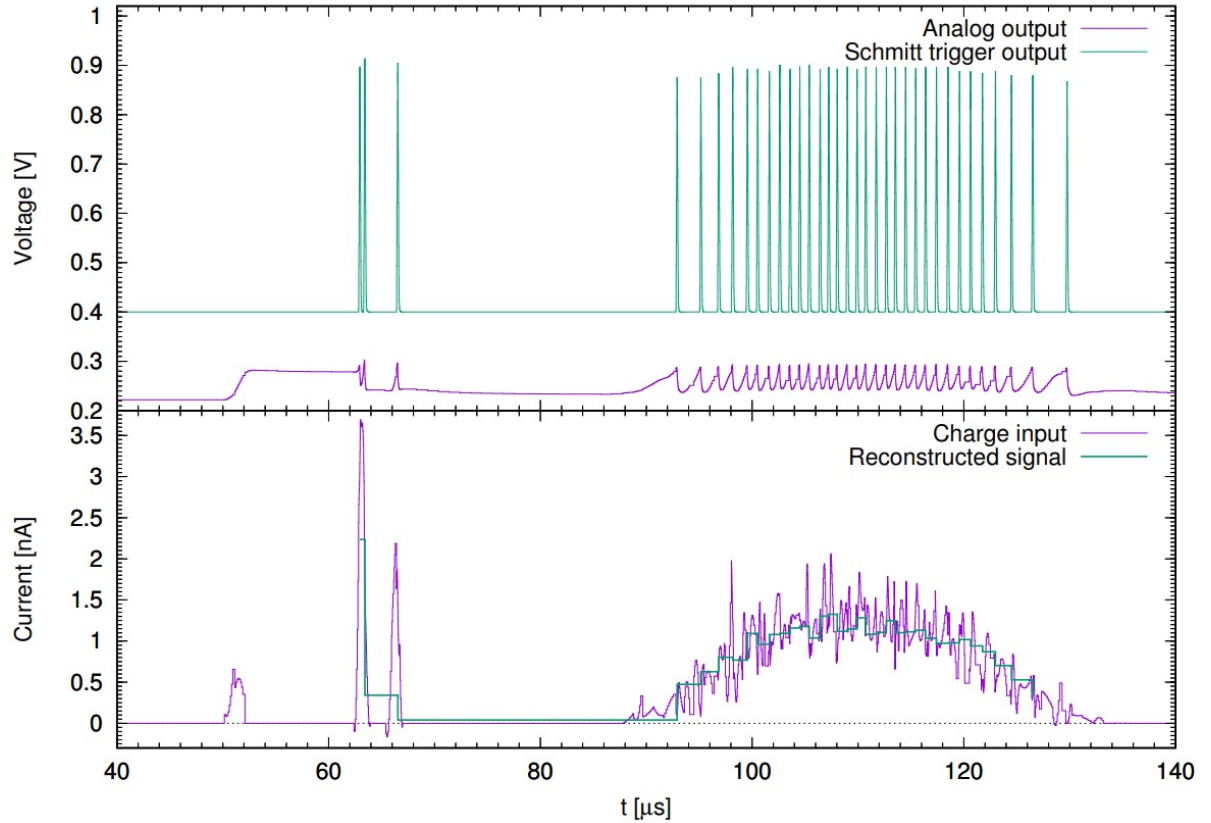


Figure 2.3: Example reconstruction of the reset time difference (RTD) based on the Q-Pix readout design. δQ was chosen to be $0.3 fC$. Image is taken from [6].

The drift distance in equation (2.1) becomes:

$$z = v_e * (T_{ri} - T_e) \quad (2.16)$$

Pixel Calibration

Calibration measurements are essential for any detector, as they provide a means to differentiate signal from noise. Here we briefly describe an automatic use of existing Ar^{39} decays as a source of calibration at the pixel level. A full discussion of simulations using backgrounds is found in 5.

The target volume (LAr) is stable nobel but still provides a quiescent background from the charge deposited β decay (≈ 6 MeV). The total volume continually observed by any pixel a drift distance ≈ 3.5 m yields an average reset on the order of 10s of seconds $O(10^1)$. This value is much lower

than the wrap-around rate of the 32-bit sample clock, which in practice will provide continually increasing reset values and prevent errors in identifying the correct reset time.

The pixel level value which needs to be calibrated is the pixel's response to an input charge Q_{in} in equation 2.1. The capacitance (C_i) for each pixel is a systematic which can be calibrated periodically using the background current from Ar^{39} decay. Given some stable input charge, there is a known number of reset measurements to calibrate against.

LAr purity over the detector volume is essential for background calibration. Differences in purity, electric, and magnetic fields affect the major contributions to charge loss in the LAr: recombination, lifetime, and diffusion.

Bad Scenarios

Here we briefly describe potential issues of the readout circuit presented here.

Near Maximum Reset Rate

Equation 2.1 relates the maximum measurable current (I_{max}) in a QPix system to the frequency of a digital clock.

The general relationship for the current is given in equation 2.1. This can be rewritten explicitly in terms of the number of measured clock counts at the remote ASIC:

$$I_r(N_{clk}) = \frac{Q_o f_o}{N_{clk}} \quad (2.17)$$

Where f_o is the nominal frequency of the free running remote clock, and N_{clk} is the 32-bit encoded timestamp.

We note here that because N_{clk} can only take positive integer values that there can be large uncertainty in the measured currents between the maximum and half of the maximum. That is since $I(t) \simeq 1/N_{clk}$, explicitly measured currents can only be discrete and have large variance for small N_{clk} .

However, these discrete uncertainties can be accounted for after digital processing. An example of a periodic artificial input current of with $I \approx I_{max}/10$ is shown below in Figure 2.1. The reconstructed charge over time is shown in Figure 2.5.

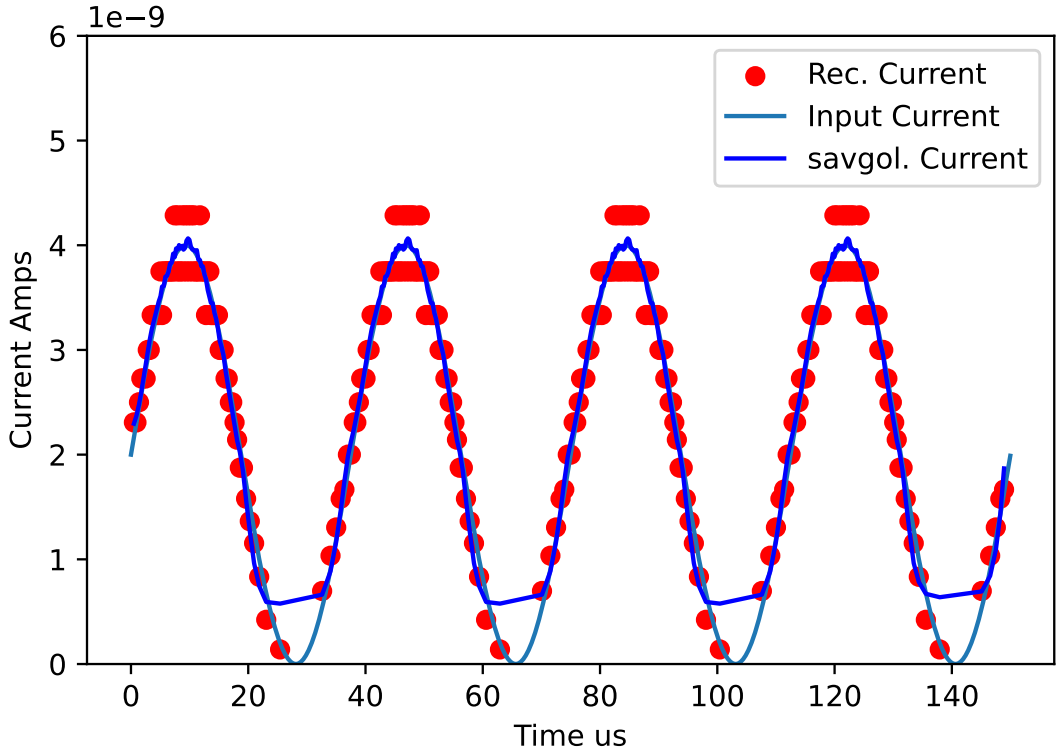
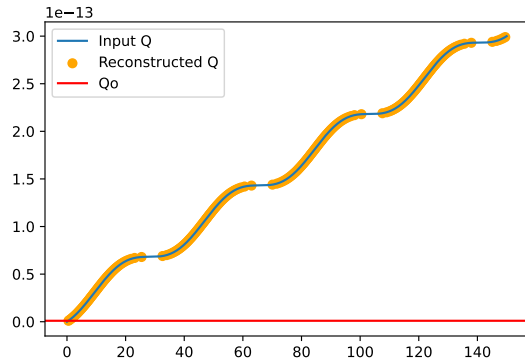


Figure 2.4: Arbitrary sin-wave based current input. Maximum amplitude is chosen to be close to I_{max} . Reset Charge is chosen to be 1 fC and digital clock frequency of 30 MHz. Since the amplitude is close to the maximum, and the clock measurements are necessarily discrete, the exact current can not be measured from reset-to-reset. However, an example of a savgol filter is performed on the resets after the fact, shown in blue, with near agreement of the large input. An use-case of this kind of digital filtering would be applied to large current values only, and not for low current inputs, where the pure timestamp difference provides better results.

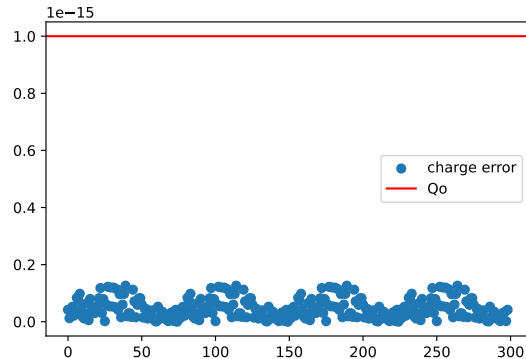
Discussion of Uncertainties

The uncertainty for the two transverse coordinates (\hat{x} and \hat{y}) come from the pixel size. If we assume the electric field to be uniform, on average, across all $O(10^7)$ pixels in an APA, then the charge drift will be uniformly distributed over the pixel size. Then, the pixel dimensions determine the resolution: $\frac{3mm}{\sqrt{12}} \approx 0.87mm$.

The two remaining coordinates to reconstruct tracking are drift distance, \hat{z} , and then time the charge was deposited, T_{ei} . The measurement of \hat{z} is based on equation 2.1. Expanding the uncertainties



((a)) CDF



((b)) Difference

Figure 2.5: Reconstruction of Sub figures CDF of charge as a function of time (a) and difference (b).

based on this equation, and assuming v_e to be a constant, gives us a relation for $\sigma_{\hat{z}}$ to be:

$$\sigma_{\hat{z}} = v_e(\sigma_{T_{ei}} + \sigma_{T_e}) \quad (2.18)$$

Where $\sigma_{T_{ei}}$ and σ_{T_e} are the uncertainties for the reconstructed charge arrival time and the event time, respectively. Of these two, only $\sigma_{T_{ei}}$ depends on the reconstructed charge value; T_e can be provided as an external trigger, such as a photonics system which uses scintillation photons. Such a system can reasonably expected to have a much smaller uncertainty than $\sigma_{T_{ei}}$ since its timescale (ns) is three orders of magnitude smaller.

Therefore, to reasonable approximation $\sigma_{\hat{z}}$ is:

$$\sigma_{\hat{z}} \approx v_e \sigma_{T_{ei}} \quad (2.19)$$

Equation 2.1 relates the uncertainties of the last two coordinates which define a total event reconstruction. A full treatment of the uncertainty in time ($\sigma_{T_{ei}}$) depends on the uncertainty of the measurement of the timestamps for each remote ASIC in a tile, as well as the charge per reset (Q_o) and nominal frequency of the ASIC (f_o). The full treatment to analyze the uncertainty of f_o is the goal of this work and the details are provided in Chapter 4. The measurement of the uncertainty provided by the charge (Q_o) depends strictly on the analog front-end, which is beyond the scope of the work presented here.

We can provide here, however, an order of magnitude estimation based on equation ??, if we consider only the contribution of the uncertainty due to the measurement of time which depends on the number of clocks recorded since the last reset (N_{clk}). Since the measurement of the input current is inversely proportional to N_{clk} , the percent uncertainty of the current measurement is proportional to the percent uncertainty in the timestamp measurement.

A 1% measurement of error can be calculated using a standard percent error definition, and by noting that the maximal error happens when a true current should record a value between $N_{clk} + 1$ and N_{clk} counts. A maximal error of a measured current would happen if the current provides just shy the amount of charge to trigger a reset in N_{clk} cycles and instead the recorded reset occurs on the next clock, $N_{clk} + 1$. The worst case true measurement should be:

$$N_{true} = \frac{1}{N_{clk}} \quad (2.20)$$

We can then directly apply percent error:

$$error = \frac{\frac{1}{N_{true}} - \frac{1}{N_{clk}+1}}{N_{true}} \quad (2.21)$$

Plugging in the value N_{true} from equation 2.1 and simplifying gives:

$$error = \frac{1}{N_{clk} + 1} \quad (2.22)$$

Equation 2.1 provides a general formula for calculating the maximal error due to the discretization of the timestamp measurement. Then, we can solve for N_{clk} to determine how many clock cycles must occur between two resets for a 1% error ($error = \frac{1}{100}$):

$$N_{clk} \approx 100 \quad (2.23)$$

Then after 100 clock cycles, the worst possible measurement of the current is still within 1%. 100 clocks cycles for a 30 MHz clock yields measured drift time $t_{drift} \approx 3.33 \mu\text{s}$. The drift, v_{e^-} is $\approx 1.6 \frac{\text{mm}}{\mu\text{s}}$, multiplied by the time gives the drift distance, known to within 1%:

$$\hat{z} = v_{e^-} t_{drift} \approx 3.33 \cdot 1.6 = 5.33\text{mm} \pm 0.05\text{mm} \quad (2.24)$$

We can rewrite equation 2.1 explicitly in terms of N_{clk} to get a worst case:

$$\hat{z} = v_{e^-} \frac{N_{clk}}{f_o} \quad (2.25)$$

The maximal percent error in the drift distance due to timing increases as N_{clk} decreases, however because the drift distance is also calculated using.

2.2 How Q-Pix fits into a DUNE-FD APA

Here we briefly describe QPix system requirements at DUNE module size (10 kt). A full technical design report for a kt module implementing QPix is clearly beyond the scope of the work presented here, yet we still offer comments on the requirements, particularly on the digital back-end related to a DUNE APA.

The DUNE Far Detector Electronics

DUNE's Anode Plane Assemblies (APA) full description can be found at [7]. Expected noise level of $1000 e^-$. Sampling frequency of 12 bit ADCs is 12 MHz. Expect to collect 20-30 ke^- per channel for a minimum ionizing particle. Large signals require a linear response of $500 ke^-$, and ensures that fewer than 10% of beam events experience saturation.

Dune APA takes 20 Front-End-Motherboards (FEMBs), to digitize a total of 128 wires. 40 wires are taken from the U and V (induction) layers, and 48 wires are taken from the X (conduction) layer. The reason for this distribution is simply that the X layer has a total of 980 wires per APA, where the U/V layers have 800 wires.

Three ASICs are responsible for collecting the charge as it passes between the wires and sending it out of the cryostat. The first ASIC is a waveform-shaping and amplification ASIC. The second ASIC is the ADC ASIC and is responsible for converting the analog signal to digital. The final ASIC, called the COLDATA ASIC, merges the data streams from the previous ASICs and is responsible for communication between the motherboard and the outside world. Maximum expected data collection is to exceed no more than 30 PB/year, which corresponds roughly to $\approx 1Gb/s$ of continuous collection.

Each 10 kT module consists of 150 APAs. Dune expects to draw less than 50 mW per channel, and incur less than 1% dead channels.

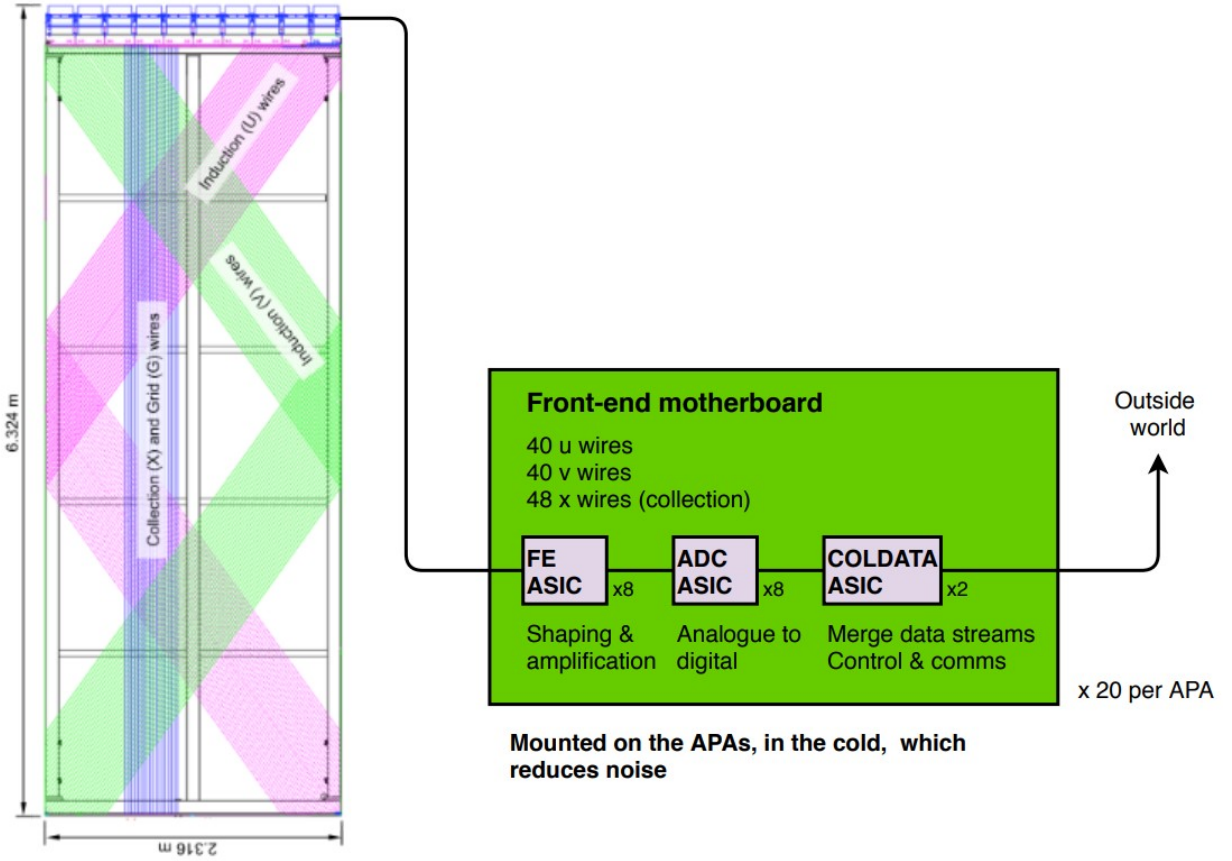


Figure 2.6: Image taken from [7], Fig 1.12 of section 1.8. Image shows an overlay the the relevant charge collection wires within a SP DUNE LArTPC.

Each APA is $6.324 \text{ m} \times 2.316 \text{ m}$, for a total area of 14.646 m^2 . From these dimensions the expected channel count of the QPix readout on the DUNE-FD APA is

$$N_{pix} = 14.646 \text{ m}^2 * \frac{1 \text{ pixel}}{4 \text{ mm}^2} * \frac{1000^2 \text{ mm}^2}{\text{m}^2} = 915399 \quad (2.26)$$

To have a comparable power draw compared to DUNE-FD, which has 2560 channels, then QPix would need less than $\approx 140 \mu\text{W}$ of power draw per channel. Too much energy dissipated in the LAr creates bubbles which is a high voltage (HV) discharge risk. The total channel count for a 10 kT module is based on 150 DUNE-APAs or $2560 \times 150 = 384000$.

Thus, the number of extra analog channels that QPix is required to measure, compared to the typical wire readout, increases by a factor of $915399/2560 \approx 357$. This is an increase of $O(10^3)$ A orders

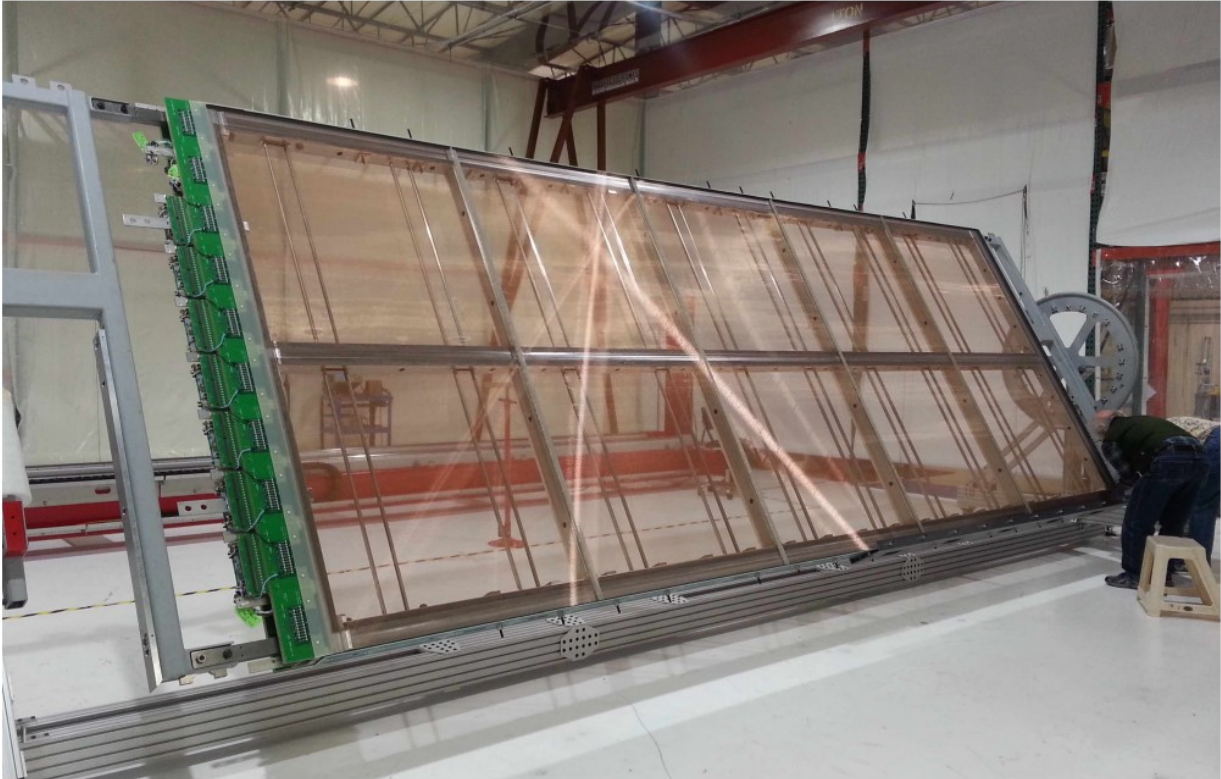


Figure 2.7: A simple caption [7]

of magnitude.

QPix instead offers conversion from analog (charge) to digital (32 bit time) signals on the front-end ASIC. These front-end ASICs are arrayed in tiles, and the tiles themselves would spread out to cover the entire area of an APA. Each tile would interface with a single FPGA chip which would concentrate the digital data for each tile; we refer to this FPGA as the DAQ-Node (DN). Then, each DAQ-Node interfaces with at least a single concentrator FPGA that sends the digital data to the Warm-Interface-Cards (WIC) out of the cold electronics (CE). The final concentrator FPGA we refer to as the Super-DAQ-node (SDN).

The exact description and characterization of the WIC for a QPix depends on the final implementation of the SDN and is thus beyond the scope of the presented here.

2.3 The digital back-end

| Description | Specification | Rationale |
|--|-------------------------------|---|
| System Noise | $< 1000 e^-$ | Provides >5:1 S/N on induction planes for pattern recognition and two-track separation. |
| Signal Saturation | $500,000 e^-$ | Maintain calorimetric performance for multi-proton final state. |
| Cold Electronics Power Consumption | $< 50 \text{ mW pre channel}$ | No bubbles in LAr to reduce HV discharge risk |
| Number of Channels per front-end motherboard | 128 | The total number of wires on one side of an APA, 1,280, must be an integer multiple of the number of channels on the FEMBs. |
| Maximum diameter of conduit enclosing the cold cables while they are routed through the APA frame. | 6.35 cm (2.5") | Avoid the need for further changes to the APA frame and for routing the cables along the cryostat walls |

Table 2.1: Selected Requirements of DUNE-FD TPC electronics and Expected QPix Design goals of first generation ASIC development for comparison. TPC electronic data and rationale are taken from [7]

We define the digital back-end as the part of the larger Q-Pix readout system that is responsible for handling the data after a reset is recorded. This sub-system must be able to record and store data, be robust against SPF, define error states, and more.

Initial Desgin Choices

All first designs require choices; the digital back-end is no exception. In order to make any set of first choices there must be a definition for a successful design. Table

We consider that the digital blocks responsible for digitizing the reset to have a nominal frequency of $\approx 30MHz$. Therefore, the minimum time before the recorded timestamp value resets is calculated by:

| Parameter Name | Value | Description |
|----------------------------|---------------------|-----------------|
| Total Number of Nodes | Pixel Dependent | Based on Pixels |
| Local Oscillator Frequency | Fixed | 30 |
| Input Connections | Fixed | val |
| Communication Protocol | Endeavor | val |
| Configuration Connections | Eventually TBD | val |
| Local Counter Bits | 32 | val |
| Local Buffer Depth | 64 | val |
| Remote Buffer Depth | 256TBD, here | val |
| Configuration Registers | Fixed, possibly TBD | 8 |
| State Machine Logic | Fixed, but Tested | val |
| Tile Size | TBD, here | val |
| Aggregator Connection | Fixed, here | val |
| Interface to Warm | TBD, | val |

Table 2.2: Design Parameters

$$T_{loop} = \frac{2^{32}}{30 \times 10^6} \approx 143 \text{ seconds} \quad (2.27)$$

This time (T_{loop}) indicates the minimum reset time to occur within each responsible digital block. Since this time is much greater than the anticipated reset rates to be produced from backgrounds, discussed in section 2.1, we expect the looping of the 32-bit recorded value to not present a design concern.

The total number of free running oscillators (N_{osc}) per DUNE-APA for a given pixel pixel of 4 mm^2 is:

$$N_{osc} = \frac{915399}{16} \approx 57213 \quad (2.28)$$

N_{osc} represents the total number of front-end ASICs whose data must be aggregated and sent outside of the cold electronics to a warm interface. Therefore we expect the order of the number of free running oscillators per DUNE-APA $O(10^5)$. This also gives an order of magnitude estimate of the increase of number of ASICs compared to the MWPC readout of Single-Phase (SP) DUNE-FD.

Figure 2.2 shows that each APA uses 20 FEMBs to digitize 128 of the 2560 channels. Each FEMB houses a total of 18 ASICs which smooth, digitize, and aggregate data before being sent to the

| Description | Specification | Rationale |
|--|--------------------------------|---|
| System Noise | $\approx 300e^-$ | Provides $\approx 17:1$ S/N ratio, a component of front-end integrator. |
| Signal Saturation | >30 nA? | Upper limit from local oscillator frequency and integrator reset. |
| Cold Electronics Power Consumption | < $100\mu\text{W}$ per channel | Equivalent power consumption for heating |
| Number of Channels per Tile | ?? | Design parameter to be calculated. |
| Maximum diameter of conduit enclosing the cold cables while they are routed through the APA frame. | 6.35 cm (2.5") | Same as [7], an engineering goal is to aim to use existing APA frame designs. |

Table 2.3: Q-Pix based Requirements, which can be compared against 2.2. Results here are necessarily speculative, but provide a design goal baseline.

Warm Interface CRATE (WIC). The total number of ASICs per APA is $18 \times 20 = 360$. Since each 10 kt module uses 150 APAs the total number of ASICs would be multiplied by 150.

The goal of a digital back-end design is how to handle the data from the 10^5 free running oscillators, and how to ensure that the free running local oscillator clocks can be calibrated to a known frequency. Additionally,

Single Point Failures

Here we comment on an overall design guideline for Q-Pix: “robust resilience” against single point failure (SPF). The readout technology presented here relies on huge numbers of readout channels (10^8) compared to current MWPC designs (10^5). As such, extra care must be made in designing new technology to improve over established, seemingly simpler means.

This principal guides design choices such as the use of independent local oscillators at the pixel-level instead of a provided distributed clock. This design choice, in particular, is discussed at length in chapter 4, and the findings presented there are one of the major contributions presented in this work.

The design which avoids SPF and handles the digital requirements presented here, namely: the continual time calibration of each local oscillator ($N_{osc} \approx 10^5$) is a goal of this work.

2.4 Q-Pix and Light Detection

Other recent progress [8] has been made towards inclusion of an optical system combined the readout technology presented here. Such a system would integrate well with a charge-integrate-reset style presented here, as the charge collection area is much smaller than the total pixel area. The pixel dimensions are 4 mm \times 4 mm for a total active area of 16mm². Most of this active area is unused for the charge collection pad, which could be as small as drill-hole via (6 mil $<<$ 16mm²). Then, most of the remaining area could be plated with a photo-sensitive material.

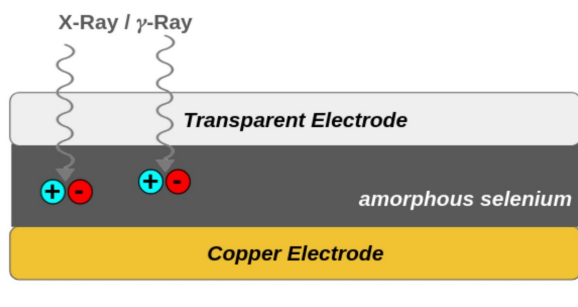
Such a photosensitive material could capture incoming scintillation photons and provide an additional voltage measurement at each pixel. Depending on the sensitivity, such a measurement could be used to reconstruct tracks by providing a $\frac{dE}{dx}$ measurement, or even as a time-tag and a trigger.

The use of a reference trigger could be useful to establish event-time within the same system, and allow adjacent pixels which would receive photons, but not charge, to contribute to time reconstruction. Any reconstructed event requires some T_o time to indicate the start of the event. Typically this is done via scintillation photons from a secondary system, where the photons arrive nearly instantly at the collection planes compared to the slow drift speed of the electrons.

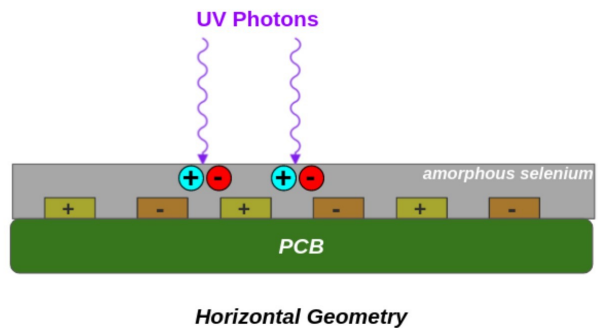
The natural pixelization of QPix required the charge collection can also be used to be sensitive to scintillation photons. These photons could not only provide the required event timing but also provide an additional means of calorimetry and track reconstruction. Additional work is currently underway to demonstrate the viability.

2.5 Q-Pix at "Low" Energy: Supernova Studies

Work has been done to understand how a Q-Pix based DUNE-FD would measure core collapse supernovae [14]. Simulation studies which involved particle interactions were based on Geant4 [80].



Vertical Geometry



Horizontal Geometry

((a))

((b))

Figure 2.8: Images taken from [8].

THE FIRST PROTOTYPE: FIRST RESETS AND LEAKAGE MEASUREMENTS

In this chapter, we present the first implementation of the Q-Pix-based design using off-the-shelf electronics.

This section describes the first prototype based on the Q-Pix readout: The Simplified Analog Q-Pix (SAQ). First we discuss the design goals of the prototype and highlight the basic building blocks of any Q-Pix based prototype. Next, We describe the prototype status as well as lessons learned in characterizing noise and performing calibrations.

In the final part of this section we describe the future goals of this prototype, including the addition of GEMs to the experimental setup. The full results of the planned diffusion measurements are beyond the scope of this work, but we provide the initial details here because these measurements will ultimately provide the complete description of the prototype.

3.1 Simplified Analog Q-Pix: System Design

The SAQ prototype is designed as a first physical proof-of-concept for a Q-Pix readout. The intended use

3.2 The SAQ Prototype Design

The TPC Design

The Integrator Circuit

The SAQ Data Acquisition

All resets are recorded via a Zybo-Z7-20 Digilent FPGA prototype board, which uses an Artix Zynq based architecture. The reference manual for the Zybo Z7 board used in SAQ can be found at

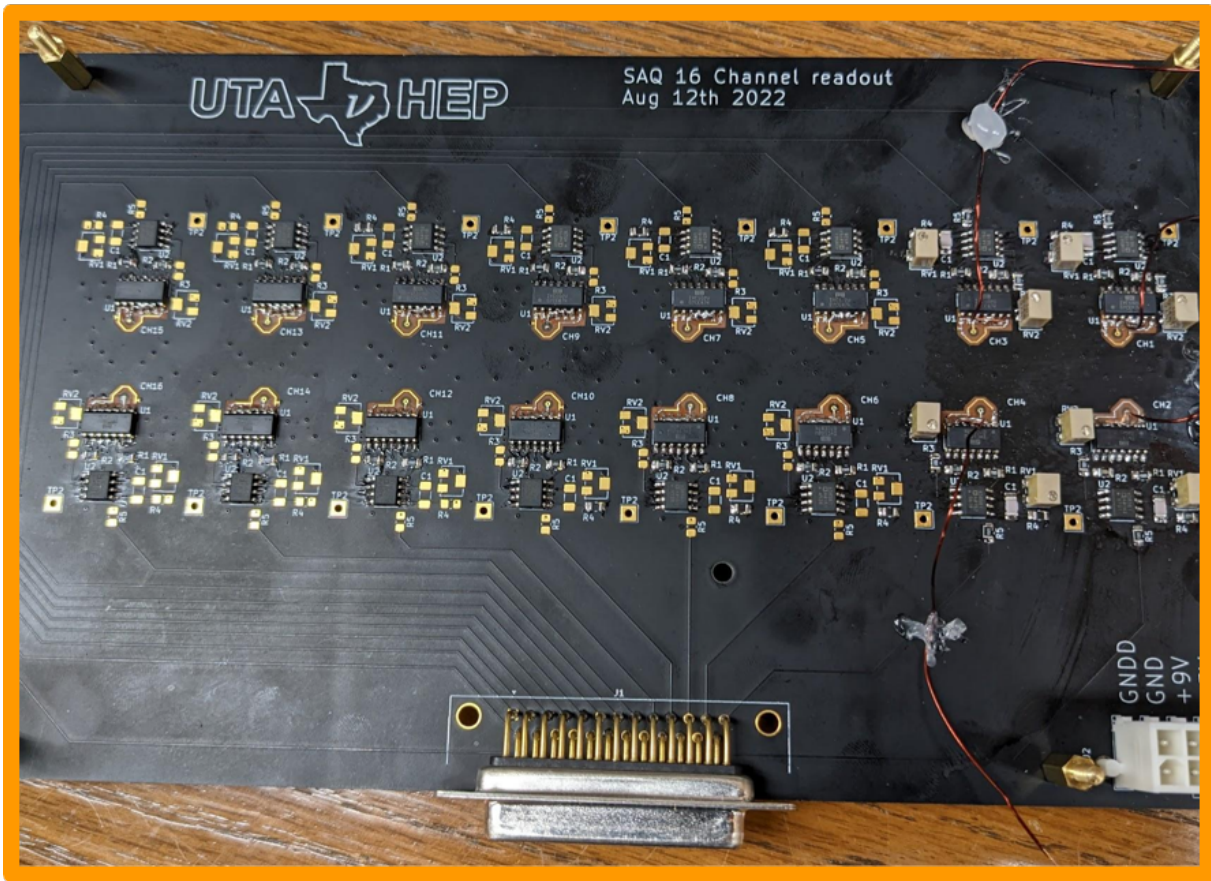


Figure 3.1: The SAQ Setup model based on ??.

[81].

3.3 Noise Measurements

The Q-Pix readout is dependent on the integrator, which provides the basic datum of the reset time. Therefore, a dominant source of noise are electrons which accumulate on the integrator which are not signal electrons. There are two possible sources for these noise electrons: excess electrons produced from the target volume or leakage current due to transistor effects from the integrator circuit. In this section we focus on the noise electrons due to the leakage current.

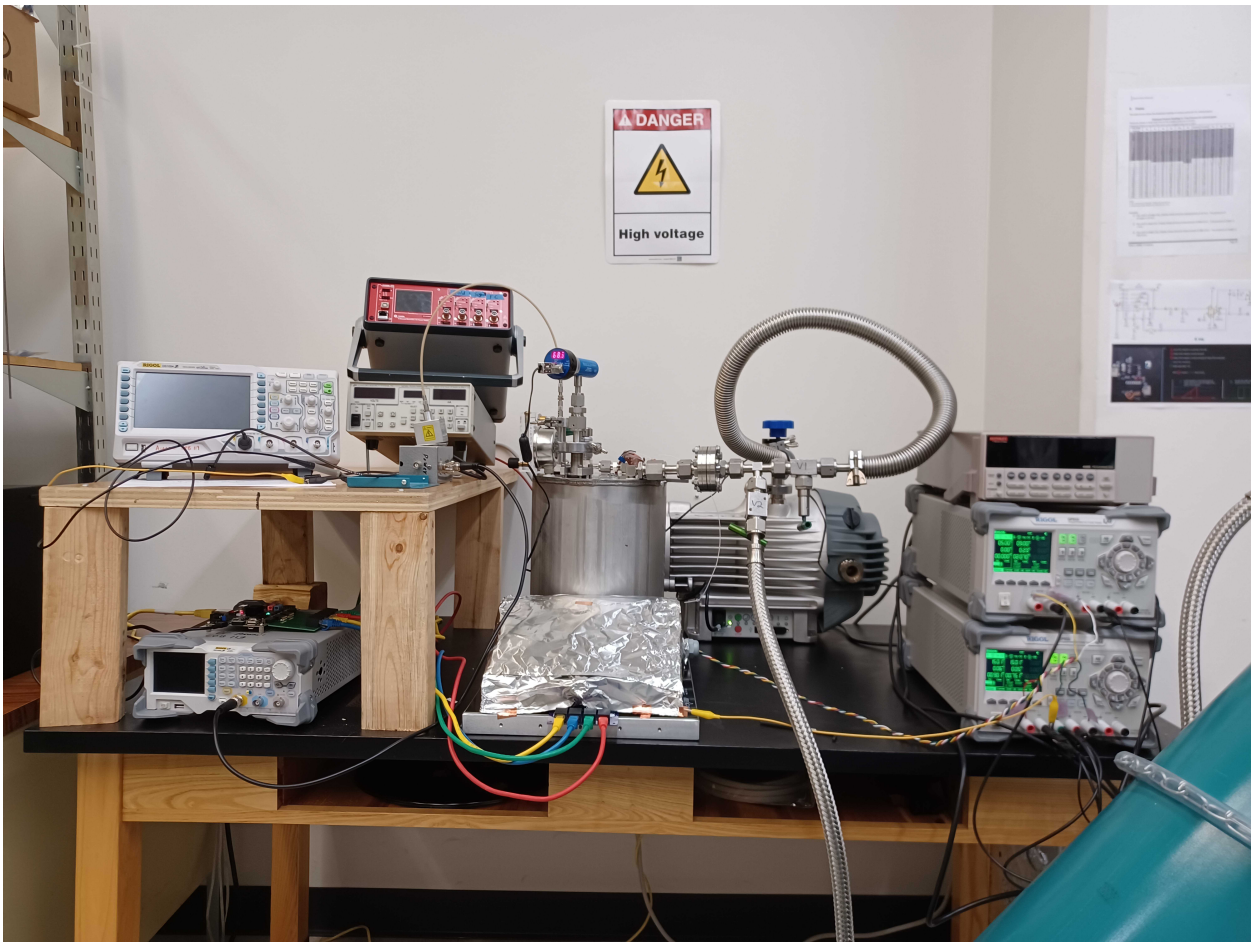


Figure 3.2: The SAQ Setup model based on ??.

Integrating towards background Current

Leakage current arises due to non-ideal behavior of the integrator operational amplifier, where the voltage across the two input terminals is nonzero. Measurements of this leakage current then are performed by measuring voltage difference across the terminals as well as directly using a pico-ammeter.

Integrating towards background Current

The second source of noise electrons are produced from the target volume. The target volume is an ultra pure Argon Gas at TODO millitorr. In this case the excess electrons come from the nominal decay of Ar-39, which provide excess electrons from the natural β decay, at a rate of $\approx 1 \text{ BqKg}^{-1}$

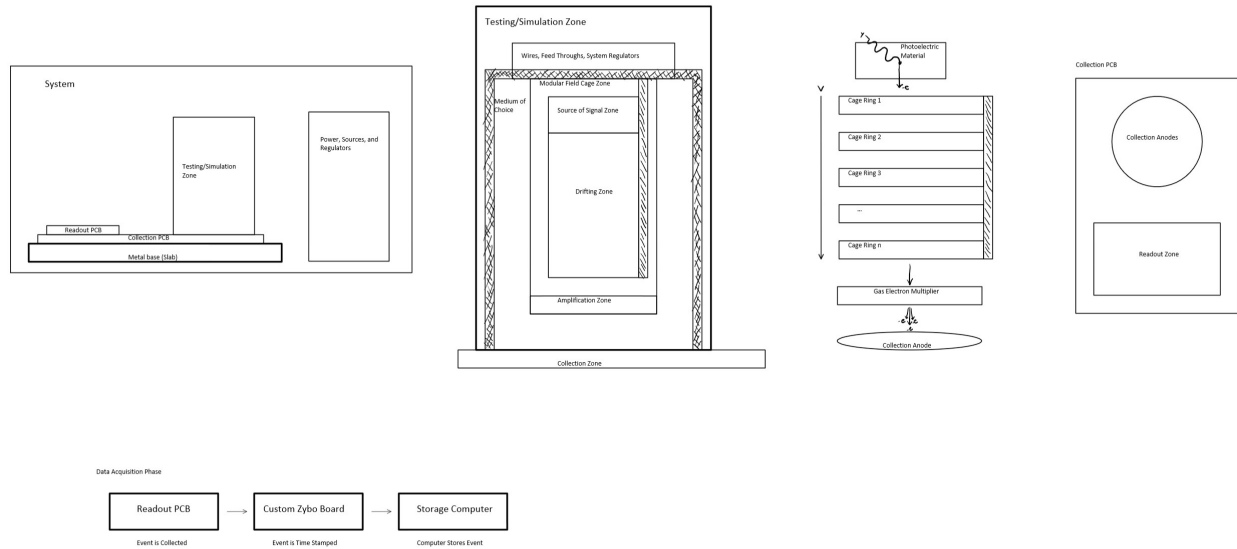


Figure 3.3: The SAQ Setup model based on ??.

Digital Noise Sources and Clock Stability

3.4 Xenon Gas Lamp Measurements

3.5 Results and Discussion

Current Status and Planned Measurements

Measurements of Transverse and Longitudinal diffusion of electrons within electric fields of strength 500 V/cm have been performed before [82].

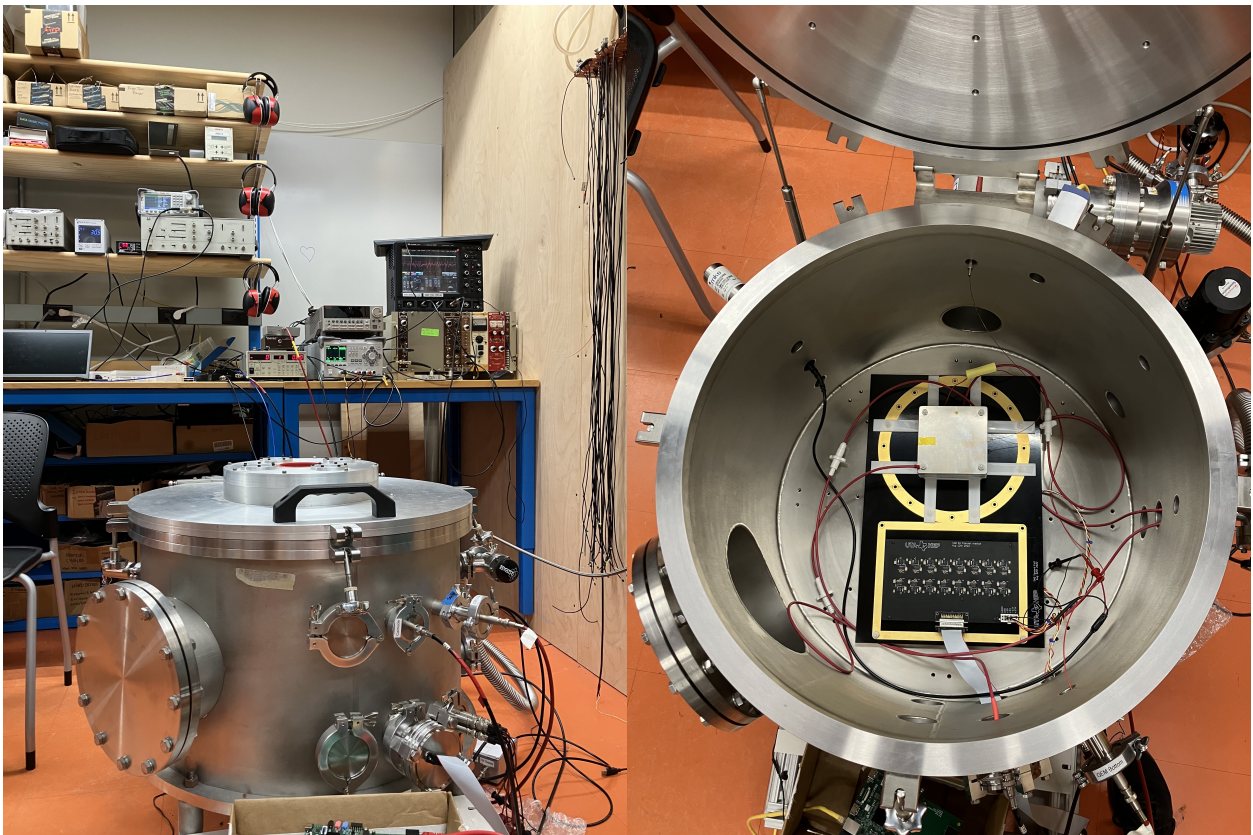


Figure 3.4: Picture of the TPC and DAQ setups at Wellesley University.

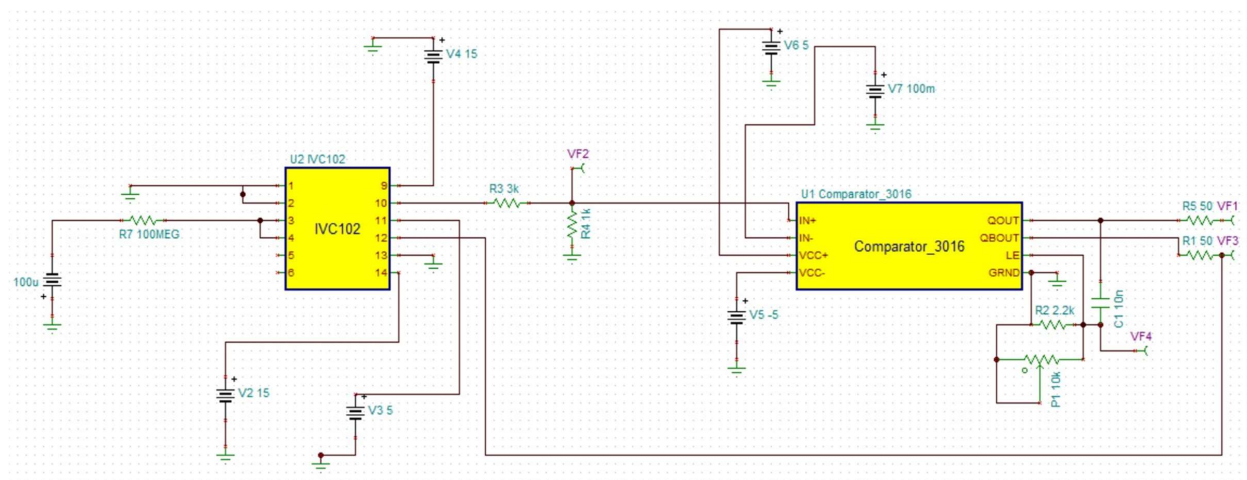


Figure 3.5: The SAQ circuit in a Spice Simulation. The IVC [9] chip chosen as the off-the-shelf integrator for this experiment. The main selection choice for this part is due to its low input bias current $\ll 750 \text{ fA}$.

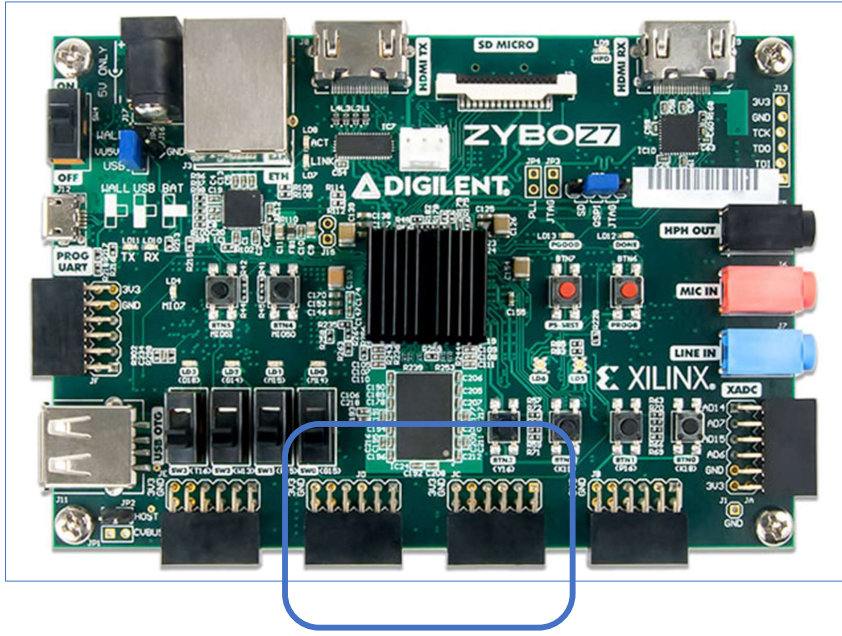


Figure 3.6: An image of the data acquisition board from Digilent, Zybo Z7-20. This board was chosen for its multiple configurable input channels, as well as the Zynq-based architecture of the onboard FPGA. Additionally, the use of the ethernet provides 1 GB transfer speeds, which is more than sufficient for the application.

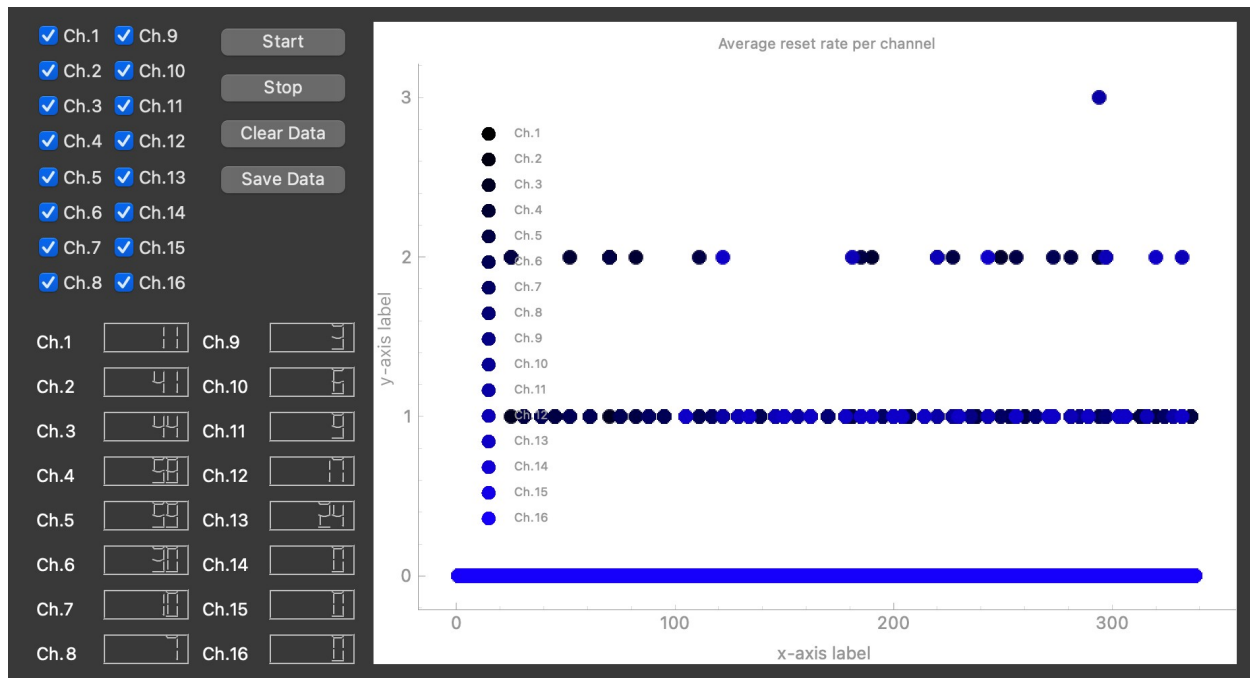


Figure 3.7: The SAQ GUI with real time plotting of incoming resets to the Zybo board.

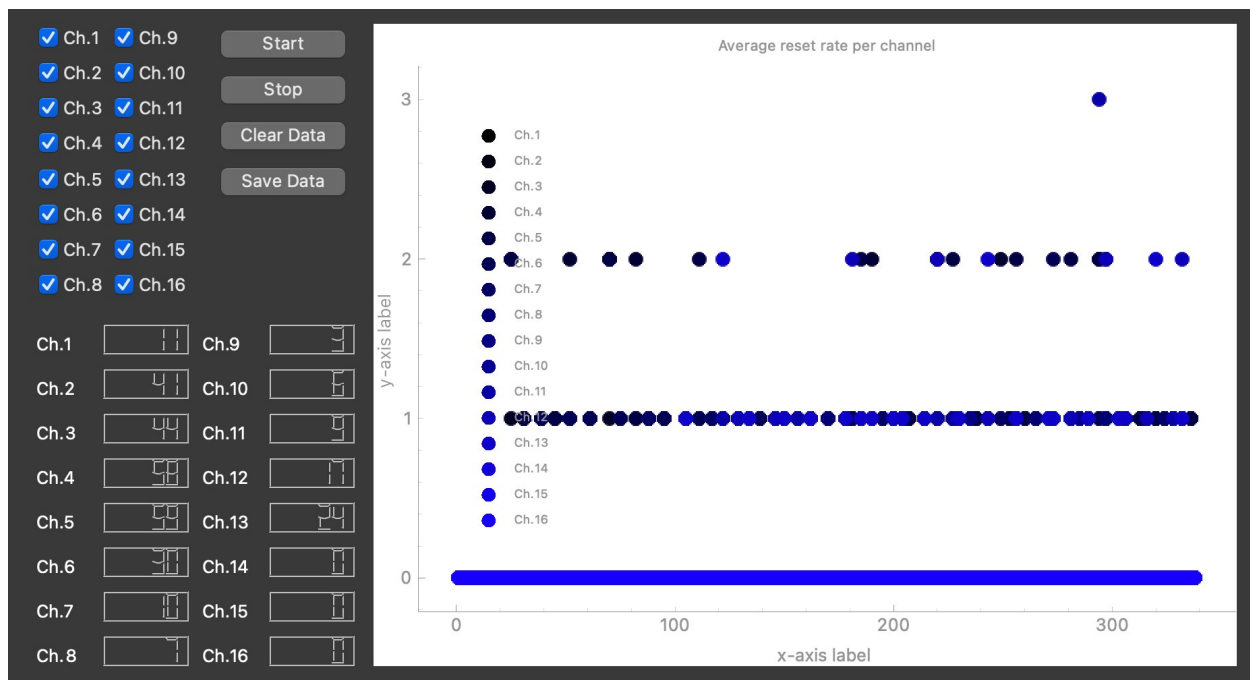


Figure 3.8: Drift Current Measurements to go here.

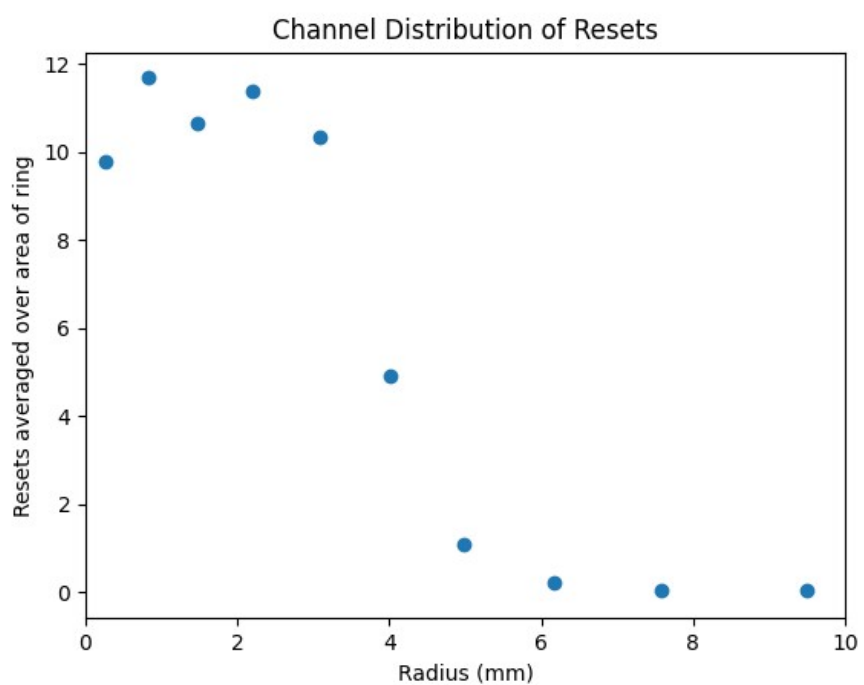


Figure 3.9: First diffusion measurement in P-10 gas performed at Wellesy University.

DIGITAL BACK-END VIABILITY STUDIES

In this chapter we describe the overall structure of the digital back-end of the Q-Pix design as well as results from prototype board tests. As described in previous chapters, the digital back-end of the Q-Pix readout is composed of an array of ASICs (FPGAs, here), which we refer to here to as digital nodes. Each digital node in the prototype array is implemented as a lattice ice40UP5k FPGA.

This chapter is divided into two parts. The first part we give a detailed description of the requirements of a successful deployment digital system in a Q-Pix based detector at DUNE APA scales. The motivation is to describe how the digital back-end of Q-Pix based readout would eventually scale into a DUNE-FD LArTPC 10 kT module.

The second part of this chapter is dedicated to the first evaluation boards developed and tested which implement the digital nodes in Lattice iCE40UP FGPAs [83]. The second part also outlines the design of the PCB on which these FPGAs are implemented, as well as results, which are motivated from the first part of this chapter.

The Lattice Semiconductor FPGAs [83] were selected because of the small form factor, pin out, availability, as well as low power consumption. There are planned tests for future, but not presented here, to indicate its viability of over-the-counter FPGAs in LArTPC. If such cheap and available FPGAs were shown to be reliable use in a LArTPC environment, that could influence future detector development and the selection of the digital chip for the Q-Pix readout.

All results presented in this chapter are my own individual work.

4.1 Digital Design Overview

The digital system of the Q-Pix readout begins when the first digital data are recorded. This occurs during the collection of a recorded timestamp in response to the logic reset pulse sent from the integrating analog front-end. This record happens in response to output reset-pulse sent from any one, or more, of the pixels. Then, the timestamp record is the value of a local 32-bit counter at the time the node receives the reset pulse. When a reset occurs the data recorded are the reset values of each pixel, and the only data required for a full analysis of all reconstruction with a LArTPC are:

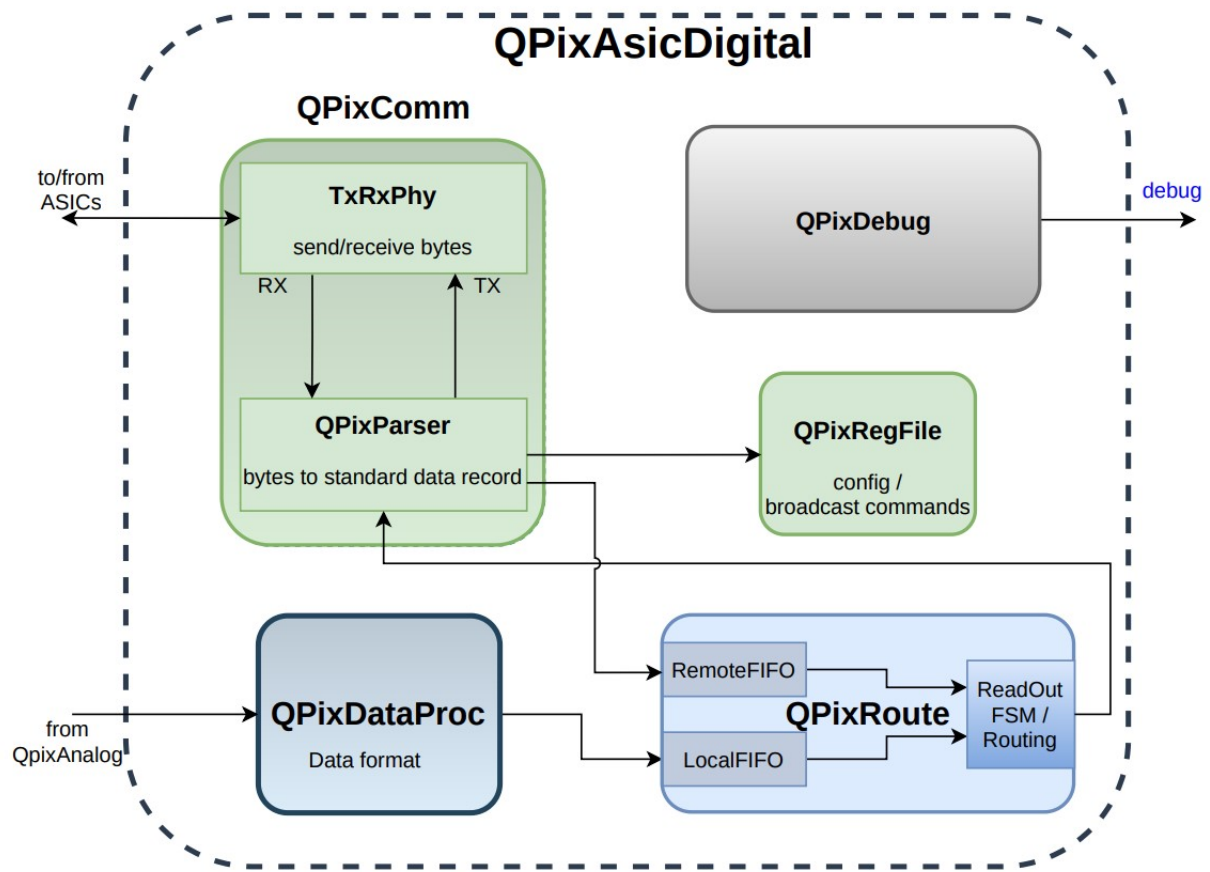


Figure 4.1: Diagram of the Digital node. The controlling sections of the logic for the digital node are QpixComm, QpixDataProc, QpixRoute, and QpixRegFile. The Comm layer is responsible for routing packets between the physical layer and handles the parsing of incoming data packets. The DataProc layer is responsible for recording timestamp data during a reset from the analog front-end. The RegFile contains configuration information, such as routing. QpixRoute determines the controlling state machine that, based on register configurations, determines what packets are sent to which neighboring nodes.

Each of these remote ASICs are running on free-running independent clocks, designed with a frequency of 30 MHz.

Communications

The QpixComm module controls incoming and outgoing packet logic.

The logic responsible for indentifying how an incoming packet is handled is defined in QPixParser. When a valid 64 bit packet has been received, a valid signal is thrown high. The packet is handled based on the bits within the header of this packet. How the packet is handled is determined the by the packet header [4.1](#).

Packets are only comprehensable for types if the same region of the 64 bits are ubiquitous. For this purpose all packets use or reserve the same 20 bits, with four bits reserved for the packet type:

- Unused, 60–63
- Header, 56–59
- X Location, 36–39
- Y Location, 32–35

If the packet originated from the aggregator node then this packet is treated as a broadcast. Broadcast commands record unique numbers associated with this request and are also sent to all connected neighborhoods except from the direction that the broadcast is received. A unique broadcast number is used to avoid registering the same request.

If the packet was not from an aggregator node, then this packet is treated as remote data from a neighbor node. All data transfers of any kind are treated so that all communication happens between individual nodes and an aggregator node. Therefore, any packet that originates on a node that isn't the aggregator node will be sent to the aggregator node. The direction of that this packet is sent is deteremined by a configuration register.

The Structure of a Data Word

Each digital node responds to a successful transmission of a 64-bit packet. We choose that each packet, regardless of type, be 64-bits to reduce the overall packet checking complexity on each node. The type of the packet then is selected by the word type, which is reserved for a static 4 bits within each 64-bit word. This allows for a total amount of 16 unique packets each of which may be handled differently.

A successful transmission of a data word is indicated by the protocol when the correct number of bits have been read (see Section 4.1). When a correct packet is filled a single flag is raised to indicate that the word is valid, and then the appropriate logic parses the header bits of the packet and determines how the packet should be handled.

There are two main types of packets that a digital node would receive, a register request or a data word from another node. In the first case, the register request indicates that this packet originated from the aggregator node and may either go to a specific node or a broadcast to the entire array. Whether or not the register request is a broadcast is checked against another bit, and the packet is handled accordingly. If the packet is a broadcast, the receiving node records an identification number associated with the broadcast, which it uses to ignore additional packets it may receive that correspond to the same broadcast.

The second kind of packet the digital node may receive is a data type word. In the case of data words, there are also two main types: a word which contains the 32 bit timestamp or an event end word. The 32 bit timestamp data word are the words which must eventually make it to disk for analysis. The data words must also encode the row and column position of the original nodes.

Configuration

The configuration of the digital node is handled through local registers. These registers are described within QpixRegFile module, shown in Figure. 4.1. These registers include the ability to control routing of data packets, reset, enable, and channel masking. The Table ?? describes the implemented register addresses and their functions:

The composition of any register word is shown in Table 4.1.

Local Data Collection

The digital node is responsible for collecting and storing local timestamps in response to pixel resets as well as being able to communicate these data with neighbor nodes. The node must be able

| Address | Name | Function |
|---------|---------------|---|
| 0x01 | Command | Used to broadcast type or trigger |
| 0x03 | Routing | Allows selection between manual or dynamic routing. |
| 0x04 | Channel Mask | Selection of mask prevents triggers from masked channels. |
| 0x05 | Position | Allows configuration of X and Y coordinates of node. |
| 0x06 | Disable | Selection of which neighbor node inputs are ignored. |
| 0x08 | Local Disable | Selection of which input and out neighbor nodes can be ignored. |

Table 4.1: The address values are not sequential because some registers have become deprecated through development.

| Bit Location | Name | Function |
|--------------|----------------------|---|
| 0–15 | Data | Excess bits |
| 16–31 | Address | Excess bits |
| 40–43 | Y Position Transfers | Next Y position in tile. |
| 44–47 | X Position Transfers | Next X position in tile. |
| 48 | Source Flag | Single Bit flag to indicate whether or not packet originated from aggregator. |
| 49–52 | Request ID | Identifier bits to specify broadcast. |
| 53 | Destination Flag | Identifier bit to specify if broadcast is meant for a specific node. |
| 54 | Read Flag | Identifier flag to specify if register request is a read. |
| 55 | Write Flag | Identifier flag to specify if register request is a write. |

Table 4.2: Description of the bit values within the register request word.

to buffer data so as to prevent packet loss during transactions. The separation of the remote and local packets are contained within two different FIFOs, as shown in Figure 4.1.

There are two conditions which must be met in order for a timestamp to be recorded. First, an incoming reset pulse must be supplied from one of the pixels. Second, at the time of this incoming reset the corresponding pixel mask must not be set in the channel mask register (See Table 4.1). When both conditions the value of the local reset is recorded into a 32 bit wide FIFO shown in QpixRoute in Figure 4.1.

The composition of the data word is shown in Table 4.1.

| Bit Location | Name | Function |
|--------------|-------------|---|
| 0–31 | Timestamp | Basic Datum which records the local counter at the time of the reset pulse. |
| 32–35 | Y Position | Assigned Y position in tile. |
| 36–39 | X Position | Assigned X position in tile. |
| 40–55 | Pixel Mask | Pixels which were issuing a reset at this time. |
| 56–59 | Word Header | Header value, which is command to all packets. |
| 60–63 | Reserved | Unused bits for all packets. |

Table 4.3: Data word composition.

The Local Data Packet

The transmission of the reset data from the local FIFO to adjacent neighbor nodes begins when an incoming register request from the aggregator is received. This request is supplied as register request to the command register (4.1). This request may be considered either a “hard” or a “soft” interrogation command.

The difference between the two types of an interrogation command is whether or not the event end packet is created. In the case of a “hard”–interrogation, the event end packet is always created, regardless of the local FIFO. In the case of a “soft”–interrogation, the event end packet is created only if the local FIFO is not empty.

The use of two different types of interrogations allows the aggregator control flexibility in how many packets are created during an interrogation. Interrogations may happen on timescales much more quickly than expected resent pulses ($O(10^1)$ s), Chapter ??). The ability to request data only if available prevents an over abundance of packets which prevents needless data transfers, reduces remote FIFO buildup, and conserves power.

The Event End Packet

The event end words perform multiple functions. First, they may used as checksums to indicate at the aggregator node, or on disk, that this node has successfully transmitted all of its data. Secondly, the event end word, since it is necessarily 64 bits long, may also transmit its own timestamp with the excess bits. The timestamp that the event end word carries is the time that the time that the node received the broadcast. This timestamp is used in the frequency calibration of the node; the

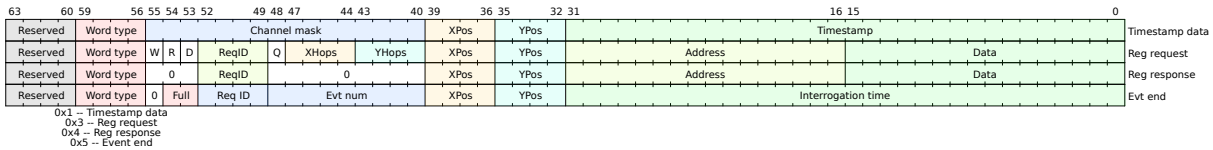


Figure 4.2: Example of Datum words and their allocation as currently implemented in the simulation and first prototypes.

method for calibration is described in greater detail in Section 4.6.

Debug and Future ASIC Prototypes

Finally, The last block in Figure. 4.1 is the QPixDebug. This portion is used to expose certain ports to the physical pins in a digital ASIC design. This design will be the first prototype of the digital ASIC, and is beyond the scope of the work presented here, but will be discussed in the final section of this thesis.

Inter-Node communication via endeavor protocol

The Endeavor protocol is a bi-directional serial communication protocol which allows communication between asynchronous devices. The asynchronous communication is achieved by extending the length of time that each bit is sent between the two devices. In this protocol the way that the receiving node (RXN) identifies the correct logic value of the current bit is by counting the number of clocks that the incoming signal is logic high. The incoming bit is either a logic low, if held high for fewer clocks than it would be if it was an incoming logic high. The number of clocks which correspond to high and low must be programmed beforehand and are tunable parameters.

Basic System Requirements

The sheer number of pixels required for an APA (and the 10 kT entire module) require an effective means of charge and time calibration, stable buffer depths, and protection against single-point failure (SPF). Resets are records of a local counter at the current node and are recorded in response to a reset pulse sent from a pixel.

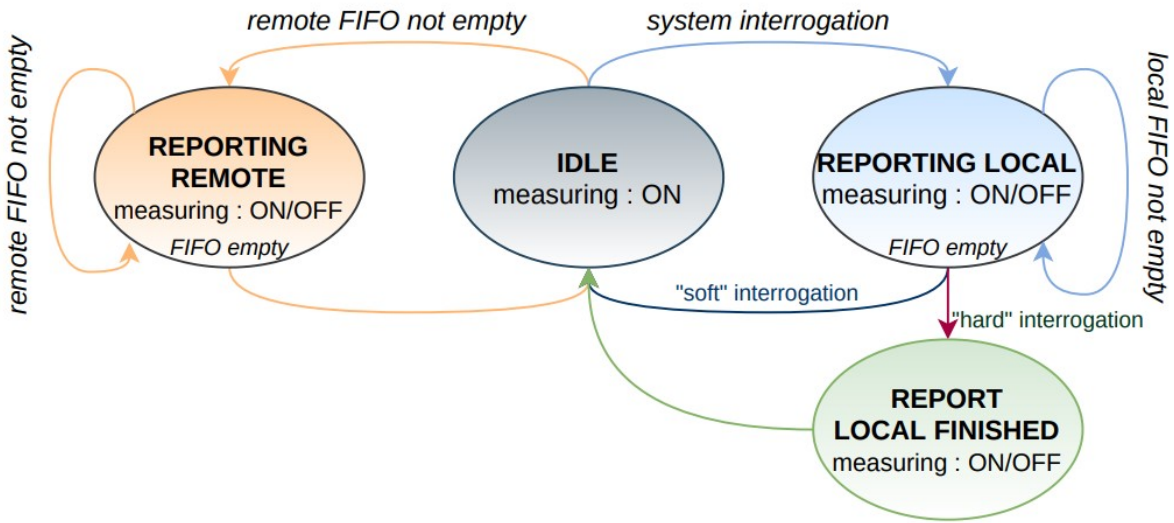


Figure 4.3: Diagram of the Digital node's FSM which determines how to respond to incoming packets.

Comments on Data Rates and required Computing

Based on the minimum number of bits for each RTD ?? we can estimate minimum data rates based on tile size.

4.2 The Digital Finite State Machine

The Finite State Machine (FSM) of the digital ASIC outlines the designed behavior response to input. Figure 4.2 shows a representation of the different states as well as the conditions to enter or leave each state.

There are two different kinds of prompts that an ASIC can receive: packet transactions from neighbors and resets from pixels. When an ASIC receives a packet from a neighbor, the packet data are written on the remote FIFO There is one special packet

- Idle, Acquisition State
- Transmit Local
- Transmit Finish

- Transmit Remote
- DONE

Idle

Transmit Data

Transmit Remote

4.3 The Parameter Space of the Digital System

The digital back-end design

Buffer Depth Requirements

The required buffer depth of each node in an array is the maximum number of timestamps the node can store in memory before overflow (dataloss). Each node requires some buffer memory to record local data as well as separate storage for remote data. The remote data which can be sent can come from any of the adjacent connected nodes, and may of any type: data words, register request, etc. Since the remote

The ice40 FPGAs have a total of 20 Embedded Block Ram models (EBRs) which allow for a total of 64xTODO memory depths allocated in each node.

Endeavor Packet Stability at Different Scales

We test two differet scales for the endeavor protocol. This protocol maintains a relative relationship between the number of high signals used to send either a high and low bit. The convention to send a high bit is to pulse a logic high signal for twice as long as is done for a low bit.

The number of bits used for to send a high bit are either

| Name | Function | Value Range |
|------|--|-------------|
| Zero | Controls how many clocks to send a logic high to transfer a low bit | 1–3 |
| One | Controls how many clocks to send a logic high to transfer a high bit | 2–5 |

Table 4.4: The address values are not sequential because some registers have become deprecated through development.

The Push and Pull Architectures

4.4 The Digital Back-end problem

The main objectives of the digital back-end are to correctly measure the data presented to it by the analog front-end and ensure lossless transport of that data to disk. More simply, the goals of the digital portion of the Q-Pix readout are to record and send data. We note that the successful completion of these two objectives to be goal of these simulation studies.

The Basic Datum

We begin with a discussion of the basic datum and mention initial design choices at the physical connection interface. The structure of this datum determines the buffer widths and depths required to store the data at the local ASIC level as well as the protocol used to transfer this data between ASICs and eventually out of the detector.

The minimum data which needs to be recorded are the timestamp, the relative location of the digitizing ASIC within the detector, plus any channels which were responsible for this reset. Each of the number of bits assigned to recording these parameters are a design consideration. We choose the number of bits for the timestamp (N_T) to be 32, which prevents frequency wrap-around based on a fast clock frequency (Equation ??). We choose as the number of bits to assign a location (N_{loc}) to be 8, which provides a maximum possible number of unique positions before aggregation to be 256. Next, since the number of pixels (required by analog front-end design) is 16 we choose this number as the number of bits to represent a “mask” ($N_{bits} = 16$). We need to record all of the channels during each reset since it is technically possible (even if less likely) for multiple analog channels to provide a reset within the same clock window.

We calculate the minimum number of bits per datum to be:

$$N_{bits} = N_T + N_{pix} + N_{loc} = 32 + 16 + 8 = 56 \quad (4.1)$$

Since buffer memory addresses and widths are normally characterized by powers of two, we can construct the basic datum size above the minimum number of bits provided by 4.4 to get $N_{\text{datum}} = 64$. The remaining bits are useful for constructing different types of packets to be used by the digital ASICs for additional uses such as register configuration or to provide packet identification.

Communication of the Datum

There exist many asynchronous protocols of communication of digital information. Most of the differences between protocols exist based on the number of connections between devices and whether or not one pin is allocated to share a clock, etc.

Our design considerations for this readout include reduction of SPF risk, low power, and minimal routing. Partly for these reasons, the design choice for communication relies on only two connections between ASICs. One connection is defined as a data receiver (Rx) and the other as a data transmitter (Tx). This choice of interface dramatically limits a choice of possible protocols. Here, we describe the difference between two that we tested: Universal Asynchronous Receiver-Transmitter (UART) and Endeavor. We discuss and test only these two protocols for simplicity, and find it instructive to compare a proven and custom protocol (Endeavor) with a very common one (UART).

The importance of choosing a correct protocol is to ensure lossless data transmission. Since there are free running clocks, an asynchronous communication protocol is required. The way to ensure that data can be moved between clocks of different speeds is to stretch the signal or to repeat bits. The more the word is stretched in time, the larger the allowable difference in frequency between the two devices. However, this lengthening can't proceed forever, obviously, otherwise data transmission time could exceed data capture rates.

It is another important design consideration, then, to ensure that transactions proceed as quickly as possibly without data loss. Additional concerns of long data transactions include the use of more clock cycles which use more power and increase the risk noise to leak to the analog front-end.

Endeavor

This protocol is slower than UART, but allows for approximately double the frequency difference: $\approx 20\%$.

The endeavor protocol relies on repeating the value of a high-bit, (digital '1' value) for an integer number of clock cycles. The receiver continually samples in incoming data transmission and counts the number of clock cycles that the signal was high for. The longer the signal was high, the more likely it is the the transmitter was attempting to encode a high bit, and vice versa.

The number of clock cycles which accompany either a high bit transmission or a low bit transmission then represent a possible design choice for the protocol. The actual number of bits which should be used ultimately depend on the similarity of the frequency between adjacent digital channels; the more similar the frequency (and relative phase) the lower these numbers can be.

- Start Bit
- High Bit
- Low Bit Send
- Stop Bit Send

4.5 Constraining the digital back-end Design

Section 2.2 describes in detail how a Q-Pix based hardware readout architecture could fit within a single DUNE-APA. Here we extend this discussion and use those constraints as the starting point for a search for a solution to the digital back-end architecture. The first problem to solve is how to aggregate the all timestamp data supplied by the large number of channels within a DUNE-FD APA.

A Q-Pix architecture would likely use either a high-performance FPGA or a custom ASIC to aggregate the large number of ($O(10^7)$) channels. The number of aggregated digital channels determines the required capabilities of the aggregator node and the selection of an FPGA or ASIC. Since each additional aggregator node represents an additional SPF risk, our design goal suggests that the optimal configuration is one that produces the least number of aggregator nodes. Therefore, the goal is to design a routing architecture which is responsible for as many digital channels as possible for each data aggregator node which still allows for accurate timing calibration and lossless data acquisition.

However, as one increases the number of digital channels per aggregator node one also increases the amount of local oscillators per aggregator, each of which must be calibrated. Additionally, since each digital channel requires extra communication time (as discussed in section 4.4) the introduction of more channels negatively affects the precision of timing calibrations and potentially increases SPF risk of digital channels. We consider then that an optimal number of digital channels per aggregator node is one that maximizes the number of digital channels but still maintains the required timing calibration (Sec. ??) and transmits lossless data.

We refer to the total number of digital channels collected from one pathway to an aggregator as a tile. In a fully realized design an aggregator might in fact be responsible for multiple tiles, which need not necessarily be the same size. The requirements of an aggregator node is completely determined by the composition of tiles it is connected to. Then, a parameterization of the data requirements imposed by each tile can be extended to describe the requirements of the aggregator node. Finally, we reach the conclusion that the required parameterization of the back-end system relies on the parameterization of the tile.

A tile is composed of inter-connections between digital channels. The LArTPC design suggests that each digital channel have a maximum of four connections since the collection of charge happens on a flat two-dimensional anode plane. Therefore, a two-dimensional routing requires at least two independent communication channels, which if we require the digital channels to allow bi-directional communication, the minimum number of channels is four. We use this number as a starting point for the digital channel design. These four connections per channel immediately creates a rectangular connection structure for a tile.

We note here that in order to meet other physical design requirements to fit into a pre-existing APA frame, the capability of the aggregator nodes could be increased to be responsible for more tiles, which would reduce the cable and hardware engineering considerations. However, further consideration here is beyond the scope of this work.

Tile Routing Considerations

A tile is a rectangular composition of digital channels which must provide a path to all digital channels and send lossless data to the aggregator. Since there is one connection between a tile and the aggregator, there is one special node within the tile that connects to the aggregator. This special node we refer to as the “base-node” as all data and instruction commands, regardless of routing, must pass through this node. The symmetry of the rectangular tile allows any corner node to be the base node, and we choose the upper-left to define a convention. An example of a tile with a Corner

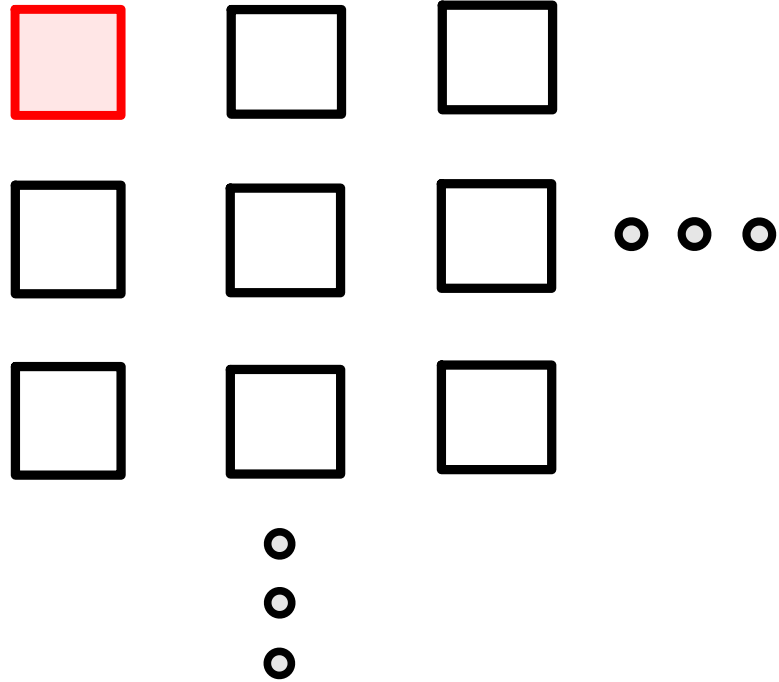


Figure 4.4: Example of an Corner Base-Node configuration. The base-node is colored and highlighted in red.

base-node is shown in Figure. 4.5.

We do not consider possible configurations where an aggregator might be connected to a digital channel within a tile since we require that all digital channels are identical and fully connected. We require identical channels as a practical choice due the required number of total channels. We also require the tile to be fully connected to allow as many possible unique paths between the base-node and the other nodes which provides maximum protection against SPF. We address that we discuss why we do not consider base-nodes placed on the outer edge of a tile, but not at the corners more generally in section 4.5. Briefly, base-nodes which are along the outer edge of a FCT but not at the corners simply contain two sub-graphs of FCT with a base-node along the edge. Therefore, an analysis of the constraints of a FCT with corner base-nodes can be mapped to an analysis of FCT with edge base-nodes.

Here we introduce a particular representation (based on graph-theory) for a tile which is useful for simplifying simulations and for analyzing particular routing configurations. The most general

tile configuration occurs when we assume that all adjacent nodes within the tile are connected; this creates what we refer to as a “fully connected tile” (FCT). An example of a FCT is shown in Figure ???. Any particular choice of an effective routing must then be a subset of this fully connected version.

To elaborate on the adjacency matrix of the FCT we consider an 2×3 tile. A 2×3 tile has six total nodes, where we consider the upper-left most node to be the base node. Then, the unweighted adjacency matrix has dimensions 6×6 of the form:

$$M = \begin{pmatrix} 0 & 1 & 0 & 1 & 0 & 0 \\ 1 & 0 & 1 & 0 & 1 & 0 \\ 0 & 1 & 0 & 0 & 0 & 1 \\ 1 & 0 & 0 & 0 & 1 & 0 \\ 0 & 1 & 0 & 1 & 0 & 1 \\ 0 & 0 & 1 & 0 & 1 & 0 \end{pmatrix} \quad (4.2)$$

Where each non-zero value of M_{ij} represents a connection between nodes i and j . As an unweighted, undirected graph this is a symmetric matrix.

In practice each digital channel within a tile is actually controlled by a unique, free-running oscillator. Therefore, we can define the length of each edge between nodes as the length of time to send of a packet of data between two nodes ($T_{i \rightarrow j}$). With this we can extend the model the adjacency matrix as a weighted and directed graph if we recognize that the non-zero elements of M_{ij} become $T_{i \rightarrow j}$, or the length of time it takes for the i^{th} local oscillator to transmit a packet to node j .

We can generalize this matrix in terms of an arbitrary number of rows (r) and columns (c). We define a convention of numbering nodes within the tile in terms of increasing column number followed by increasing row number. With this convention we obtain the general adjacency matrix with values defined by:

$$M_{ij} = T_{i \rightarrow j} (\delta_{i,j=i \pm 1} + \delta_{i,j=i \pm r}) \quad (4.3)$$

An adjacency list can similarly be constructed from Equation 4.5 where the non-zero connections are given by the kroniker-deltas factors.

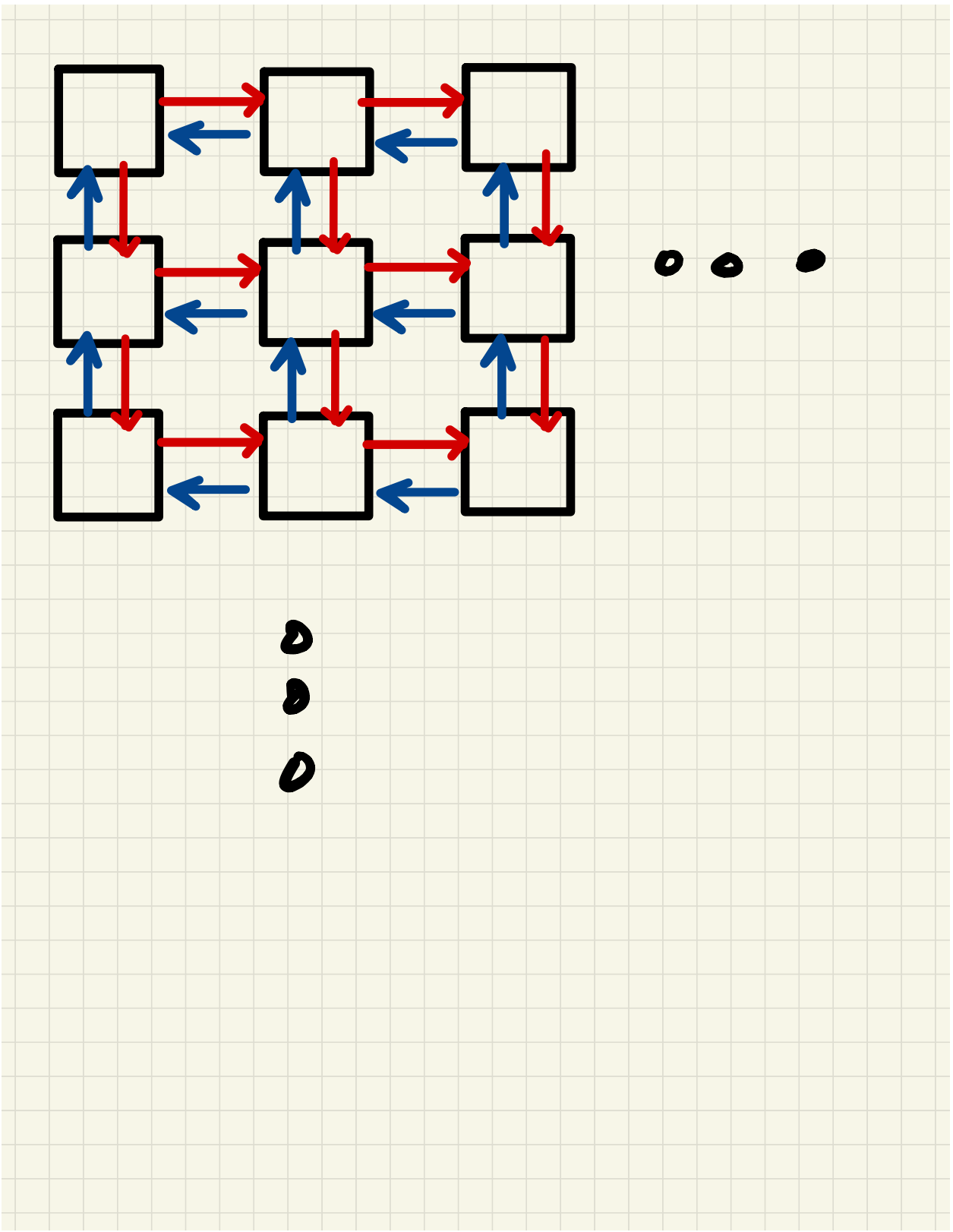


Figure 4.5: Example of the fully connected routing configuration for a tile (FCT). Each Node represents a digital channel which must be aggregated, and the red and blue connections distinguish directions of communication. The red connection lines indicate pathways away from the base node, whereas the blue lines represent connection paths towards the upper-left.

The length between the nodes represents the time it takes for a packet to transact from one node to the next. This is determined by both the number of clocks to be sent in the communication protocol (N_{bits}) and the period of the transmitting and receiving oscillators, T_i and T_j , respectively. Unlike the transmitter, the receiver only affects the transaction time with a single clock cycle, as the protocols we test here, (UART and Endeavor), each conclude a packet transaction when the receiver records the last bit transaction from the transmitter.

The full length between two nodes, i and j , connected by an edge is represented by:

$$T_{i \rightarrow j} = N_{bits} T_i + T_j(t) \quad (4.4)$$

where $T_j(t)$ represents the time dependent fractional part of one nominal clock period of the receiving node. The expectation value of $T_j(t)$ is half of the nominal window so that mean Equation 4.5 is:

$$\bar{T}_{i \rightarrow j} \simeq N_{bits} T_i + \frac{T_j}{2} \quad (4.5)$$

Since the transaction time of a packet is much larger than a single clock cycle ($N_{bits} \simeq \mathcal{O}(10^2) \gg \frac{1}{2}$), we can approximate Equation 4.5:

$$\bar{T}_{i \rightarrow j} \approx N_{bits} T_i \quad (4.6)$$

This representation is also useful to model certain SPF where a node becomes inactive. Dead or inactive nodes are ones in which all of their connections are effectively disconnected. This is equivalent to setting their transaction lengths to zero: $T_{SPF} = 0$.

We comment that although it is possible to construct tiles where more than one node connects to the aggregator, we observe that this configuration simply produces two effective tiles. These distinct tiles then are the data paths which are unique to each base-node. In this graphical representation a packet of data can follow one, and only one path from the origin node to the base-node unless there was duplication of packets. We emphatically avoid designs which might depend on data duplication for redundancy; these two base-nodes are in unconnected graphs.

Additionally, it is possible to connect non-rectangular tiles, but these tiles are effectively a larger rectangular tile with disconnected nodes to produce the desired shape. Since every node is designed to be robust in the full version, it will be robust in the subset.

We can apply this same argument to base-nodes which do not lie at the corners of the rectangular tile. In the case where the base-node is selected along the edge Therefore, we conclude that the analysis of the tile with the above adjacency matrix and a selection of the base-node at the corner of a rectangular corner provides the basis problem to the tile configuration.

The SPF Cost

We define the average SPF cost as the amount of nodes that will be lost during a transaction as the number of digital channels at a height below the failed digital channel. For example, the number of nodes which are lost if a leaf-node fails is one since no other channels are between it and the data node. Likewise, the number of nodes which are lost in the event of a base-node failure is the total tile, N .

We can then calculate a mean cost SPF, C_{SPF} , :

$$C_{SPF} = \frac{1}{N} \sum_{node} \frac{n_i}{N} = \frac{1}{N^2} \sum_{node} n_i \quad (4.7)$$

Minimize Occupancy

One of the goals of a successful digital design is to ensure lossless data transfer. One point of failure on the digital side is an overabundance of data arriving at a single layer within the tree. This data loss occurs when data are sent to a node faster than the data leaves the node, and persists for long enough such that the buffers of the node overflow. This creates a horrible loss of data which can't be recovered.

A routing scheme which minimizes the overall occupancy in the tree depths is shown in Figure 4.5. We refer to the style of routing as "Snake"-routing (SR), because this is also the longest possible routing scheme for a square tile.

We inspect the SPF risk from this routing scheme with Equation 4.5, where we notice that the n_i of each node is simply a running sum from the leaf to N at the base node.

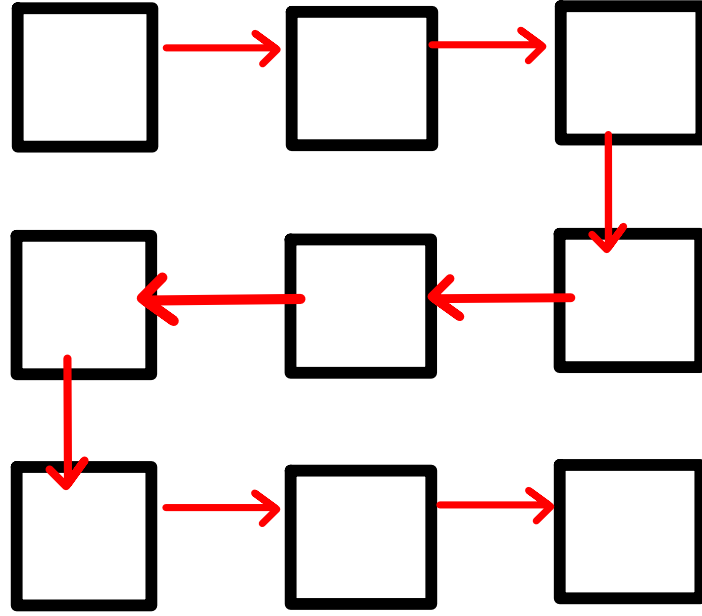


Figure 4.6: Minimal Occupancy Path of a FCT. This routing path ensures that the number of input connections equal the number of output paths for the node.

$$C_{SPF} = \frac{1}{N^2} \frac{N(N+1)}{2} = \frac{1}{n} \frac{N+1}{2} = \frac{1}{2} + \frac{1}{2N} \quad (4.8)$$

Equation 4.5 tells us that the SPF risk of this routing configuration converges to half as the size of the tile grows. Intuitively, this makes sense, since it is equally likely to select a node close to the base-node as it is far away, which implies that the sum should converge to half the tile size for large N .

Although this routing scheme provides the most lax constraint on the required buffers at each digital channel, it provides the longest average path between the base node. The longer the transaction delay between the base-node and other nodes increases the reconstruction time uncertainty. Therefore, a natural alternative routing scheme is one that minimizes the communication scheme.

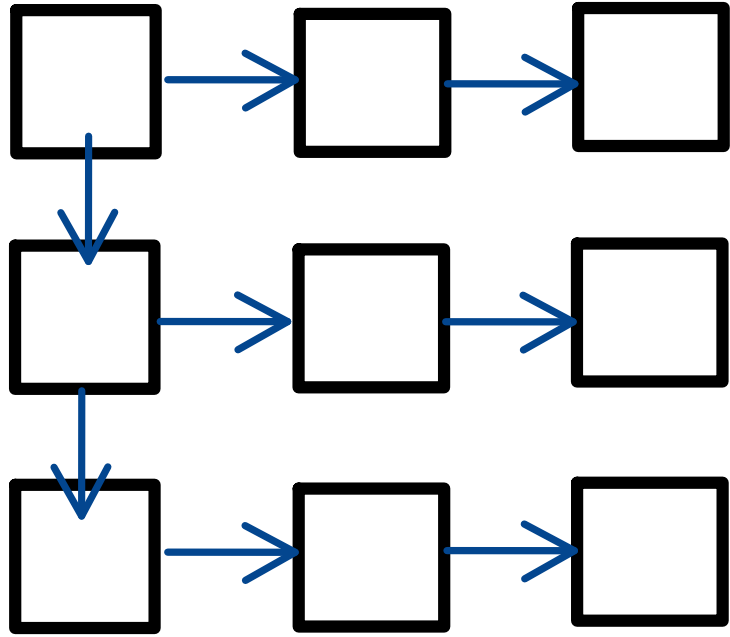


Figure 4.7: Minimal Delay Path of a FCT. This routing path ensures that the minimum number of transactions occur from every node in the FCT to reach the base-node. For any node along any column this is equivalent to the sum of the row and column of that node.

Minimize Delay

For any given node in an edge FCT with location (R_i, C_i) , the shortest path to the base-node is simply the sum of its coordinates: $R_i + C_i$. An example of such a routing configuration for a tile is shown in Figure 4.5.

We can calculate C_{SPF} for this routing configuration if we identify that there are a C number of rows which sum from one to $R - 1$. Likewise, the far-left column in Figure 4.5 shows that the number of rows, R , sum from one to C . We can rewrite the sum over all nodes in Equation 4.5 as:

$$\sum_{node} n_i = C \sum_{i=0}^{i=R-1} i + R \sum_{i=0}^{i=C} i \quad (4.9)$$

We simplify the running sum of each term in Equation 4.5:

$$\sum_{node} n_i = C \frac{R(R-1)}{2} + R \frac{C(C+1)}{2} = RC \left(\frac{R+C}{2} \right) \quad (4.10)$$

Using this result we obtain C_{SPF} by identifying $N = RC$:

$$C_{SPF} = \frac{1}{N^2} \sum_{node} n_i = \boxed{\frac{R+C}{2RC}} \quad (4.11)$$

This result informs that relative cost of losing a node tends to zero as the size of the tile grows. Again, this result can be obtained intuitively, since as the number of columns (or rows) grow in size, the probability of a single failure occurring on the aggregator column is increasingly less likely.

Broadcasts to avoid SPF

In order to protect against SPF we only consider designs which implement the FCT, since SPF can occur on any node the most robust connection scheme is the FCT. A FCT allows searches to probe all possible paths to any node via a “broadcast” produced from packets sent by the aggregator to the base-node. Therefore the broadcast algorithm can be represented by a complete circuit which begins at the base-node and proceeds to a target node with no repeated nodes until the target node is reached. The backward path is then completed in reverse by following the edges (connections) between each node until arriving finally again at the base-node.

In practice, we encode the broadcast packet with a special header, to differentiate it from a request packet. To differentiate broadcasts an identification number is also included in the packet. Then, any node which receives a broadcast packet will record the identification number of the most recent broadcast, which it uses to discard repeated broadcast packets that arrive with the same identification number.

In the event that a particular node becomes inactive it will “block” data coming from the nodes along its path. In this case, there must be some sort of “broadcast” originating from the base-node that would allow information to traverse regardless of the effective routing path.

$$\begin{pmatrix} 0 & 1 & 0 & 1 & 0 & 0 \\ 1 & 0 & 1 & 0 & 1 & 0 \\ 0 & 1 & 0 & 0 & 0 & 1 \\ 1 & 0 & 0 & 0 & 1 & 0 \\ 0 & 1 & 0 & 1 & 0 & 1 \\ 0 & 0 & 1 & 0 & 1 & 0 \end{pmatrix}$$

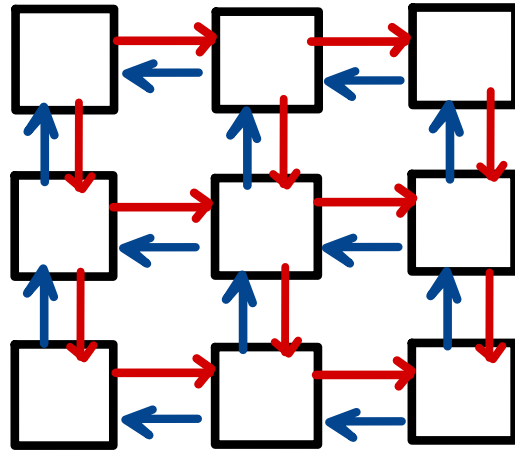


Figure 4.8: Minimal Routing Path of a FCT. This routing path ensures that the number of input connections equal the number of output paths for the node.

Comments on the Edge Base-node and Other Routings

We discuss here the case of a FCT with an edge base node. An edge base node (EBN) is a digital channel that connects to the aggregator and to three other digital channels within a tile. Like before, this base-node must provide a unique path during data transmission to all digital channels within the tile. In this configuration the adjacency matrix is still the same as given in Equation 4.5.

Also, as before, we wish to inspect different routing scenarios for a tile of a given square dimension of R rows and C columns. We can proceed by dividing the FCT graph into two subgraphs, $S1$ and $S2$, where $S1$ represents the rectangular section of the graph below and to the left of the EBN, while $S2$ are the remaining channels.

We identify that while the number of columns (C) in tile is equal to both subgraphs, the total number of rows R of the tile is equal to the sum of the rows from these two subgraphs: $R = R_1 + R_2$.

The EBN then is actually just a composition of two subgraphs which are each equivalent to The tree characteristics which determine requirements for the digital channels are the tree height and total occupancy at each level. Therefore, since the EBN provides no difference in either of these characteristics and is a superposition of two fundamental CBN, an analysis of an EBN is equivalent to the analysis of a CBN.

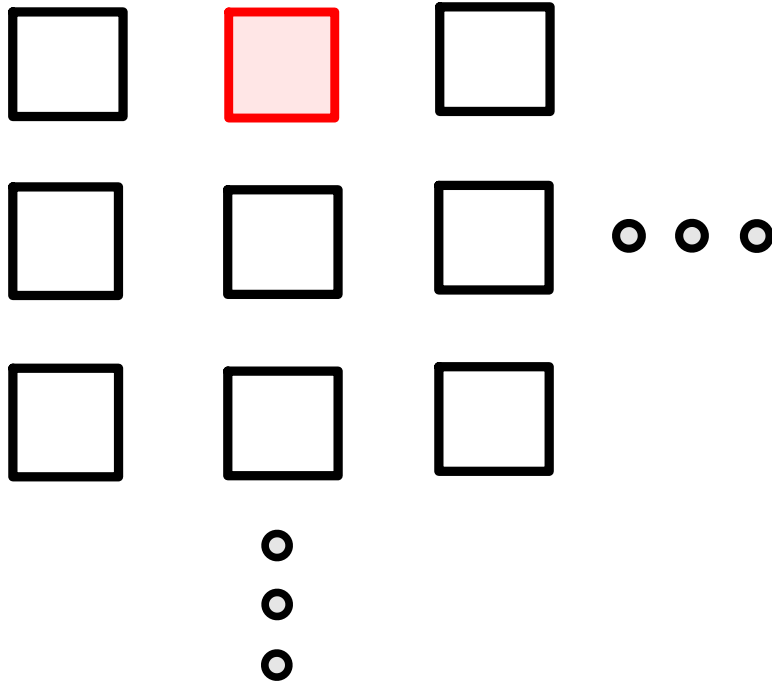


Figure 4.9: Example of an Edge base-node configuration. The base-node is colored and highlighted in red.

However, we do remark comment that the average difference of the relative weights of each node in a SPF analysis are different in a EBN compared to the CBN case. This should be obvious since the relative weight of each node is determined by the running sum of the path length between the base-node and its leaf. For a fixed row dimension, R , the EBN offers a smaller average tree height for each of its component radii R_1 and R_2 .

Therefore, in a EBN tile, with two subgraphs of radii R_1 and R_2 where the base-node is on the R_1 edge. The total sum of the weights of all nodes in the tile are the sums of the two subgraphs plus CR_2 , which is the average weight of the nodes from the subgraph R_2 when it connects to R_1 .

$$\sum_{node} n_i = \sum_{R_1} + \sum_{R_2} + CR_2 \quad (4.12)$$

Equation 4.5 gives the general formula for calculating the SPF risk for a EBN case, depending on the routing methods of subgraphs R_1 and R_2 . We can treat these sub-graphs as in equation 4.5 to

obtain:

$$\sum_{R_1} + \sum_{R_2} + CR_2 = \frac{R_1 C(R_1 + C)}{2} + \frac{R_2 C(R_2 + C)}{2} + CR_2 \quad (4.13)$$

We use this result to obtain the relation of the general C_{SPF} :

$$C_{SPF} = \frac{1}{N^2} \left(\frac{R_1 C(R_1 + C)}{2} + \frac{R_2 C(R_2 + C)}{2} + CR_2 \right) \quad (4.14)$$

if we identify that $N = C(R_1 + R_2)$ and use $R_2 = R - R_1$:

$$C_{SPF} = \frac{1}{2CR^2} (2R_1^2 - 2R_1R + R^2 + CR + 2(R - R_1)) \quad (4.15)$$

4.6 Frequency Calibration of Local Oscillators

The Q-Pix calibration requirements are described in detail in Section 2.1. The important parameters which must be calibrated for each pixel are the charge per reset and the frequency of the local oscillator. An aim of this work is to demonstrate an additional frequency calibration method using the minimal required connections between each digital node.

Any method of a frequency calibration must synchronize time measurements between all digital nodes within a tile and the aggregator. There are several possible methods to achieve this, but ultimately the data that are recorded must be some time at the aggregator, T_a , and the time at any specific node, T_j .

A direct method is one where the aggregator distributes its own clock to all nodes in the tile. This scenario removes the need for a calculation of the frequency of each node altogether since the clock of each node is already known from the aggregator. This is the simplest case for timing calibration: remove all free running oscillators. However, this method also introduces complex routing and power requirements within every tile.

A distributed clock network indeed removes ambiguity of the remote oscillator frequencies, but at the cost of hardware complexity. Whether or not this design choice is preferred is entirely detector dependent, but likely increases in difficulty with the scale of the TPC.

We comment, however, that we ignore this scenario because it may altogether be unnecessary depending on future ASIC performance. In the event that frequency calibrations of sufficient precision ($\bar{f} \approx 1 ppm$) are possible occur on free-running local oscillators future detectors would

need only to acquire these ASICs and place them with minimal cost in terms of both time and money.

Another simple scenario is one where the aggregator itself connects directly to all nodes within a tile via a single connection which can be used as a reference trigger. This means that some trigger from the aggregator would issue directly into each node at the same time: $T_a = T_n$. To calculate the frequency in this manner, the controller would issue two triggers from the aggregator with a known time separation, $T_o = T_{a2} - T_{a1}$. The remote nodes would each record and send their timestamps back to the aggregator, where the time difference would be calculated as:

$$T_o = T_{a2} - T_{a1} = T_{n2} - T_{n1} \quad (4.16)$$

this is rewritten in terms of frequency as follows:

$$f_n = \frac{T_{n2} - T_{n1}}{T_o} \quad (4.17)$$

This calibration method extremely simple but introduces an additional connection to each node between itself and the aggregator. For a large scale system such as Q-Pix even this simple connection scheme introduces $\approx 60 \times 10^3$ hardware points of failure per APA.

Both of these scenarios are valid implementations of a Q-Pix readout system. In both of these scenarios, however, there is added complexity into the hardware design of the system in the form of additional routing where each route which represents a possible point of failure.

In a world of perfect hardware and costless routing in terms of both time and money these routing schemes would clearly be sufficient. However, no hardware is perfect. Therefore we introduce and discuss a calibration technique which relies on no additional routing and could be optionally implemented even in the above schemes in the event of a failure. Therefore, even if not the primary implemented calibration technique, since this calibration introduces no superfluous routing it could still be used regardless of the actual future hardware implementation.

A Minimal Connection Calibration Procedure

As stated in the previous section, any frequency calibration records a reference time at the aggregator (T_a) and an event time (T_n) at a node within a tile.

the time calibration procedure presented here requires only the minimal routing required in any Q-Pix readout system, where we assume time-dependent free-running local oscillators at each node within the tile.

The calibration procedure begins at a time (T_0) where the aggregator sends a calibration packet.

Next, the packet propagates through the tile to some remote node, N_j . This node receives the packet later at some time T_{n1} :

$$T_{n1} = T_o + T_{f1} \quad (4.18)$$

Where T_{f1} is the propagation time of the packet from the aggregator to the N_j node.

This remote node then sends the packet with its time (T_{n1}) back to the aggregator.

The aggregator will wait some calibration time (T_{cal}) before issuing another calibration packet. This wait period ($\mathcal{O}(10^{0-2})$) can be long compared to the full transaction time to the N_j node ($\mathcal{O}(j * 10^{-5})$).

After the wait period, the aggregator will issue a second calibration packet to be sent to a remote node at time:

$$T_1 = T_{cal} + T_0 \quad (4.19)$$

Similarly to the first packet this packet will propagate to N_j with some new time T_{f2} where N_j will record time T_{n2} :

$$T_{n2} = T_1 + T_{f2} \quad (4.20)$$

Now, we define ΔT_j as the difference in the two time measurements from the two packets sent from the aggregator. The time difference is related to the number of clocks that occurred between the two different measured values of the clock, T_{n1} and T_{n2} .

$$\Delta T_j = T_{n2} - T_{n1} \quad (4.21)$$

We use the known relationships for T_{n2} and T_{n1} to obtain:

$$\Delta T_j = (T_1 + T_{f2}) - (T_o + T_{f1}) = (T_1 - T_0) + (T_{f2} - T_{f1}) = T_{cal} + \Delta T_f \quad (4.22)$$

Where we defined ΔT_f as the difference in forward propagation times from the packets sent from the aggregator node at T_1 and T_0 .

We arrive at the result which compares the measured time at the aggregator T_{cal} and the time measured at each node, ΔT_j :

$$\Delta T_j = T_{cal} + \Delta T_f \quad (4.23)$$

A perfect reconstruction of the nodal frequency would follow if $\Delta T_f = 0$. But it is sufficient to note that the wait period happens on the order of seconds, whereas ΔT_f is on the order of μs or at least a six order of magnitude difference. We then use $\Delta T_f \ll T_{cal}$ to obtain:

$$\Delta T_j \approx T_{cal} \quad (4.24)$$

We convert time into frequency with the difference of the timestamps measured and a known aggregator frequency (f_a):

$$\frac{\Delta N_j}{f_j} = \frac{\Delta N_a}{f_a} \quad (4.25)$$

or,

$$f_j = \frac{\Delta N_j}{\Delta N_a} f_a \quad (4.26)$$

Where ΔN_j and ΔN_a are the differences in the timestamps of the 32-bit clocks at the remote node and aggregator, respectively.

Packet Transaction Time

We next examine the approximation that $\Delta T_f \ll T_{cal}$ and consider its contribution to the error in the reconstruction of T_j . This analysis also provides a constraint on the duration of T_{cal} to ensure an accurate measurement of each T_j in a tile. We begin by discussing how long it takes for a packet to traverse a tile.

The time it takes for each packet to be received by the next node is given in Equation 4.5. The value, N_{bit} , is the number of clock cycles used for the packet and is protocol-dependent. Since the protocol must be deterministic for each packet, N_{bits} must be the same for each transaction on the path from the base-node to the remote node.

As an example, the time it takes for a packet to go from the base-node, N_1 , to a remote node, N_3 , via the path $1 \rightarrow 2 \rightarrow 3$ is determined by:

$$T_{1 \rightarrow 3} = T_{1 \rightarrow 2} + T_{2 \rightarrow 3} \approx \frac{N_{bits}}{f_1} + \frac{N_{bits}}{f_2} = N_{bits} \left(\frac{1}{f_1} + \frac{1}{f_2} \right) \quad (4.27)$$

Where, f_i , is the frequency of the clock at sending node. The approximation is within a single clock cycle of the receiving digital node (≈ 33 ns).

Therefore the time it takes for a packet to go from the base-node to any remote node is proportional to N_{bits} multiplied by the sum of the edges in the full adjacency matrix given by Equation 4.5.

We generalize Equation 4.6 to represent the time it takes a packet to go from the aggregator ($i = 0$) to any remote node, N_j :

$$T_f = T_{0 \rightarrow j} = N_{bits} \sum_{i=0}^{i=j-1} \frac{1}{f_i} \quad (4.28)$$

We require that every calibration packet on the protocol uses the same number of clocks (N_{bits} is constant) and follows the same path. ΔT_f becomes:

$$\Delta T_f = N_{bits} \sum_{i=0}^{i=j-1} \frac{1}{\Delta f_i} = N_{bits} \sum_{i=0}^{i=j-1} \Delta T_i \quad (4.29)$$

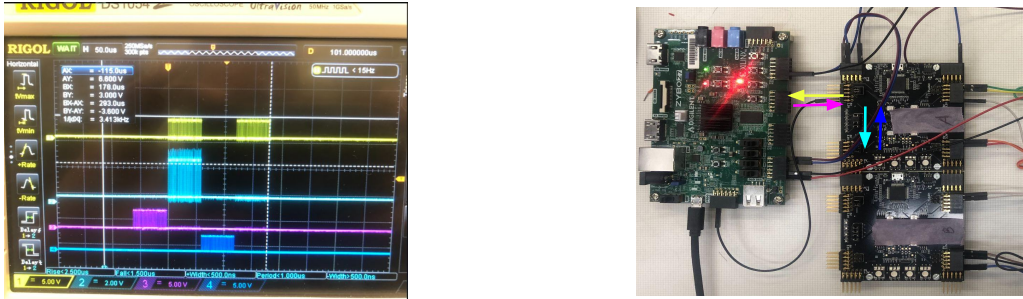
We recognize ΔT_i as the nominal time-dependent clock drift of each local oscillator in the path between the base-node to the remote-node. We can provide an order of magnitude estimate for ΔT_f if we assume a (very poor) $\approx 1\%$ drift in each of the remote clocks within the tile during a period of $T_{cal} \approx 1$ s. In this approximation we also assume that the mean of the periods of the nodes are the designed value (≈ 33 ns) for which a 1% error gives $\sigma_{T_f} \approx 3$ ps. If we assume that all of the clocks (for whatever reason) drift have error which drifts in the same direction (the sum doesn't cancel) then for 100 transactions with 1000 clocks per transaction, we obtain for ΔT_f :

$$\Delta T_f \approx 1000 * 100 * 3 \times 10^{-12} \approx 30 \text{ ns} \ll 1 \text{ s} \approx T_{cal} \quad (4.30)$$

4.7 The Digital Prototype Design

This section marks the second part of this chapter. We describe the design of a digital back-end prototype, which is configured as a 4×4 array of nodes. Each node is implemented with the logic described in the previous sections.

These nodes are used to test the control logic, communication stability, buffer requirements, and calibration methods. The most important quantity that must be calibrated for the digital nodes is the frequency of the local oscillator. The Q-Pix reconstruction for both time and z position are dependent on this parameter, see Chapter 2.



((a)) Waveforms caught on an oscilloscope. The((b)) Example of arrows depicting the direction of the timescale is 50 μ s.

Figure 4.10

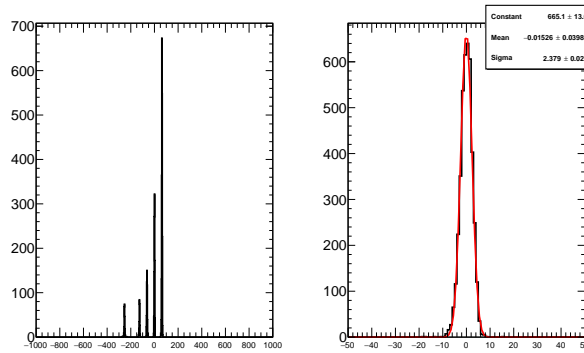


Figure 4.11: Example of frequency calibrations for the FPGA Adjacent to the Zybo.

Since the frequency is the most important quantity, we also dedicate a full section to describe the results of the of local oscillator tests.

Future implementations of the digital back-end for Q-Pix may, of course, use different oscillators. However, these results are still beneficial as a proof of concept for the frequency calibration, as well as tests to the packet loss susceptibility. Packet loss is a function of relative frequency drift between neighbor nodes.

Frequency Calibration of each Node

Charge Auto-Calibration of each Pixel

Natural decay products produced by ^{39}Ar provide a continous source of incoming current across a LArTPC.

| FPGA Position | Mean | STD | $\frac{\delta f}{f_o} * 1e6$ (ppm) |
|---------------|--------------|-------|------------------------------------|
| (0,0) | 30000245.543 | 2.379 | 0.079 |
| (0,1) | 30000190.646 | 2.979 | 0.099 |
| (0,2) | 30000153.908 | 3.334 | 0.111 |
| (0,3) | 30000248.831 | 3.843 | 0.128 |
| (1,0) | 30000192.729 | 2.860 | 0.095 |
| (1,1) | 30000210.905 | 3.405 | 0.114 |
| (1,2) | 30000116.212 | 3.984 | 0.133 |
| (1,3) | 30000159.824 | 4.158 | 0.139 |
| (2,0) | 30000351.431 | 3.685 | 0.123 |
| (2,1) | 30000193.845 | 4.285 | 0.143 |
| (2,2) | 30000200.278 | 4.071 | 0.136 |
| (2,3) | 30000152.633 | 4.263 | 0.142 |
| (3,0) | 30000183.359 | 3.954 | 0.132 |
| (3,1) | 30000209.788 | 4.561 | 0.152 |
| (3,2) | 30000192.277 | 4.169 | 0.139 |
| (3,3) | 30000171.302 | 4.538 | 0.151 |

Table 4.5: FPGA calibration results based on hard interrogations at a frequency of 4 Hz.

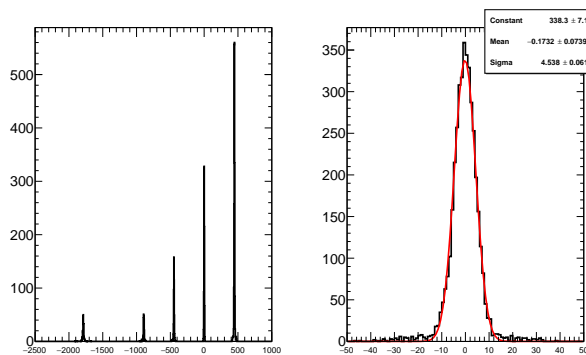


Figure 4.12

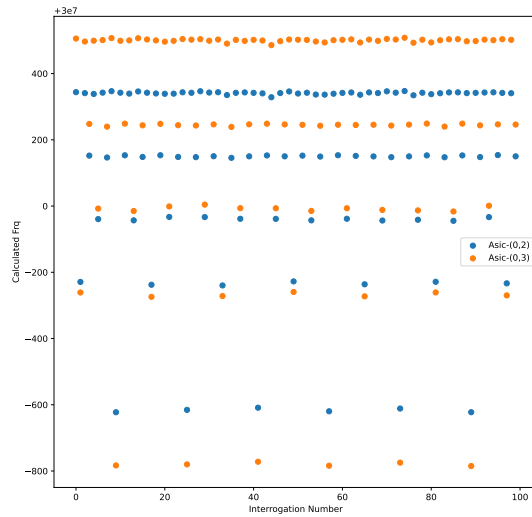


Figure 4.13

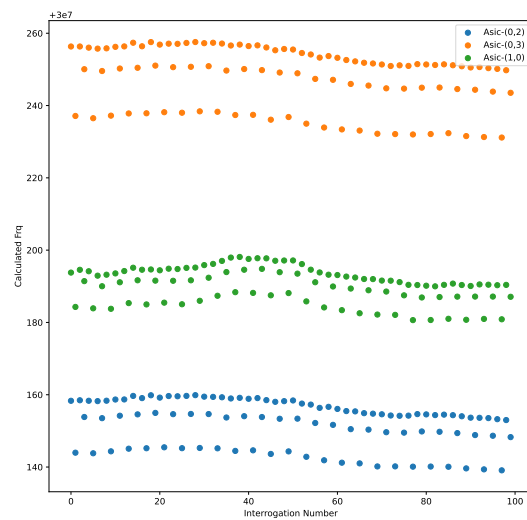


Figure 4.14

| FPGA Position | Mean | STD | $\frac{\delta f}{f_o} * 1e6$ (ppm) |
|---------------|--------------|-------|------------------------------------|
| (0,0) | 30000245.543 | 2.379 | 0.079 |
| (0,1) | 30000190.646 | 2.979 | 0.099 |
| (0,2) | 30000153.908 | 3.334 | 0.111 |
| (0,3) | 30000248.831 | 3.843 | 0.128 |
| (1,0) | 30000192.729 | 2.860 | 0.095 |
| (1,1) | 30000210.905 | 3.405 | 0.114 |
| (1,2) | 30000116.212 | 3.984 | 0.133 |
| (1,3) | 30000159.824 | 4.158 | 0.139 |
| (2,0) | 30000351.431 | 3.685 | 0.123 |
| (2,1) | 30000193.845 | 4.285 | 0.143 |
| (2,2) | 30000200.278 | 4.071 | 0.136 |
| (2,3) | 30000152.633 | 4.263 | 0.142 |
| (3,0) | 30000183.359 | 3.954 | 0.132 |
| (3,1) | 30000209.788 | 4.561 | 0.152 |
| (3,2) | 30000192.277 | 4.169 | 0.139 |
| (3,3) | 30000171.302 | 4.538 | 0.151 |

Table 4.6: FPGA calibration results based on hard interrogations at a frequency of 0.1 Hz.

4.8 Timing Stability

We describe here the methods of measuring a stable time for different configurations of the nodes. We also comment on the results of the timing with respect to the minimum required timing sensitivity in order to have accurate timestamp reconstruction.

4.9 Power and Current Characteristics

There are test pads on the PCBs used to measure the voltage stability of the different FPGA voltages. For each voltage, there is also a single $1\ \Omega$ probe-resistor. This resistor is used to measure the relative current drawn from each of the voltage sections on the PCB.

4.10 Analysis of Systematics for Different System Implementations

The essential features of the digital node in the Q-Pix readout are the properties of the local oscillator. The frequency, relative phases, and stability of the oscillator determine the power consumption, packet transaction time, minimum timestamp resolution, which determines maximum current measurements, and affects packet loss probability in larger tile systems. It is not an understatement to say that the successful development of the digital node relies on the development of the local oscillator.

4.11 Towards the Integration of the Aggregator Node

In the studies presented here, The aggregator node which was used was the Zybo Z7-20.

4.12 Comments on A Super-DAQ-Node

Each APA module within a larger DUNE module must ultimately be interconnected so that the entire module can be readout. As described above, a single modular tile is controlled by an individual DAQ node, where many constitute a complete APA. Therefore, we refer to the device that digitally multiplexes all of the DAQ node data as the "Super DAQ Node" (SDN). Then, we imagine the final multiplexing stage for an entire DUNE module as an array of SDNs, each of which consistute an array of DAQ nodes, where each DAQ node is a 2-D array of Q-Pix based ASICs.

The total number of request SDNs within the full dune module depends on the final size of a DAQ-node controlled tile.

4.13 The Back-End Summary

THE Q-PIX BACK-END AND SIMULATION STUDIES FOR FUTURE Q-PIX PROTOTYPES

This chapter explores the requirements of a Q-Pix based digital back-end readout targeted at a DUNE-FD module.

The first part of this chapter describes the digital simulation used to evaluate the possible designs presented in the previous chapter. The Q-Pix readout (Chapter 2) relies on several key factors which promise possible improvements over a traditional MWPC readout: automatic calibration from quiescent radiogenic background, an overall reduction in volume of data collection, and simpler analysis chain and vertex reconstruction, to name a few. However, this novel readout technique not only changes the front-end analog structure but also dramatically increases the number of digitization channels. The increase of the number digital channels and required ASICs creates the need for a new digital back-end design.

The second part of this chapter presents results from a physical simulation framework based on radiogenic backgrounds in LArTPCs as well as high energy ($\approx 10\text{GeV}$) neutrino events. We use this physical simulation framework to address a number of design choices, since any sufficiently complicated design offers an intractible number of possible choices each of which can significantly alters the performance of a detector. A few examples of crucial design choices for the digital back-end are: the use of free-running local oscillators, the selection of an inter-ASIC communication protocol, the choice of inter-ASIC connections or routing profiles, and the buffer sizes of FIFOs to store charge-reset data. The goal of the simulation is to parameterize these design choices in order to provide an understanding of functional design targets and analysis of design tradeoffs.

The final part of this chapter synthesizes the results of the physical and digital simulations and provides a description of the effects of the most important parameters determined from these results. We use as inputs to the simulation the expected input charge from radiogenic background and beamline neutrino interaction over a $2.3\text{m} \times 6.0\text{m}$ LArTPC. The characterization of the analog front-end, namely the charge characteristics per channel, is an on-going collaborative work whose results can be able to be applied here.

All results in this chapter are my own individual work.

5.1 The Tile Simulation Framework

The previous chapter introduced the digital back-end as well as discussed different design choices, namely tile size, routing configurations, and the effects of the aggregator position. Here we describe how we simulate events of interest for these different configurations.

A successful design is able to record and send loss less data for all events of interest. In a DUNE-FD LArTPC these sources range in intensity from sub-MeV-scale radiogenic backgrounds native to the LAr to 10's of GeV scale of beam neutrinos or atmospheric neutrinos. We consider the back-end design to be successful if and only if it provides the ability to fully capture and transmit of all collected resets from these sources.

We note that while it may be shown in the future that some resets may in fact not be needed for a reconstruction of particular events, we still assert that since Q-Pix is a novel readout, it is not yet possible to claim all scientific goals for which it may be used. For this reason we demand that no data be lost for any reason due to the digital back-end design.

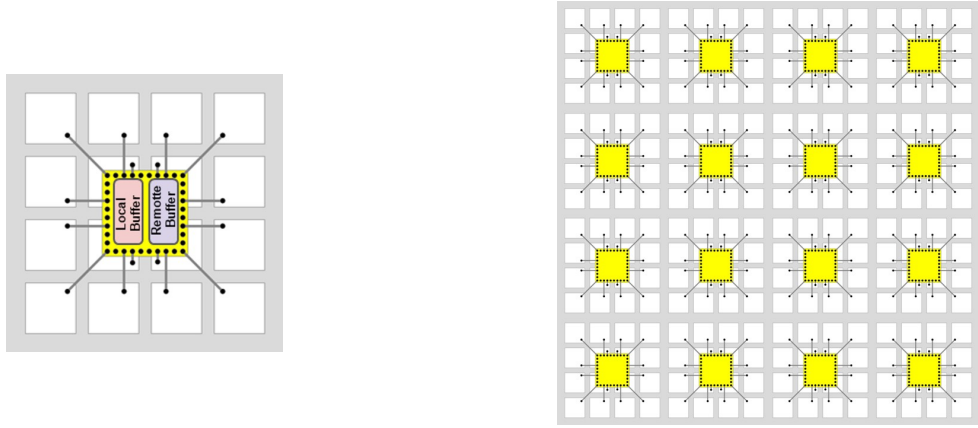
The Tile Representation

We model a tile (a group of digital nodes, or ASICs) based on the description given in Chapter 4. A tile is then represented in software (Python 3) as a linked list of nodes which store pointers to the adjacent nodes or neighbors.

We note a distinction between the nomenclature used here. The term "node" refers to the simulated back-end ASIC whereas our use of "ASIC" refers to the first digital prototype.

Every node in the tile holds two FIFO objects which store local and remote data. The local and remote FIFOs keep track of the total number of resets or packet transactions, respectively. If a node records a new reset the local FIFO is then written to, and the local FIFO transaction counter increases. Similarly, the remote FIFO's transaction count is increased when a write occurs on this FIFO, which happens every time a digital node receives a packet from a neighbor node, including the aggregator node.

In the current Q-Pix digital ASIC design (see Sect. 4.2) all packets sent between neighbor nodes, with the exception of broadcasts, are written on the remote FIFO. At the beginning of a simulation step each node first checks to see if it has received an interrogation request. If the node has received a soft interrogation request (see Sect. 4.5), and has data in its local FIFO, it will first send its data in the local FIFO, followed by the event-end packet. If the node receives a hard interrogation request, the node will send local data, if any, and will send an event-end packet regardless of whether or



((a)) Individual node with local and remote FIFOs.

((b)) Tile of node objects.

Figure 5.1: Composition of an example 4×4 tile. Each node in the tile represents a digital ASIC which contains two FIFOs. One FIFO is used to store timestamps from reset data, which we refer to as the local FIFO. The other FIFO we call the remote FIFO and is used to store all packet transactions from neighbor nodes. The local FIFO is 48 bits wide, where 32 bits come from the timestamp and 16 bits are from the pixels. The remote FIFO is 60 bits wide, since it must store all relevant bits for the 64 bit packet word, where there are 4 unused bits.

not the local FIFO had any data. If the node's local FIFO is empty, and it has not received an interrogation, it will check the empty status of the remote FIFO. If the remote FIFO is not empty, this packet will be read and transmitted to its neighbors accordingly, otherwise the node remains in its idle state [4.2](#).

There are two types of remote data to send: broadcasts and responses. A broadcast is a register request sent to a digital node, which can only be created and sent from the aggregator node. The responses include all other kinds of packets sent from neighbor nodes which include: data packets, event-end packets, and register response packets.

The communication packet object is a custom struct object which uses an enumerated type to differentiate the kinds of packets that the digital node can read from its remote FIFO. Each simulated node's behavior to these incoming packets is mirrored to the digital FSM, shown in Fig. [4.2](#). When a node reads the packet from the remote FIFO it reads the enumerated type to determine how to communicate the packet to its neighbors, just as is done in the physical ASIC.

Also tested in these simulations are tiles which have a "push" architecture. This architecture changes the condition for a node to leave its idle state and send local data whenever the local FIFO is

not empty. For this reason the push architecture is also more time consuming to simulate since each node can send a packet at any time, provided that it will inject a hit into its local FIFO following the procedure described in the next section. Nodes which require an interrogation in order to send local data we refer to as the "pull" architecture.

Injected Resets

In order to speed up the execution of the python simulation reset events are precalculated and loaded into separate list containers for each node. At the beginning of every simulation time step every node checks its injected resets list against the new simulation step time. If the new time step is larger than any of the timestamps in its resets list, the resets are then removed from this list and are written to the node's local FIFO.

Resets from simulated data whether radiogenic or neutrino data can occur at any pixel and at any time. The digital node (and the ASIC) is capable of recording multiple resets from multiple channels at the same time. This means that it is possible for multiple different pixel resets to only contribute to one local FIFO write. Therefore, extra care must be taken when adding injected resets with channel information.

In this simulation we consider the best case timestamp measurement for each reset, which is that each digital node can record a unique reset for each channel on every new clock cycle. Then, procedure for combining resets from multiple channels calculates the clock cycle (timestamp) for which this node would record a timestamp for a particular channel. If a reset has already been recorded for this channel, the uninjected timestamp is incremented by one clock period for this node. The above procedure then repeats until all channels have had all of their resets recorded on unique timestamps for the digital node, where only different channels can be recorded on the same timestamp.

The Simulation Procedure

Upcoming sections will discuss values derived from simulating the readout of the tile. Here we briefly describe the simulation procedure and how the results are obtained. The procedure is also graphically demonstrated in Figure 5.1.

Simulation Stepping Procedure

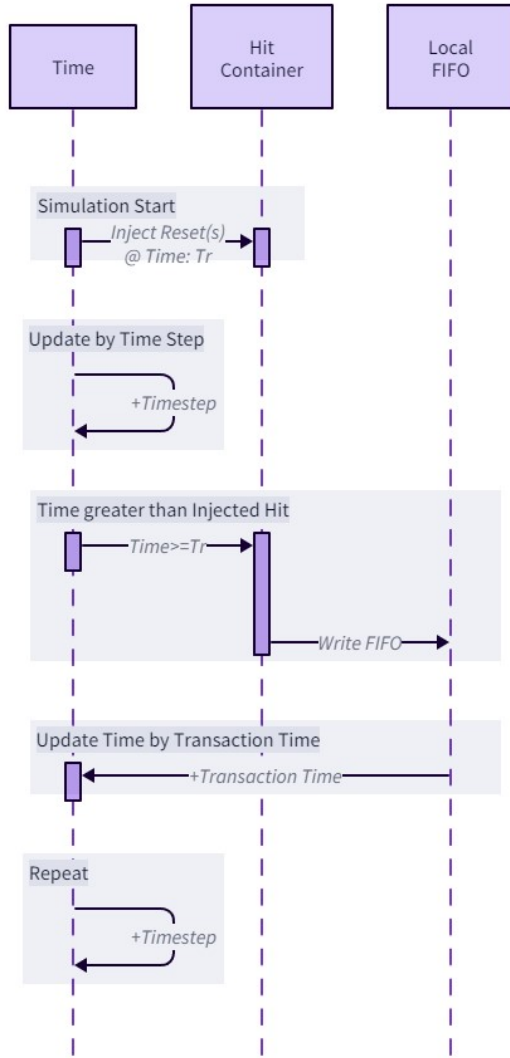


Figure 5.2: Example timeline for simulation time steps and injected hits. Before the simulation begins hits are added into a Hit Container for each node. When the simulation begins the time is incremented by a single time step ($\tau = 1\mu s$). The time increments until it is larger than the time of any of the injected hits. The values of the timestamps are then moved from the Hits container into the Local FIFO, where the timestamp that is recorded is the soonest clock cycle after the "true" time of the injected hit. When the data are ready to be transmitted from the Local FIFO, the time is then updated by transaction time. An example of this procedure is shown in Figure 5.3.

The simulation loop iteratively processes a single transaction from a queue of transactions and then processes all nodes in the tile at incremental timestamps. The timesteps used in the simulation results used here are steps $1\ \mu\text{s}$. It is not necessary to perform smaller time steps than this, as packet transactions themselves are on the order of $\approx 50\mu\text{s}$, based on the endeavor protocol. If any processed node generates a new transaction(s), this transaction(s) is added to the transaction queue.

A transaction represents a 64-bit packet that is transferred between two nodes (Sect. 4.1). The sending node is responsible for calculating the true time when this transaction would complete. The receiving node records this byte onto its remote FIFO and performs the state check based on this packet according to Fig 4.2. Then the receiving node updates its time to its soonest clock cycle after this transaction completed. Next, each node in the entire tile is processed one forward timestep. If nodes are in the push state and receive a hit within this timestep window, they create a new outgoing packet, and add this packet to the transaction queue. We note that it is only possible for processed nodes which did not receive the transaction packet to create a new packet if they are in a push-based architecture.

The simulation is complete when all nodes have been processed up to the final requested time and no transactions are left in the queue. In the results presented here we process the tile for one second longer than any injected resets to ensure that the tile is fully read out.

5.2 The Tile Parameters

One goal of the simulations presented here is to parameterize different design choices in constructing both the digital nodes and the tiles. The different parameters which we test are described in Table 5.2.

There are a total of four parameters to test: frequency stability, tile size, routing, and architecture. Of the four parameters, we note that the frequency stability is the one parameter determined by the ASIC's physical design. Therefore, special care must be taken into account when designing the local oscillator for the ASIC. The other variables: routing, architecture, and tile size are either programmable registers or easily configurable in hardware layout.

It is intuitive (and the results indicate) that improved frequency stability leads to a more stable design. Nevertheless, we find it enlightening to demonstrate how remote buffer depths are affected in the case of a 5% (0.5%) clock deviation. When a tile is created with 5% (0.5%) frequency deviation each node within the tile is created by randomly sampling from a gaussian distribution with a mean of 30MHz and a standard deviation of 5% (0.5%). Since many ($\approx 10^4$) events are

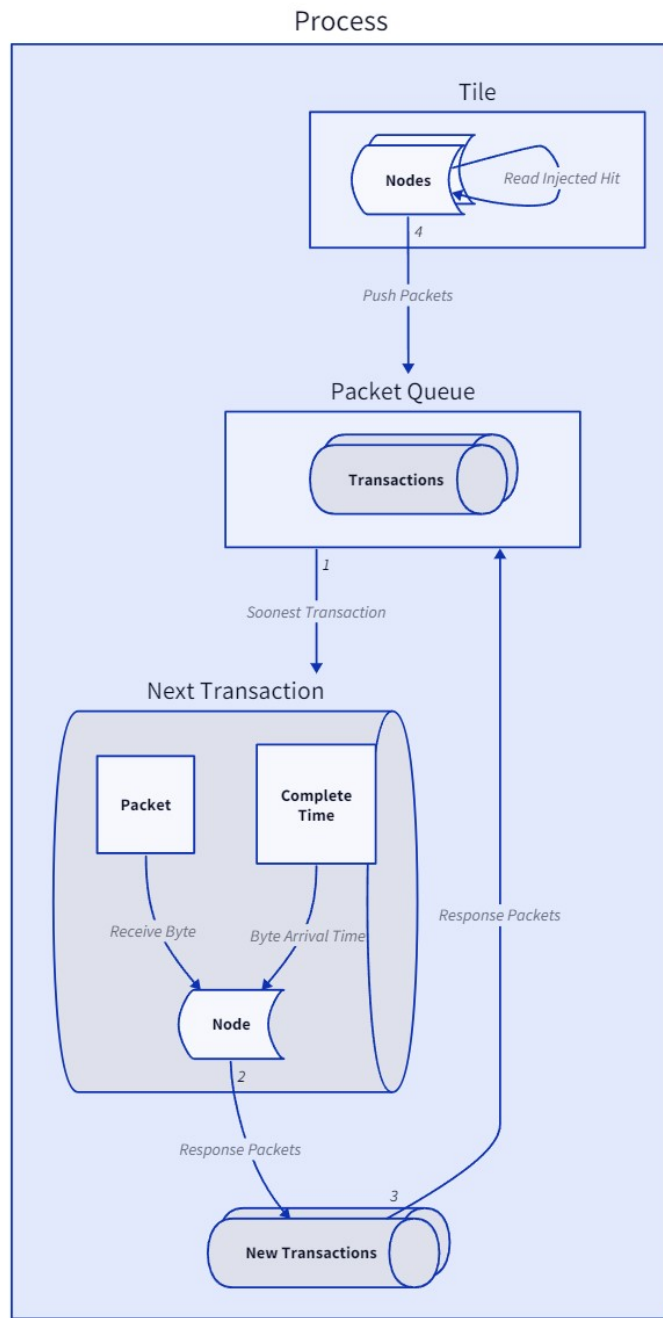


Figure 5.3: Flow chart of the simulation process method which occurs for every simulation time step. The simulation contains a queue of packet transactions. The queue is sorted by ascending time, so that the earliest transaction completed time is processed first. Each transaction contains a packet, a node, and the time the packet arrives. When the node receives the packet, it can optionally create more transactions, depending on the node's state and the packet. Any additional transactions are added to the simulation queue, and are time sorted. The simulation then increments the time for all other nodes within the tile. This procedure repeats until all nodes in the tile research designated time, which for the results presented here is 11 seconds.

| Name | Values | Relation |
|----------------------|--------------------------|---|
| Oscillator Frequency | 0.5%, 5% | High variance causes packet buildup or drift within the tile depending on whether packets are sent from slow to fast, or fast to slow clocks. |
| Tile Size | 4×4, 8×8 10×14, 16×16 | Affects total number of resets which must be routed to aggregator. |
| Routing | Snake, Left, and Trunk | Tiles with different routing are effectively different graphs which affect packet buildup (4.5). Different combinations of edges between nodes can cause packet buildup if nodes have more input edges than output edges. |
| Architecture | Push, Pull | Describes conditions for when node enters transmit-local state. 4.1. The push architecture allows individual nodes to transmit data when data are received, whereas pull architecture only send data upon receiving a special request packet from the aggregator. |

Table 5.1: The different tile parameters that are used for the effective tile search. The frequency drift relates the relative distribution of the frequency of adjacent oscillators. The tile size determines how many digital nodes are within a single tile. The routing configurations are described in detail in the previous chapter, and refer to how local data words are sent to the aggregator. The two different architectures define how the node enters the transmit local state. The push architecture enters whenever a new reset is acquired, whereas the pull architecture enters only when a data request is received from the aggregator.

performed per tile configuration each tile is created with a random seed to ensure that each node is created with the same frequency for each test.

The other design parameters are readily configurable in either hardware (tile size) or through register configurations of the digital node (routing and, possibly, architecture). Tile size is mostly an engineering and cost constraint. Larger tile sizes mean the full design would require less aggregator nodes and require less tiles to parameterize. We show results for varying tile sizes to indicate that increasing tile size may not necessarily linearly reduce cost, as larger tile sizes complicates the requirements on the digital nodes. For this reason, the largest tile size we tested was 16×16 .

The routing and architecture parameters help guide the digital design efforts design of the digital ASIC. In practice it is all but certain that implemented routing for a digital tile will take on a

combination of the routing styles described here. The reason for this is simply that is likely that some digital nodes will fail (for whatever reason) in the life time of a DUNE-FD 10 kT module. Therefore, future tiles that contain hybrid routing we suggest to those users to individually analyze the sub tiles with appropriating routing and frequency distribution and determine if the buffer depths are appropriate.

Oscillator Frequency and Drift

Two different oscillator frequencies are tested, as shown in Table 5.2. These different frequency variances indicate mean differences in oscillator frequency between adjacent nodes. An example of the 5% oscillator variance is shown in Figure 5.2. The values plotted in this figure indicate relative factors above or below the expected 30MHz mean.

Local oscillator drift was not included as a testing parameter since transactions occur over small time scales compared to any likely meaningful oscillator drift. If these drifts occur on time scales much longer than the interrogation time than the oscillator, the frequency could be continually re-calculated with the method shown in the previous chapter. If these drifts are periodic about a mean frequency and on time scales much smaller than the interrogation time window then the drifts would average out. In the event that clock drift timescales are on the interrogation timescale ($\approx 1\text{s}$), then this is equivalent to a frequency uncertainty for the entire transaction cycle. This would mean that an oscillator has a $\approx 5\%$ uncertainty in its frequency on each interrogation. Such a node would not be able to reconstruct timestamps, and therefore not be able to reconstruct the z-position of charge with the required 1ppm estimated uncertainty for Q-Pix clocks [6].

5.3 Simulating The Tile Readout

The tile simulation is performed by injecting hits from two known sources: radiogenic backgrounds and beam neutrinos. All results presented in this chapter are based on 11 seconds of simulated run time. Radiogenic data are collected and used to occupy 10 seconds of background noise resets. The higher intensity neutrino events are offset so that interaction occurs at $t = 5.1\text{s}$. The simulation is run for a total of 11 seconds, instead of 10, to ensure that all of the packets are collected by the aggregator node. In practice, there would be additional resets from backgrounds which occur in that final second of data. However, the number of resets from the radiogenic events are much smaller (by about two orders of magnitude) than the neutrino events.

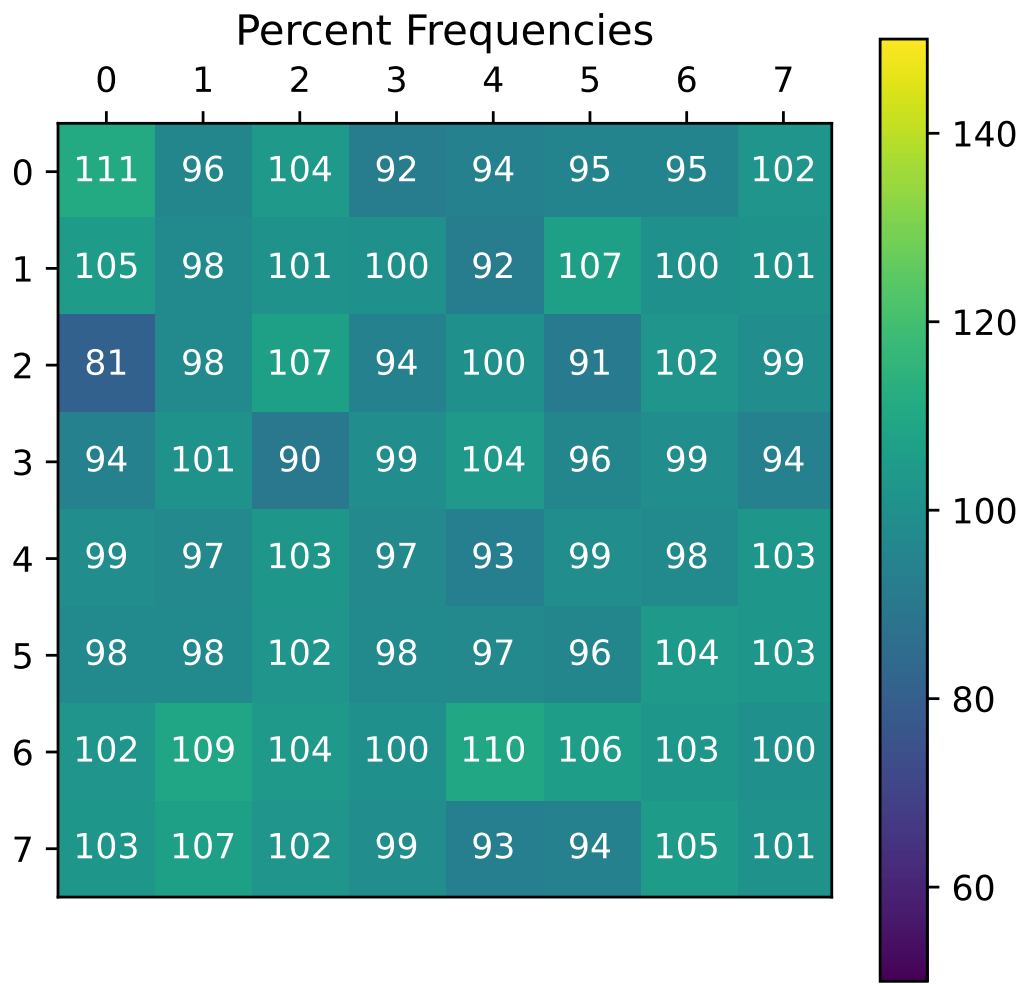


Figure 5.4: Distribution of ASIC frequencies used in the 8×8 tile, and in the example FIFO buffer depths for this chapter. The numbers plotted above each ASIC row and column indicate the relative frequency of this ASIC compared to the nominal 30MHz mean. For example, a number of 112 indicates an ASIC which is 12% faster than 30MHz, a frequency of $\approx 33.6MHz$.

The full readout of the tile occurs based on the number of packets times the average transaction length.

$$T_{readout} \approx 50\mu s \times N_{maxpackets}$$

If we set $T_{readout}$ to 1 second:

$$N_{maxpackets} \approx 20000$$

Since the simulation is run six seconds longer than the origin time of the neutrino events all reset events are accounted for if neutrino events cause less than ≈ 120000 resets. There are no simulated neutrino events which create these number of resets since this would require an energy of $\approx 15\text{GeV}$ deposited into the LAr.

The configuration of each node and the tile happens before the beginning of the simulation. The frequency and the routing directions are configured for each node during its creation.

Simulation Timing

The purpose of the simulation is to examine the communication behavior of digital nodes at different frequencies which communicate via packets of variable time width. For this reason special care is taken to ensure that the timing of packet transactions in the simulation are accurate. The behavior of each node is determined by its state machine properties, as described in Fig. 4.2. Therefore, an accurate measure of timing for each node is equivalent to ensuring that timing of ASIC state transitions are accurate.

Not shown are times when an ASIC receives or responds to a broadcast. Broadcast packets are uniquely handled by ASICs. An ASIC, instead of writing the request to the remote FIFO, immediately handles a broadcast by sending this packet to all neighbor ASICs, excluding the direction from which it received the broadcast. This means that an ASIC's state does not change during a broadcast. This is handled by the simulation by tracking packet times on the ASIC connections. The broadcast packet is sent starting at the soonest available time on each connection. The full broadcast procedure is described in Section 4.5.

Snake Timing Example

Here we refer to the "snake" routing as the maximal path routing. This routing is one that minimizes the number of input edges for all nodes within a tile. An example of a packet transfer which uses this routing is shown in Figure 5.3.

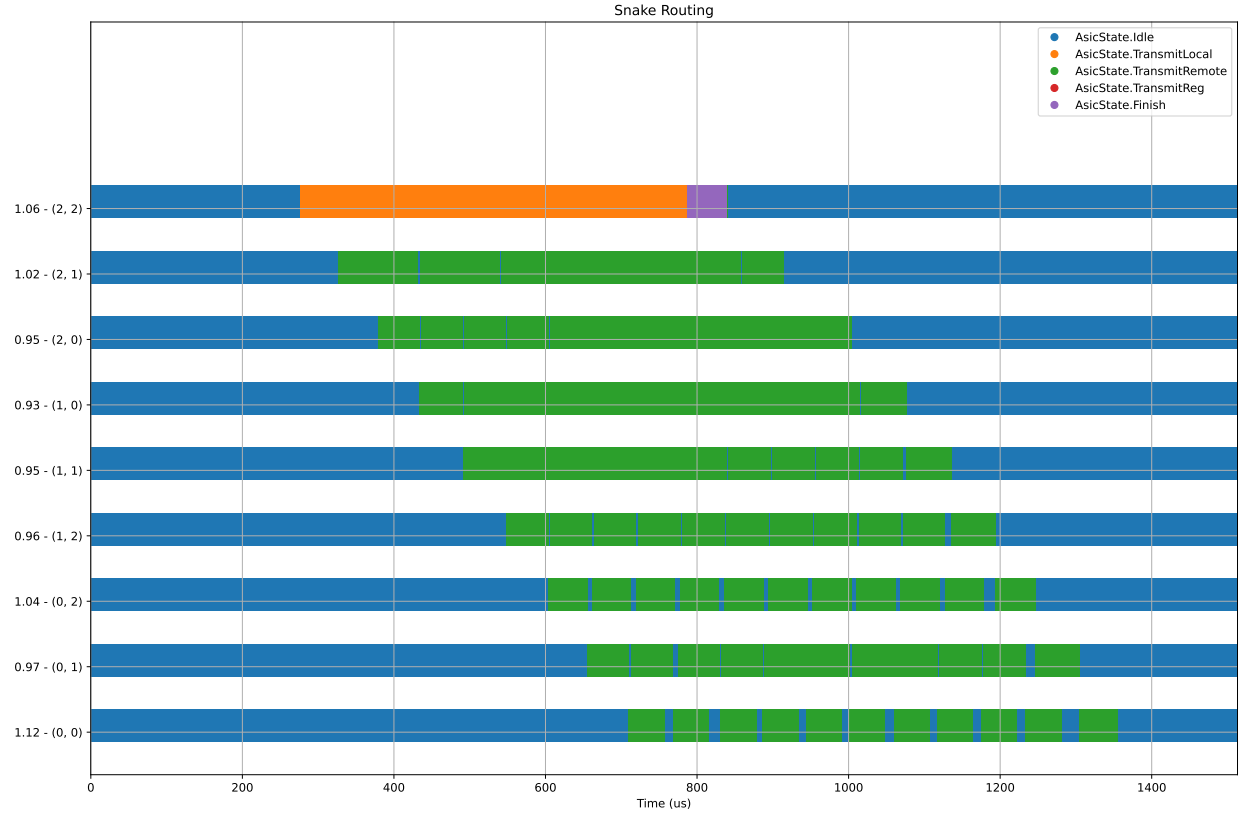
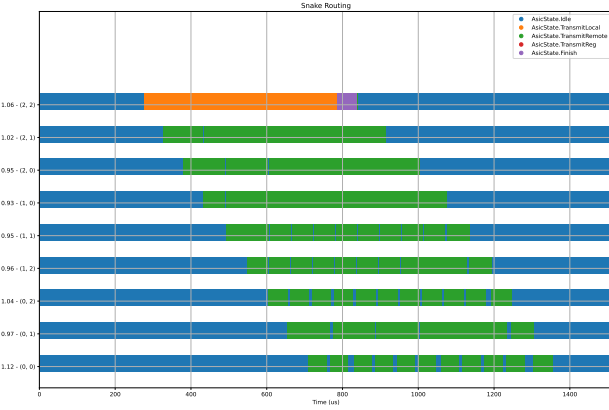
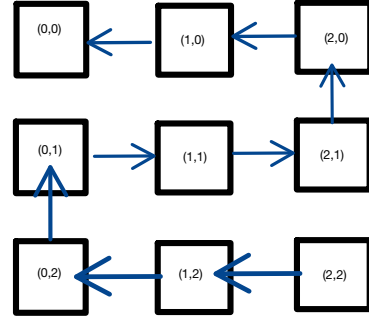


Figure 5.5: Example of timing ASIC state transitions in the simulation framework. The x-axis represents time in μs , and the different y-axis labels represent different ASICs within a 3×3 tile shown. The y-axis also indicates the relative frequencies of the ASICs in the tile, where the node at (0,0) has the fastest frequency, which is 12% faster than 30 MHz. The blue regions indicate that the ASIC is in the idle state. The first orange state indicates that this ASIC (2,2) received a register request from the aggregator node and is now sending its local data, concluding in the purple state, which is sending the event end word. The Packets drift apart in time as they are sent from slower to faster ASICs. Shown here is the possibility of packet drift due to asynchronous packet transfers that depends on the magnitude of the frequency drift between neighbor ASICs.



((a)) Snake Readout timing Diagram



((b)) Data Path in Snake Readout

Figure 5.6: A snake packet transaction example is shown. The broadcast is received by the further node $(2,2)$ and 10 data words are sent, followed by a event end word. Each packet tranverses through all nodes in the tile where remote packets are sent immediately.

Since the snake routing minimizes the number of edges, it also maximizes the number of ASICS responsible for sending remote data in the tile. This increases the number of remote transactions in a tile readout. This demonstrated by the amount of time ASICS are in the transmit remote state shown in Figure 5.3.

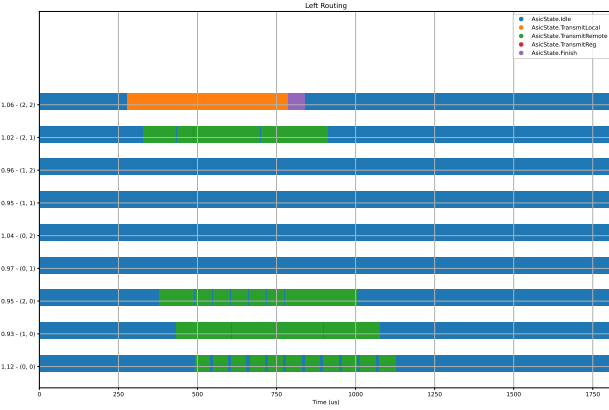
Left Timing Example

The naming convention for the "left" routing is arbitrary since the tile can be viewed from the opposite direction and the routing would appear "right". By "left" routing we mean a routing configuration in which the routed direction for all ASICS in all rows are in the same direction, except for the nodes which have no neighbor in that direction. These nodes then are routed "up" towards the aggregator. An example of a packet transfer with this routing configuration is shown in Figure 5.7.

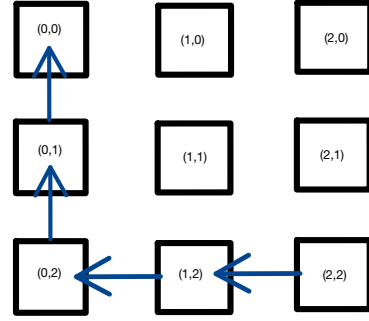
This routing configuration minimizes the path length for all nodes in the tile when the base-node is at the corner.

Trunk Timing Example

The final routing scheme we simulate we call the "trunk" routing. We name this routing the "trunk" because all data are sent to a central column within the tile and then up towards the edge base node. An example of a simple data transfer is shown in Figure 5.8.



((a)) Left Readout timing Diagram

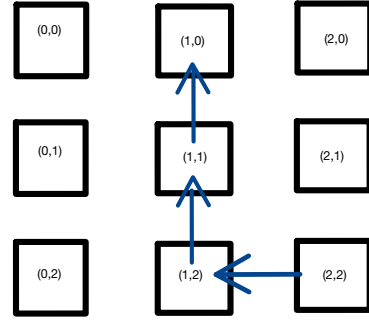


((b)) Data Path in Left Readout

Figure 5.7: A left packet transaction example is shown. The packet transfers begin with the furthest node (2,2) receives a broadcast from the aggregator. The data are then sent to the "left" and then "up" towards the base node, and finally to the aggregator node.



((a)) Trunk Readout timing Diagram



((b)) Data Path in Trunk Readout

Figure 5.8: A trunk packet transaction example of two data words and a single event end word is shown. This routing method allows for the fastest possible transaction time since it minimizes the edge lengths between the base node and all other nodes within the tile. In this 3×3 example shown, the base node is at (1,0), or in the middle.

For tiles of widths larger than three there are multiple choices for which column will be the trunk. In for example, a 4×4 tile can have either the second or third columns be the trunk. In all even width cases we test, we choose the smaller row value for simplicity. In the 4×4 case we choose the second column and in the 8×8 case, we choose the fourth ($(3,0)$) column instead of the fifth ($(4,0)$).

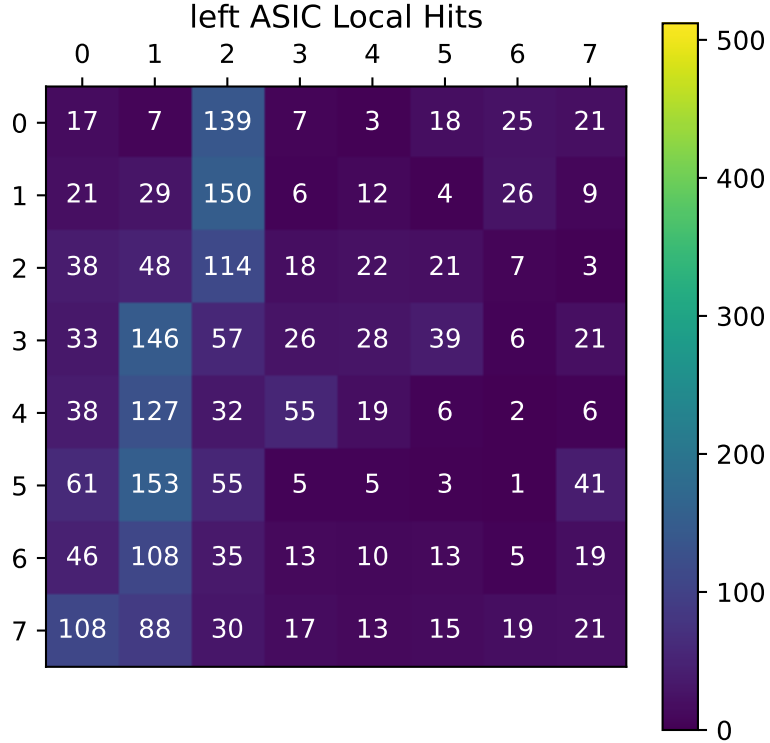
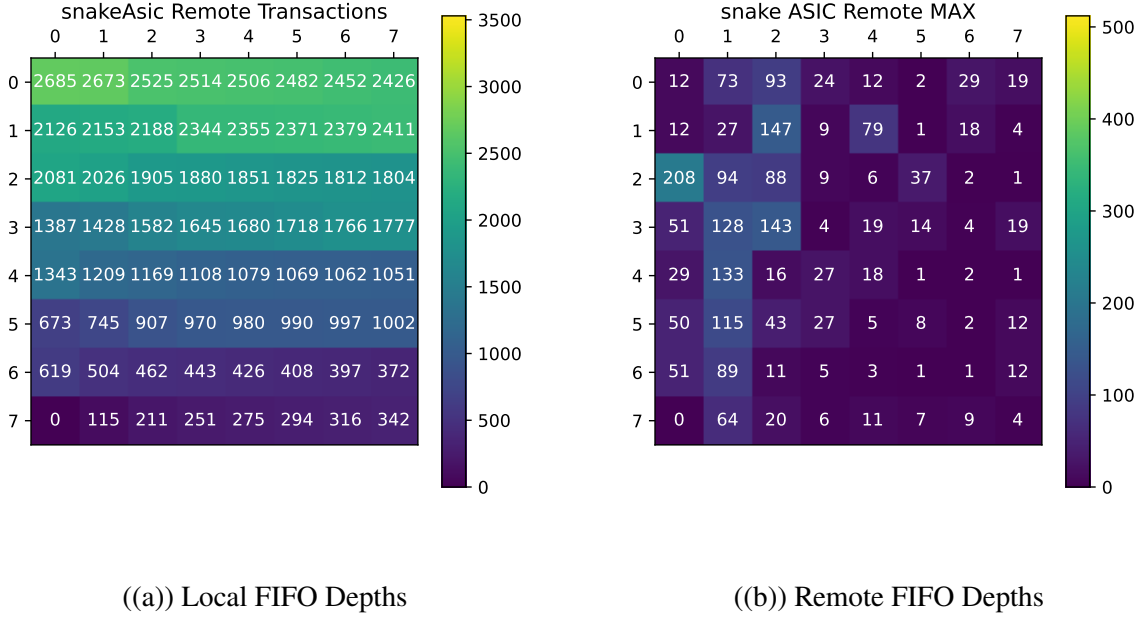


Figure 5.9: Example local FIFO distribution of a $\approx 3\text{GeV}$ ν_e event. The numbers over each tile represent the total number of writes which occurred to each local FIFO in the array. Even with the lowered resolution (each ASIC accounts for 16 pixels), different tracks are noticeable based on the FIFO depths. The maximum scale for the heatmap is chosen to be 512 resets.

The Pull Architecture and FIFO Depths

The "pull" architecture describes a tile configuration where data are only sent by ASICs within the tile when they receive a broadcast packet. We describe an example simulation event in this section with the pull architecture and the three routing methods to demonstrate which variables are recorded. The example presented in Figure 5.3 stores resets accumulated over ten seconds from both radiogenic backgrounds and a 3GeV ν_e event. The data shown are the total local FIFO transactions (writes) that occurred in the ten second run.

The figures shown in figs. 5.10 to 5.12 demonstrate how the data are accumulated onto the remote FIFO depths for the snake, left, and trunk routings respectively.



((a)) Local FIFO Depths

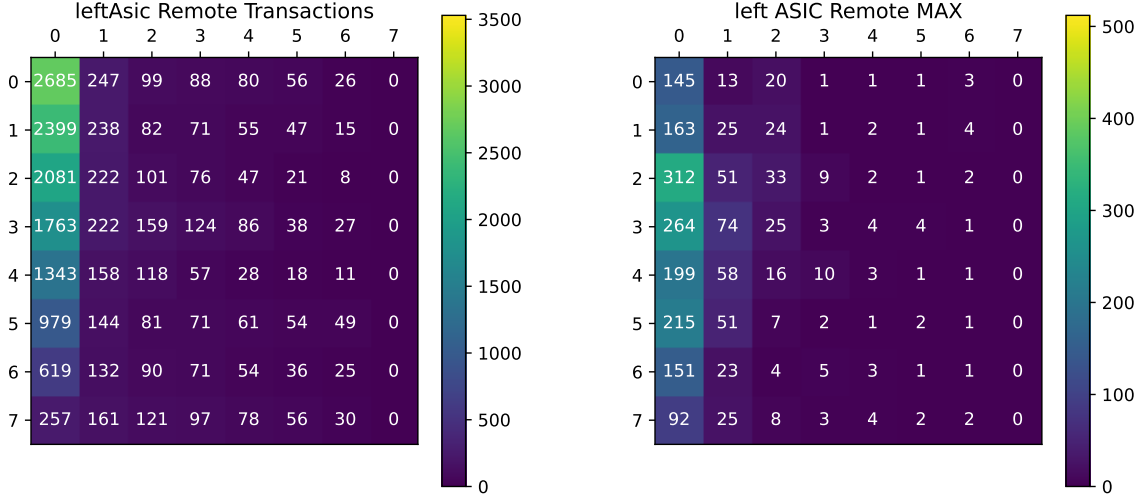
((b)) Remote FIFO Depths

Figure 5.10: Example of local (a) and Remote (b) fifo depths of the example neutrino event from 5.3 after processing. The colorbar to highlight the maximum number of transactions is used to indicate remote transactions which were happening for 2% of the total readout time of 10 seconds. The node which has the largest remote buffer depth corresponds to the ASIC with the slowest frequency as shown in Figure 5.2. The reason for this excess of buffer depth is due to packet buildup on the slow ASIC.

The following figures demonstrate why it is important to design all ASICs within a tile to meet the same specifications. Future Q-Pix ASICs within a tile will be exposed to events at or above these energy scales, and there is no guarantee (until the ASIC is in hand) what the frequency of its oscillator will be, or its location within a tile. In all three routing examples shown it was not the base node which experienced the most strain on its buffer depth, but the ASIC along the route path which had the lowest frequency.

The Push Architecture

The final simulated parameter to describe is the push architecture. Since the push architecture allows individual nodes to determine when packets can be sent all nodes must be inspected at each time step to check if a reset occurs before this new time window. If a reset occurs at a time before



((a)) Local FIFO Depths

((b)) Remote FIFO Depths

Figure 5.11: Example of local (a) and Remote (b) fifo depths of the example neutrino event from 5.3 after processing. The ASIC which has the largest remote buffer depth also corresponds to the ASIC with the lowest frequency as shown in Figure 5.2.

| Routing | Local Max | Remote Maximum | Ratio of Remote:Local |
|---------|-----------|----------------|-----------------------|
| Snake | 153 | 208 | 1.36 |
| Left | 153 | 312 | 2.04 |
| Trunk | 153 | 306 | 2.00 |

Table 5.2: Example results obtained from the three simulation examples for the pull architectures shown in the previous figures. The value of interest in determining the required remote FIFO depths for each ASIC is the maximum depth that occurred on any node. A memory optimized routing configuration is one that would introduce the least strain on the remote buffer depths for a given local buffer depth input.

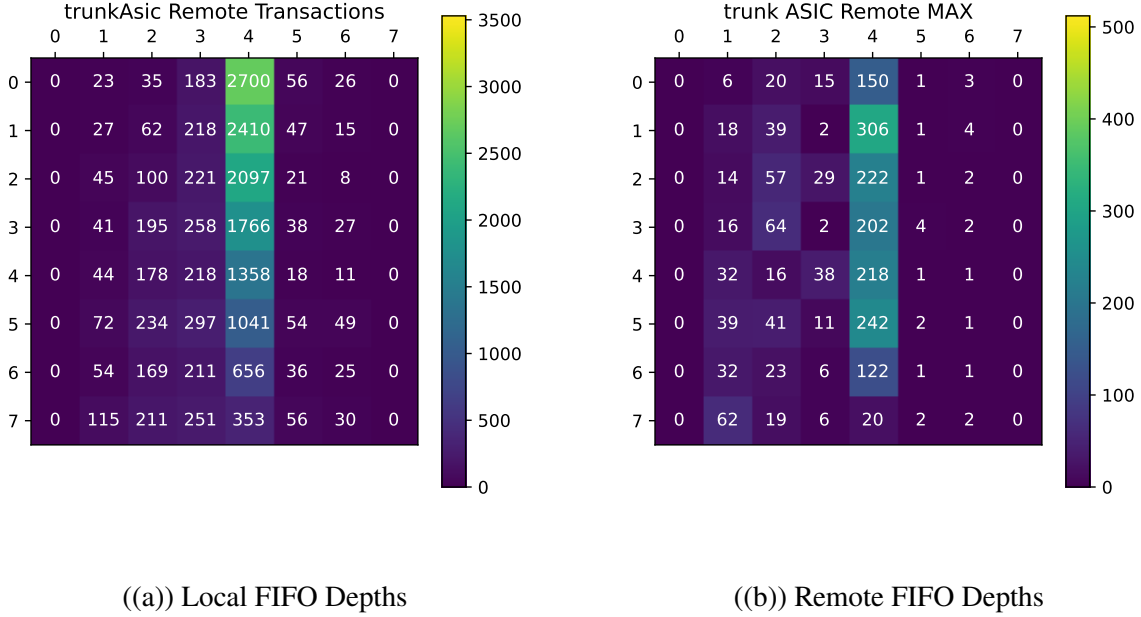


Figure 5.12: Example of local (a) and Remote (b) fifo depths of the example neutrino event from 5.3 after processing. The ASIC which has the largest packet buildup occurs at (4,1). This ASIC also corresponds to the ASIC which has the lowest frequency along the trunk column as shown in Figure 5.2.

the next simulation timestep, then the reset is removed from this node's hit list and is written to the node's local FIFO. The node will then see at this simulation timestep that the local FIFO is not empty, and leave its idle state to send this packet. An example of this process is shown in figure 5.3.

Every simulated time step is shown and recorded along the x-axis. The distance in time between simulation steps increases during packet transfers since the nodes state is fully determined during this time. This simplification is performed to speed up simulation run time.

5.4 Physical Simulation Studies

We now discuss the methodologies of the physical simulations used as input to the digital tile simulation described in the previous section.

Radiogenic Backgrounds as a Calibration Source

In this section we comment on the ability to, but do not perform, the auto-calibration of the reset loss per charge. The full charge calibration procedure is beyond the scope of the work presented here, due

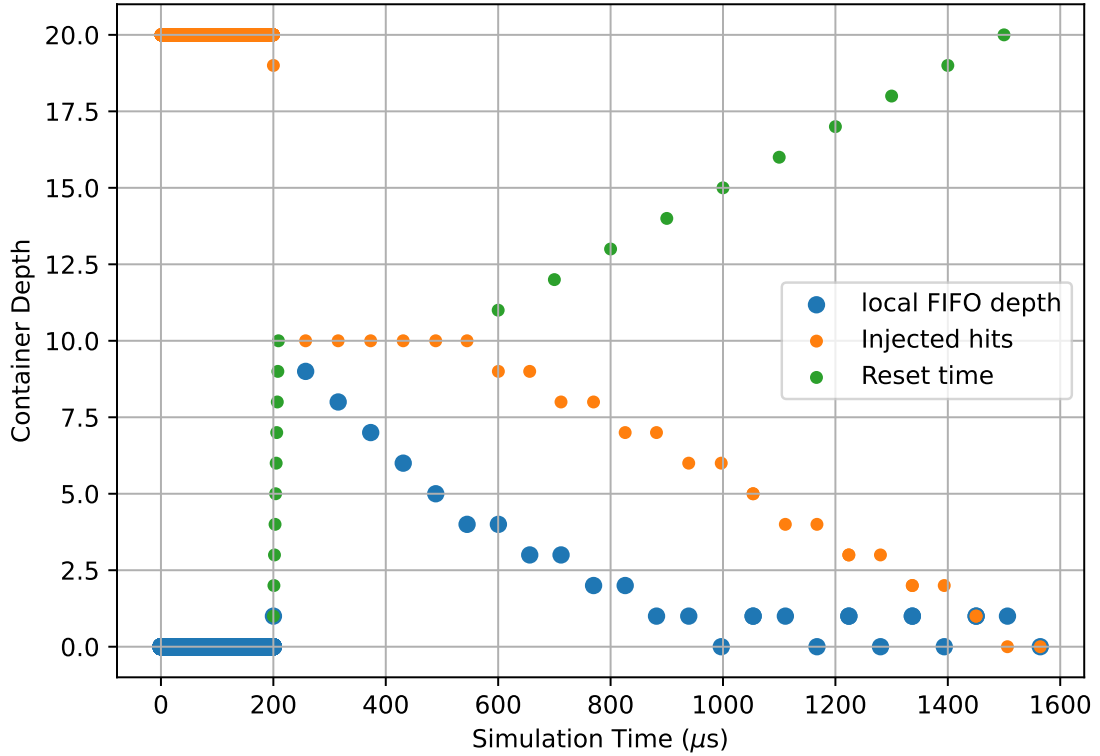


Figure 5.13: A simulated push architecture with 20 injected hits at different times. The time of the injected reset is indicated by the green points. Before the simulation is run a node has its hits injected into a storage (orange) list. Then, at each simulation time step ($\tau_{step} = 1\mu s$) the list is examined to see if a new hit will be written. When a hit is found the relative time of the node can move forward in time to when this packet will be completed in time, while all other writes can occur to the local FIFO. This is why the first local FIFO depth increases initially by one despite 10 nearly adjacent injected hits. On the next time step, the depth then moves to nine; the simulation has sent the first of the 10 packets, and records nine. This example correctly shows a maximum local FIFO depth of nine.

| Isotope | Rate [Bq/kg] | Region | Region Mass [kg] | Rate [Bq] | Number of Decays (per 10 s window) |
|-------------------|-----------------|-------------------------|---------------------|-----------|---------------------------------------|
| ^{210}Po | 0.2 | PD [Bq/m ²] | 2.46856 | 0.493712 | 5 |
| ^{60}Co | 0.0455 | CPA | 90 | 4.095 | 41 |
| ^{40}K | 0.49 | APA | 258 | 1,264.2 | 12,642 |
| ^{39}Ar | 1.010 | bulk LAr | 70,000 | 70,700 | 707,000 |
| ^{42}Ar | 0.000092 | bulk LAr | 70,000 | 6.44 | 64 |
| ^{42}K | 0.000092 | bulk LAr | 70,000 | 6.44 | 64 |
| ^{222}Rn | 0.04 | bulk LAr | 70,000 | 2800 | 28,000 |
| ^{214}Pb | 0.01 | bulk LAr | 70,000 | 700 | 7,000 |
| ^{214}Bi | 0.01 | bulk LAr | 70,000 | 700 | 7,000 |
| ^{85}Kr | 0.115 | bulk LAr | 70,000 | 8050 | 80,500 |

Table 5.3: The radiogenic background distribution is the same as that found in previous work [14]. For each 1000 second analysis the pre-rounded values are scaled up by a factor of 100 to achieve the correct normalization of events for each isotope. A key difference between the backgrounds is the origin or source of each background. Of special note is ^{40}K whose source location is the APA beams, and whose resets can be distinctly seen in Figure 5.4 as the slightly more active (yellow) region of the APA. Due to this source alone, it is likely that precise auto-calibration for charges will likely have to account for the pixel location within the APA.

to intracies that depend on the final implementation of the reset circuit as well as the replenishment circuit of the final Q-Pix ASIC. Since this ASIC does not yet exist, the true verification of this methodology is not yet possible. Nevertheless, we describe the relevant portions to the problem here, since the charge calibration along with the frequency calibration and timestamp measurements determine Q-Pix's z-position reconstruction.

The main idea behind the auto-calibration of charge at the pixel level relies on using the known (and near constant) input current from the radiogenic backgrounds (mostly ^{39}Ar) in the detector. If a perfectly known and constant input current (I_o) source was input to a pixel it would produce a resets separated by a constant time (τ_{rtd}). It would be a straight forward matter to calculate the charge per reset: $Q_o = I_o * \tau_{rtd}$.

Then, to analyze the ability for an auto-calibration procedure for Q-Pix it is important to analyze and understand the long-running charge accumulation (resets) from backgrounds present in the LAr. We use the following list of radiogenic sources of 10 distinct runs of 1000 seconds each. Further details on radiogenic backgrounds in LAr can be found at [7, 84, 85]

The well-known C++ based Geant4 [80] simulation toolkit is used to simulate particle decay and

ionizing particle interactions within the LAr volume. We use the energy deposited along the track from each ionizing particle with the W-value for liquid argon (23.6 eV) to determine the number of electrons deposited in the LAr. The resulting number of electrons are then uniformly deposited over the individual track. Then we calculate the probability of recombination for each electron following the "modified box" model [86].

The time and location of drift for each electron is calculated with an applied transverse and longitudinal diffusion with values taken from Table 1.3. The simulations for all particle interactions are run individually with a uniform random sampling of the initial decay time interval within the 1000 second window. All of the hits are then sorted by increasing time, so that the first hits read are the hits which occur the earliest. Sorting the hits by time before accumulating charge ensures that the resets happen at the correct time.

This simulation produces $\mathcal{O}(10^{11})$ hit interactions which produce $\mathcal{O}(10^{14})$ electrons, which in turn produces $\mathcal{O}(10^9)$ resets. To reduce the memory utilization of the simulation the electrons are accumulated on a hit-by-hit basis and are subdivided into a pre-determined 4×4 cross-sectional area of the detector. Each cross-sectional area defines a pixel. The dimension of the LArTPC volume is $2.3\text{ m} \times 6.0\text{ m}$ which divides into 575 pixels in the x-direction and 1500 pixels in the y-direction. There are then a total of 862,500 pixels, which store location and reset information.

As an example, the total resets from 1000 seconds of the simulation are shown in Figure 5.4. The most active pixel receives ≈ 220 resets during this simulation time. The bins for the histogram are at the pixel level, and represent the $4 \times 4\text{ mm}^2$ of each pixel.

Additional information is tracked for each reset to identify the contribution of each radiogenic background for each reset. A reset occurs when $6250\text{ }e^-$ have accumulated on a pixel. The time recorded for the reset is the same as the time the simulation calculates the last of the required 6250 electrons to arrive at the designated pixel region. This optimization was added to the existing simulation framework to separate the unknown analog contribution to the timing uncertainty from the physical simulation.

In practice, the analog front-end reset circuit obviously takes time to respond to added charge and to issue a replenishment and reset commands. There will always be some delay between the final electron's arrival, the time of the analog reset, the replenishment circuit, and the time recorded on the digital back-end. However, for the purposes of this analysis, we assume that this reset and replenishment circuit activity can happen more quickly than the average local oscillator of

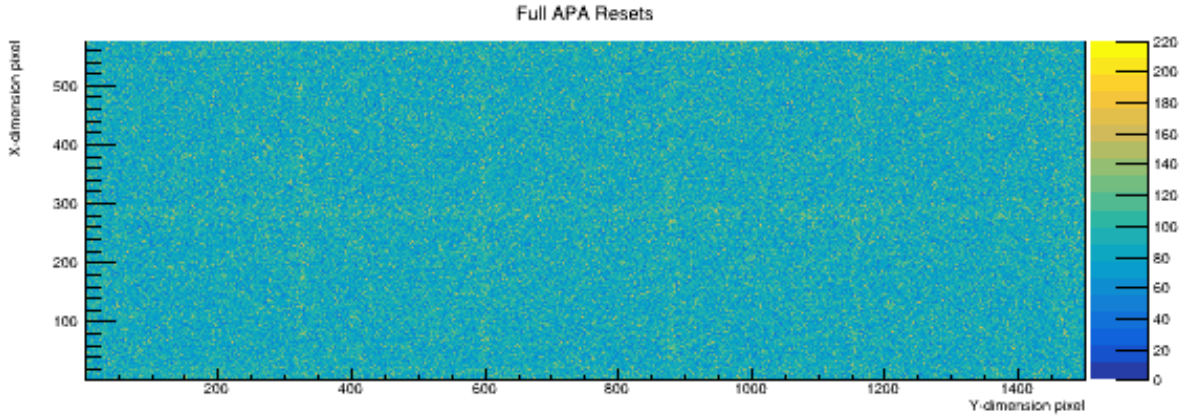


Figure 5.14: Full 1000 second of radiogenic background source simulation input into all pixels within the APA. A close examination of the resets can reveal the additional resets from the backgrounds which are location dependent. The majority of the uneven distribution of resets occur at the location of the APA bars due to the ^{40}K isotope.

the digital back-end. Therefore this analysis assumes the best timing measurement based on the digital back-end. The time measurement is then limited only by the clock frequency of each local oscillator. Finally, we comment that this optimization of the timing of the analog front-end affects only the time values, and by extension, the reconstruction of the particle tracks. It does not affect the total amount of charge, and therefore the total number of resets recorded by each pixel.

Any combination of the backgrounds can contribute some or all of the electrons required to produce a reset. The contribution of the total electrons for each of the radiogenic sources are shown in Figure 5.18. We refer to the contribution of the number of the electrons to the reset as the "weight" of the reset.

The ability to perform a charge auto-calibration using radiogenic events depends on the background to provide a reliable average input current source. We use only the data presented in Figure 5.4 and calculate the mean time between resets for all pixels. For this simple calculation, we simply take the total number of pixels (4096) and divide by the total number of recorded resets (411152) and obtain an average RTD of 9.96 seconds.

A very rough expectation of background current is $I_o \approx 100 \text{ aA}$. We can then use the following

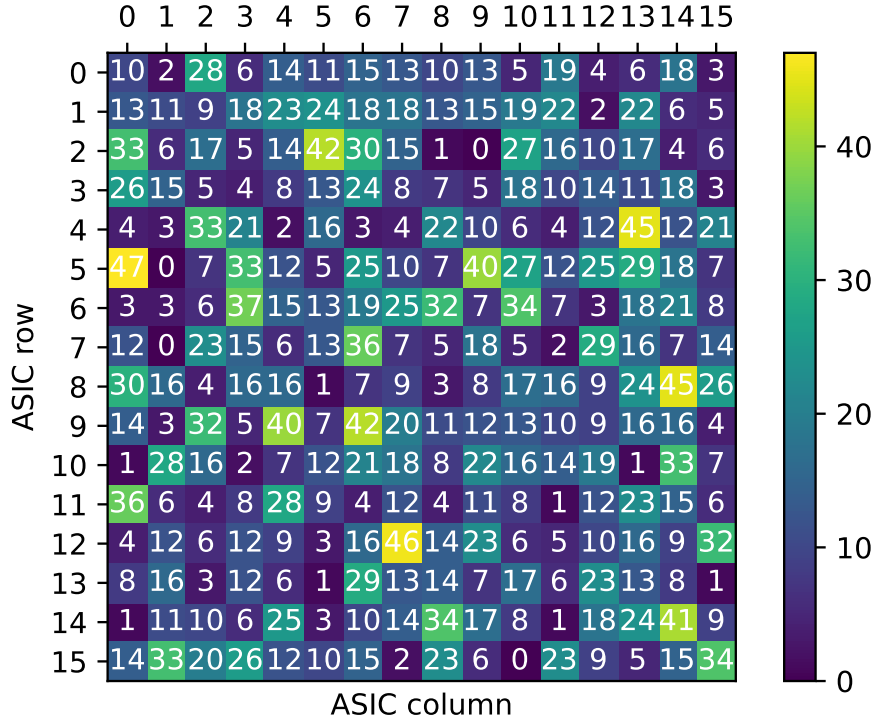


Figure 5.15: Baseline noise input for the digital simulation from all radiogenic sources and background leakage current. This figure shows the total resets in the 10 second window for the 16×16 tile. The other tile size configurations (4×4, 8×8, 10×14) also use these reset data for background noise. All tiles start with the top left node as their origin node.

equation to calculate:

$$I_o = \frac{Q_o}{\tau_{rtd}}$$

solving for Q_o with $\tau_{rtd} = 9.96$ and $I_o \approx 100$ aA, we obtain:

$$Q_o \approx 100 * 10^{-18} * 9.96 / 1.6 * 10^{-19} \approx 6225$$

More sophisticated analysis will be needed for pixel level charge calibration. The contrived derivation above assumes equal capacitance and charge replenishment on all pixels, which in practice is not necessarily true. Furthermore, additional tests can likely be done for each pixel by comparing the peak of the distributions as shown in Figure 5.4. Such an analysis is not appropriate yet since it is not yet known what the leakage current will be in the Q-Pix ASIC. As shown in both Figure 5.4 and Figure 5.18, the contribution from noise is not negligible. Therefore, any true

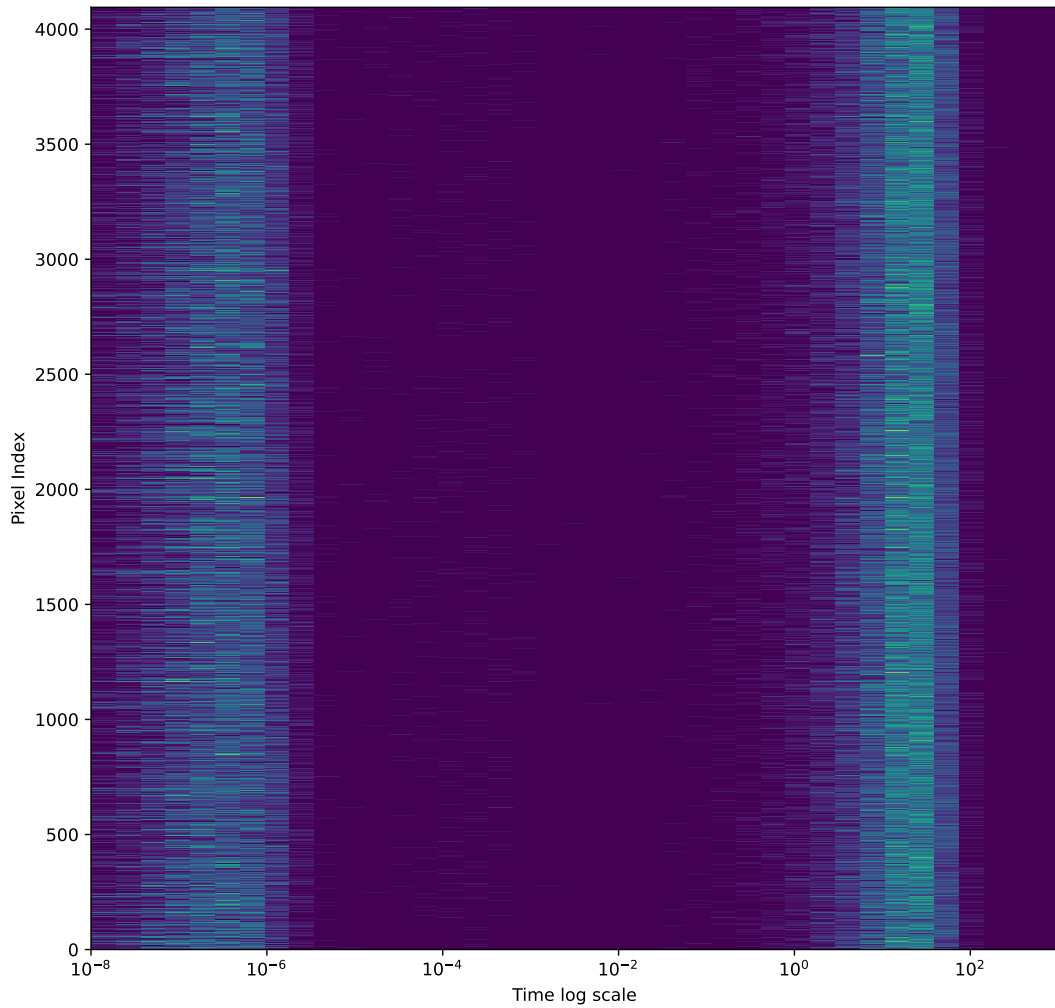


Figure 5.16: All 4096 pixels in the 16×16 tile for 1000 seconds of radiogenic data. The y-axis represents a different pixel, and the x-axis is a log-scale time axis with even bin widths. There are two clusters of resets for different time intervals. The first large cluster of resets occurs at $\approx 10^{-7}$ seconds and is due to a single radiogenic decay event causing additional resets. The second large cluster of resets occurs at ≈ 10 seconds. This second cluster of resets is caused from the first reset of a new radiogenic decay event. The ability to perform a charge calibration per pixel may depend on accurately resolving the mean for this "long period" RTD.

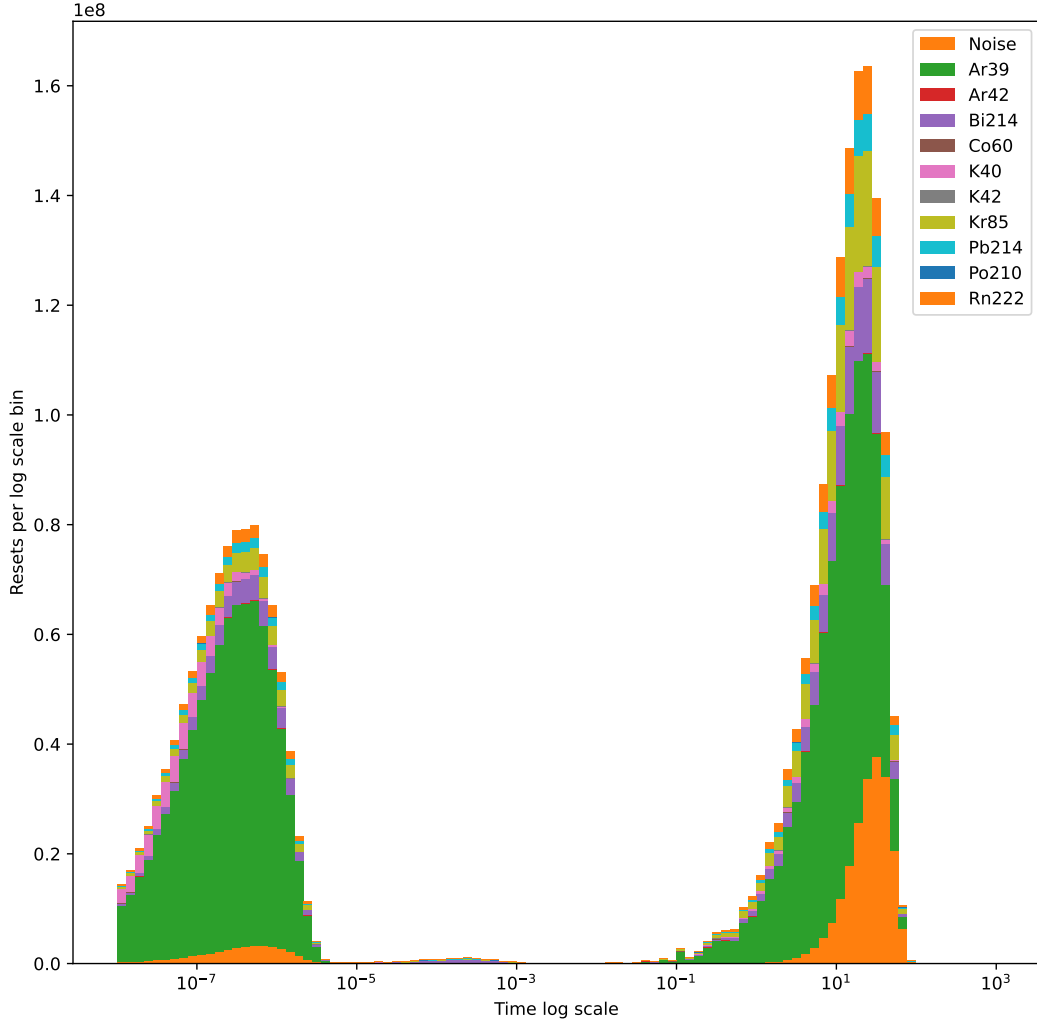
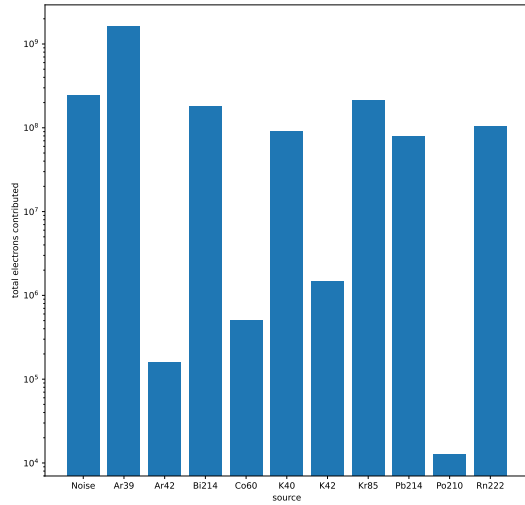
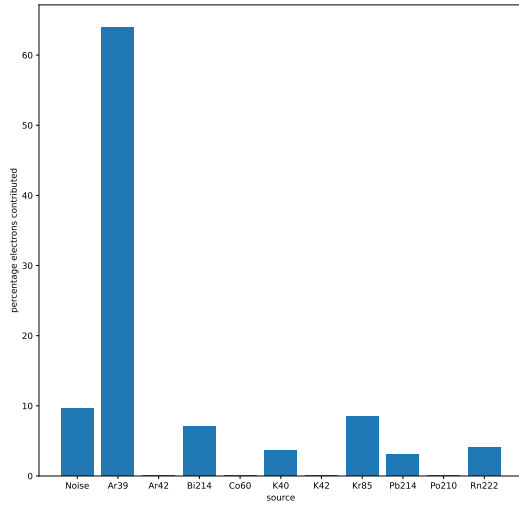


Figure 5.17: All 4096 pixels in the 16×16 array for 1000 seconds of radiogenic data. These data are the same as those shown in Figure 5.4, where all pixel RTDs are binned together. There are two clusters of resets on two different time scales. The first cluster of resets near at $\tau_{rtd} \approx \mathcal{O}(10^{-7})$ is due to events which produce more than one reset. The second cluster of resets near at $\tau_{rtd} \approx \mathcal{O}(10^1)$ are from a "waiting" period where there is no charge buildup from decays and only background noise. The dominant source of electrons on each pixel is from the ^{39}Ar , with a non-zero contribution from leakage. The leakage current value used in this simulation is 10 aA.



((a)) Contribution of total electrons.



((b)) Contribution of electrons by percentage.

Figure 5.18: Both figures indicate a comparison of the amount of electrons deposited on all pixels in the tile shown in Figure 5.4. Plot (A) represents the total number of electrons on a log scale. As expected, ^{39}Ar contributes the majority of background charge. The leakage current used is 10 aA, and represents about 10% of the total contribution of electrons. This implies that leakage currents from the front circuit which are ≈ 100 aA will contribute nearly as much electrons to the steady-state RTDs as the radiogenic backgrounds.

analysis of the charge auto-calibration ability of Q-Pix awaits studies of both the leakage current and replenishment circuits of the analog frontend.

Reset Contribution of Sources

5.5 Neutrino Beam Studies

Here we discuss the implementation of the digital framework within the high energy regime. For this we use as an input neutrino events from the Long-Baseline Neutrino Facility (LBNF) [5] and take the unoscillated flux of neutrinos which were used in [10]. These neutrino flux are simulated using GENIE [15], v2.12.10. The interaction distributions for both the forward and reverse horn current directions are shown in Figure 5.5.

We do not perform any calculation involving the oscillation on the input neutrino flux. The reason for this is that the digital back-end should be able to fully record data from all possible ν_l events

regardless of interaction type, not only the intended ν_e appearance spectra. It is equally important for a future readout to be able to correctly tag noise (ν_μ , or ν_e from the beam, etc.). For example, sensitivity to mass ordering and CP violation rely on the ability to measure ν_μ disappearance in addition to the ν_e appearance.

What will be shown in the upcomming sections is that capability of the digital back-end depends on the energy deposited in the volume of the LAr. By the virtue that oscillations change only the flavor (not the energy) of the ν , the constraints of the back-end do not depend on if more (or less) ν_e are measured compared to $\bar{\nu}_e$, provided the back-end is capable of fully measuring both events. Furthermore, by using the unoscillated flux of the neutrinos at the near detector, the neutrinos will be of necessarily higher energy than the expected flux at the far detector. The use of high energy helps in establishing what we will show as the upper-bound for the required local and remote FIFO depths for each ASIC.

Neutrino Event Parameters

Table 5.5 describes the parameters of each input for the simulation. The parameters used to vary the tiles for these neutrino input energies are shown on Table 5.2.

The Q-Pix readout presented here is designed for use in a LArTPC at the scale of DUNE-FD 10kT module 1.6. In order to test what kinds of requirements this readout will need we use high energy neutrino interactions as discussed in Section 5.5. The different selection parameters for each event are neutrino flavor, neutrino energy, horn current direction, Z-position vertex position, and source neutrino momentum direction (θ_z). We define the beam direction (the direction parallel to the surface of the APA) as $\theta_z = 0$. The X and Y positions are held constant for all interactions, at X = 120 cm and Y = 3200 cm. The coordinate system we use, as well as a slice of the APA within a module are shown in Figure ??.

The LBNF beam is not the only source of high energy particles DUNE will detect. Other high energy (≈ 10 GeV) interactions may come from other sources. These other high energy events (such as nucleon decay, cosmic neutrinos) may also deposit energy on GeV scales per interaction. These sources may interact with their net momentum vector pointing in any direction. For this reason we also test ν_e and ν_μ interactions at $\theta_z \pm 90^\circ$; this direction causes the secondary ionizing particles to carry momentum along the direction parallel to the pixel's surface normal. These two

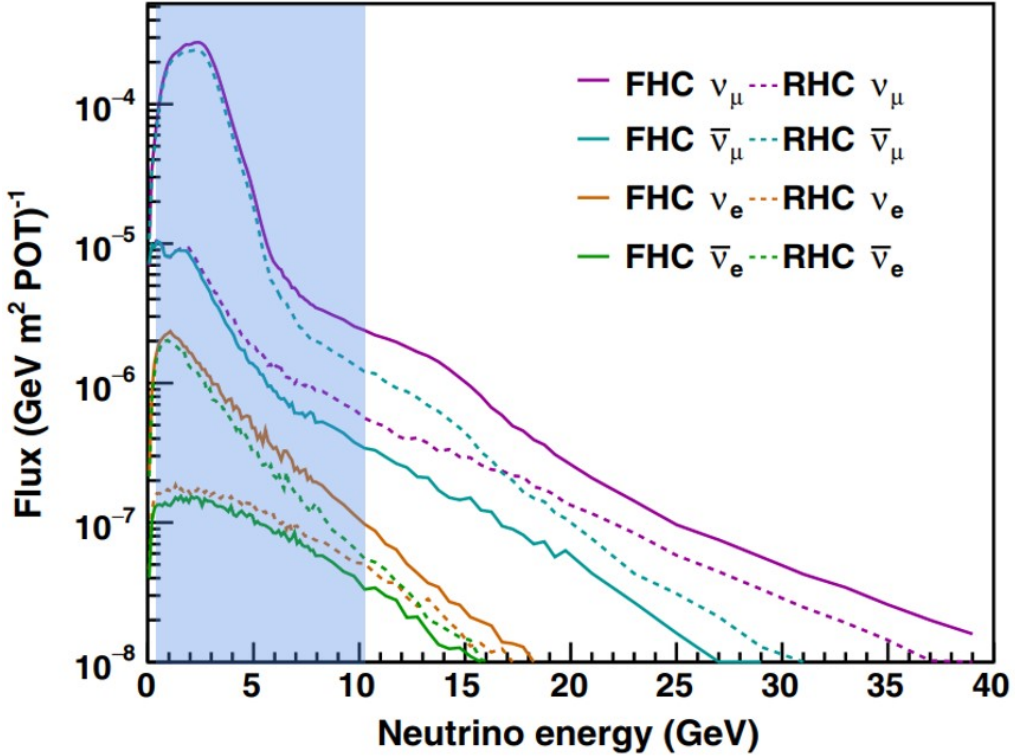


Figure 5.19: Flux spectrum of neutrinos from the neutrino beam used in this study. This figure is taken from [87]. Highlighted in blue is the reconstructed energy range of neutrinos that are used to seed the interaction with the APA LAr's volume.

momentum directions, though unphysical for beam interactions, still present possible interactions types within the scope of DUNE's proposed physics program [77].

Neutrino Event Results

Every simulated neutrino interaction generates some number of resets which are collected onto the pixel plane. The purpose of the study explored by the parameters described in Table 5.5 is to investigate the charge resets these interactions produce; we pay particularly close attention to

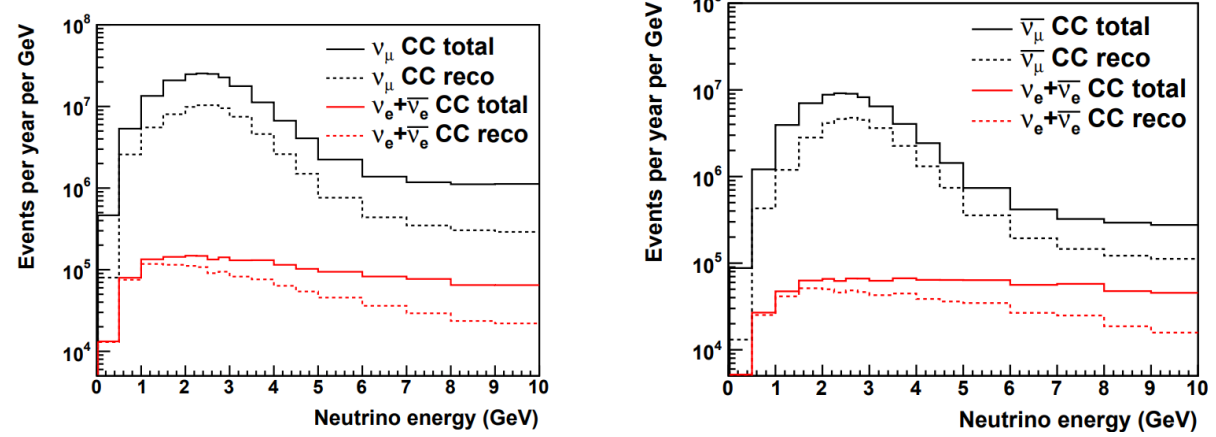


Figure 5.20: Rate of CC neutrino interactions based on flavor as a function of true neutrino energy. Figure is taken directly from [10]. Right is shown the neutrino interaction distribution for the forward horn current. The left image is for the reverse horn current. Both images assume an average exposure rate of 1.2 MW from LBNF beam.

ASICs where the number of resets (energy deposited) is the largest in a given event.

We bin the maximum number of resets in a 4×4 pixel array, or ASIC, for every neutrino event. The plot Figure 5.23-(A) shows a ν_e event and Figure 5.5 shows these resets binned into pixels. For every event we take the maximum ASIC value and use that as an entry into a histogram. Next, we take the integral of each histogram as shown in (B) of Figure 5.23 and (B) of Figure 5.24. The value of this integral gives the percentage of fully events a function of local FIFO depth.

Neutrino Energy Deposit

True neutrino interaction energy is notoriously difficult to reconstruct. The neutrino itself carries no charge and its track is not directly reconstructed in the LAr. Other effects such as hadronization make perfect energy reconstruction of the neutrino interaction impossible by principle. For these reasons we show how the resets and ASIC FIFO depths vary both by the energy deposited into the

| Name | Values | Relation |
|----------------|--|--|
| ν_l | $\nu_e, \bar{\nu}_e, \nu_\mu, \bar{\nu}_\mu$ | Oscillation measurements require sensitivity to measurements for both ν_e appearance, and ν_μ disappearance. |
| ν_l Energy | 0.25 GeV to 10 GeV, in steps of 0.25 GeV | neutrino energy determines output secondary energy, which causes more resets and directly affects buffer depths. |
| Horn Current | Forward and Reverse | Beam horn current direction affects neutrino flux, as shown in Figure 5.5. Additionally, mass hierarchy measurements (according to the MSW effect [72]) require difference in measurements of appearance probability for ν_e and $\bar{\nu}_e$. |
| Z-position | 10 cm, 80 cm, 180 cm, 280 cm, 350 cm | Interaction z-position above the anode plane. Interactions which happen further from the collection plane have more time to diffuse or recombine. |
| θ_z | $0^\circ, \pm 2^\circ, \pm 90^\circ$ | Different momentum angles are different Z-positions, in general, direct ionized particle tracks within the active volume. |

Table 5.4: The different neutrino simulation parameters which are passed into Geant4 based simulation. The original interaction products are generated using GENIE [15] v2.12.10. The output products of the neutrino interaction produced from GENIE are then configured using the different parameters described above. We select ν_l events for different energies in bin-widths of 250 MeV; We follow the same bin width as is done in [16] for their neutrino oscillation analysis. A selection of 100 events for each ν_l is taken within each energy bin, for a total of 3900 ν_l events for each horn current direction, z-position, and θ_z selection. Since there are two current directions, four ν_l , five z-positions, and five θ_z positions, a total of 780,000 neutrino events are simulated.

LAr as well as the true neutrino energy.

Figure 5.25 shows the relationship between the true ν_e energy and the max FIFO depth as well as the total APA resets. Figure 5.26 shows the same relationships instead as a function of the energy deposited.

5.6 Neutrinos, Backgrounds, and Routing

A valid reconstruction requires all packets to be collected regardless of neutrino type, energy within the valid range, interaction vertex, and should also be able to accept a range of incoming momentum angles.

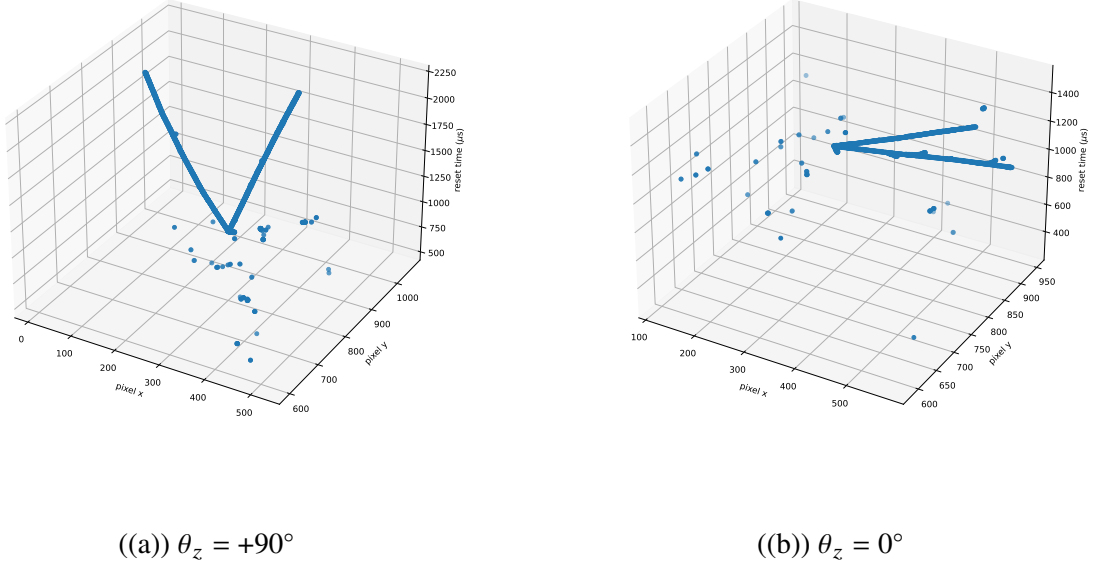


Figure 5.21: Same ν_e interaction at $Z\text{-position} = 180\text{cm}$, which is in the middle of the drift length of the APA. Image (A) has the incident ν_e momentum rotated upwards ($\theta_z = +90^\circ$). Image (B) has the incident ν_e had momentum along the beam direction ($\theta_z = 0^\circ$). Since there are five different z -positions, and five different θ_z values, each of the 3900 ν_l interactions are repeated 25 times. These two plots show two of those 25 examples.

Combining the Digital and Physical Simulations

5.7 Summary and Further Studies

Future Neutrino Oscillation Studies

Although an analysis of the reconstruction of the events involving oscillation are slightly beyond the scope of the work presented here, we provide a brief summary of how the work presented here helps in that future analysis.

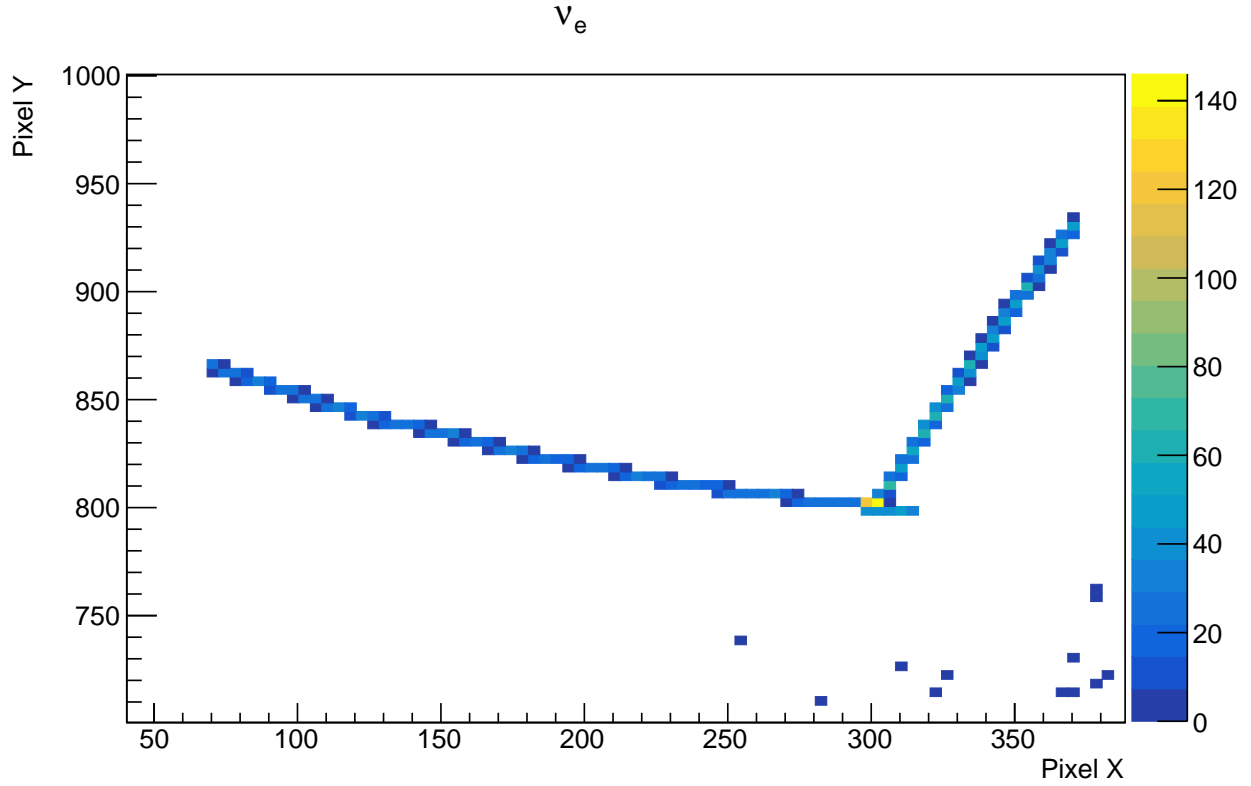


Figure 5.22: The same ν_e event as the one shown in Figure 5.21-(A). The plot is zoomed into to the region of interest where the bin widths represent the pixels dimensions in the collection plane. The energy of this ν_e was 546.1 MeV, and considering that each reset requires 0.1475 MeV, the maximum number of resets this event could produce is ≈ 4368 . The histogram records 3733 total resets. The most active pixel received 144 resets. When the pixels are binned into ASICs (4×4 pixels) the maximum number resets an ASIC received is 347.

| Freq. | Tile Size | Avg. Local Hits | S. Tot | S. Per. | L. Tot. | L. Per. | T. Tot. | T. Per. |
|-------|-----------|-----------------|----------|---------|---------|---------|---------|---------|
| 5% | 16 | 772.001 | 423.293 | 42.329 | 166.403 | 16.640 | 138.380 | 13.838 |
| 0.5% | 16 | 829.541 | 449.861 | 44.986 | 177.357 | 17.736 | 147.346 | 14.735 |
| 5% | 64 | 2184.255 | 1332.440 | 133.244 | 286.929 | 28.693 | 227.595 | 22.759 |
| 0.5% | 64 | 2321.148 | 1400.794 | 140.079 | 301.775 | 30.178 | 239.087 | 23.909 |
| 5% | 140 | 3712.921 | 2298.912 | 229.891 | 355.037 | 35.504 | 262.448 | 26.245 |
| 0.5% | 140 | 3944.215 | 2416.778 | 241.678 | 373.173 | 37.317 | 275.614 | 27.561 |
| 5% | 256 | 6231.886 | 4020.649 | 402.065 | 465.629 | 46.563 | 354.405 | 35.440 |
| 0.5% | 256 | 6592.433 | 4209.196 | 420.920 | 487.090 | 48.709 | 370.695 | 37.070 |

Table 5.5: Transaction Data

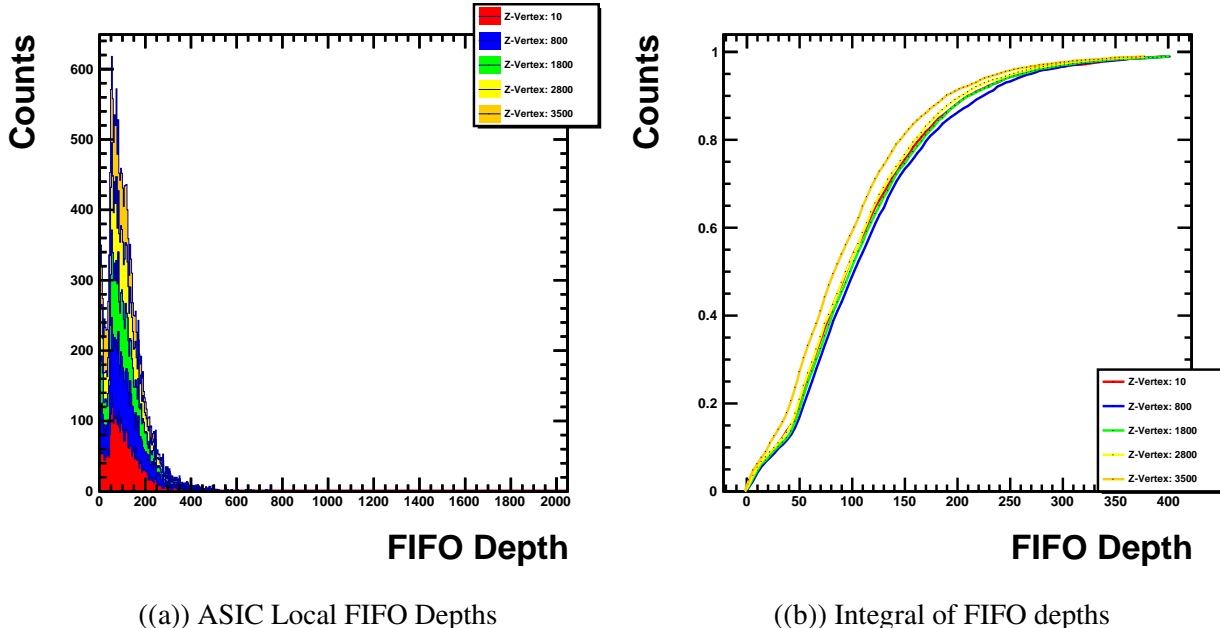


Figure 5.23: Example ν_e events for different z-position of the vertex with $\theta_z = 0$ held constant. Plot (A) bins the maximum value of local FIFO depth for all 3900 events (ν_l energies between 250 MeV - 10 GeV) for variable z-position and $\theta_z = 0$. Plot (B) shows the running integral for each histogram shown in plot (A). The integral continues until 99% of all events are counted. This process is repeated for all 200 possible parameter choices as discussed in Table 5.5.

| Freq. | Tile Size | Local Hits | 95-S | 99-S | 95-L | 99-L | 95-T | 99-T |
|-------|-----------|------------|------|------|------|------|------|------|
| 5% | 16 | 939 | 320 | 1014 | 535 | 1736 | 607 | 1971 |
| 0.5% | 16 | 1014 | 322 | 975 | 603 | 1949 | 652 | 2125 |
| 5% | 64 | 1200 | 598 | 2191 | 1098 | 4394 | 975 | 4295 |
| 0.5% | 64 | 1307 | 403 | 1328 | 970 | 4298 | 974 | 4521 |
| 5% | 140 | 1182 | 852 | 3486 | 1455 | 6558 | 1343 | 6309 |
| 0.5% | 140 | 1393 | 440 | 1464 | 1327 | 6616 | 1382 | 6757 |
| 5% | 256 | 1456 | 1039 | 3637 | 2026 | 7679 | 2008 | 8250 |
| 0.5% | 256 | 1670 | 527 | 1668 | 1773 | 7460 | 1784 | 7368 |

Table 5.6: Buffer Data

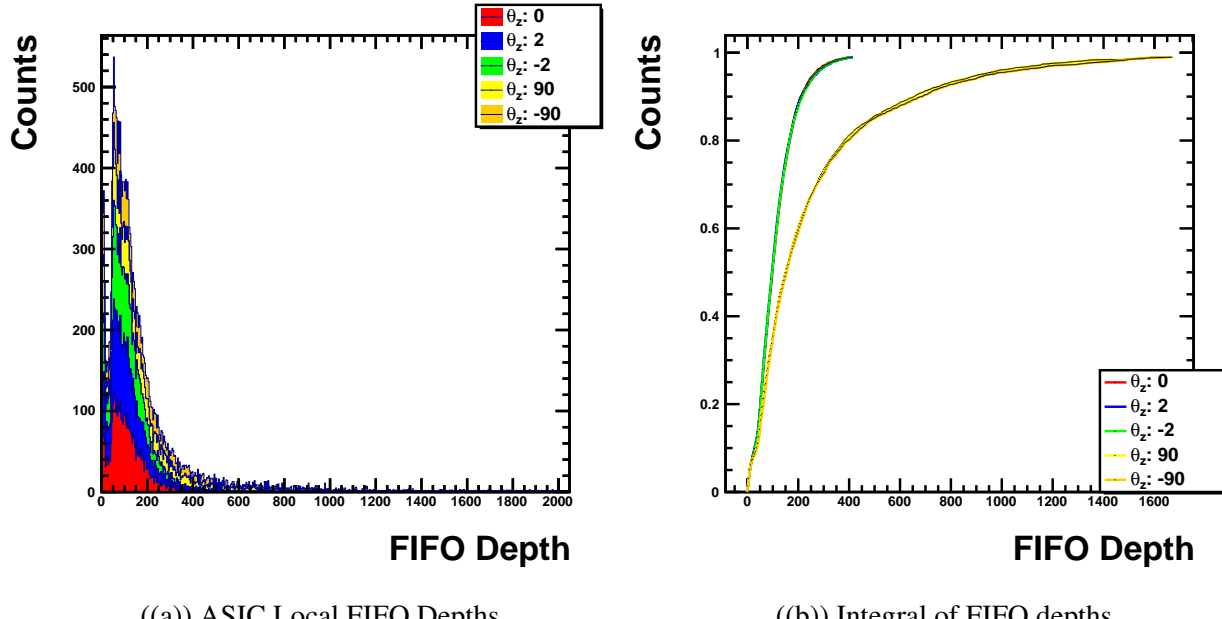


Figure 5.24: Example ν_e events for different θ_z with the vertex held constant with z-position = 180cm. This is a similar plot to Figure 5.23 with the exception that θ_z is varied and the z-position is held constant at $z = 180$ cm. A striking difference to note here is the run away effect of the large values of θ_z .

| Freq. | Tile Size | Snake Fit | Left Fit | Trunk Fit | Push Fit |
|-------|-----------|-----------|----------|-----------|----------|
| 5% | 16 | 1.041 | 1.823 | 2.082 | 0 |
| 0.5% | 16 | 0.948 | 1.879 | 2.039 | 0 |
| 5% | 64 | 1.623 | 3.176 | 2.969 | 0 |
| 0.5% | 64 | 1.006 | 2.514 | 2.727 | 0 |
| 5% | 140 | 1.966 | 3.506 | 3.481 | 0 |
| 0.5% | 140 | 1.021 | 3.033 | 3.131 | 0 |
| 5% | 256 | 1.981 | 3.616 | 3.913 | 0 |
| 0.5% | 256 | 1.027 | 3.243 | 3.336 | 0 |

Table 5.7: Transaction Fit Results

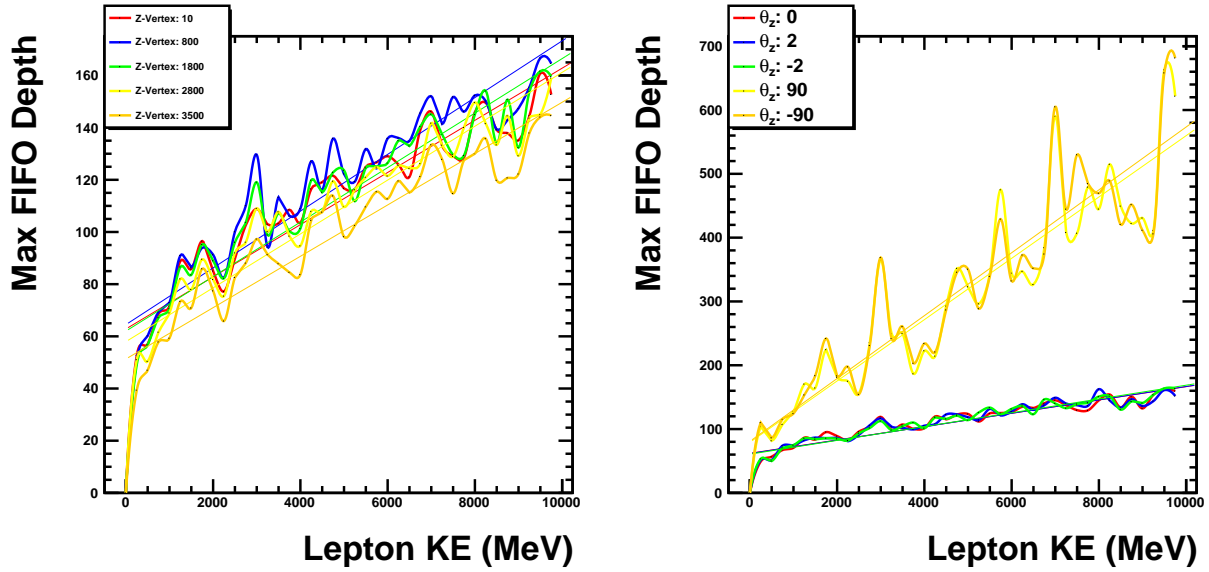


Figure 5.25: Comparison of Buffer depths as a function of energy for different parameters of θ_z and z-position. There is a large variance between the true ν_l incident energy and the actual energy deposited in the LAr. This is the reason why only the means are plotted for each energy bin.

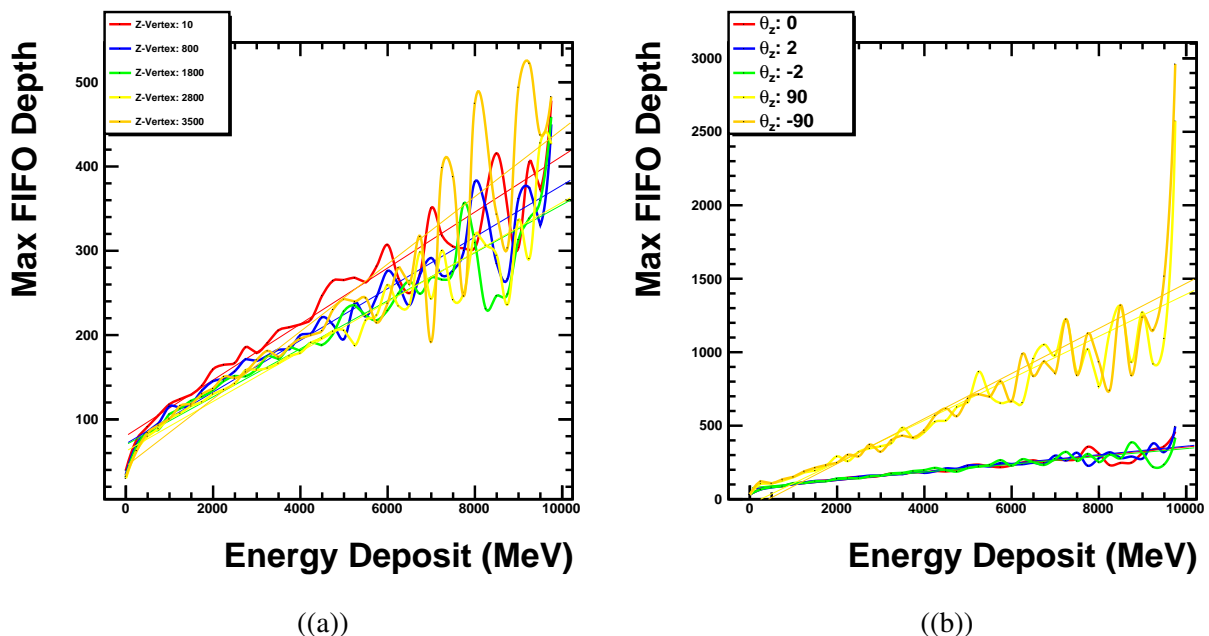
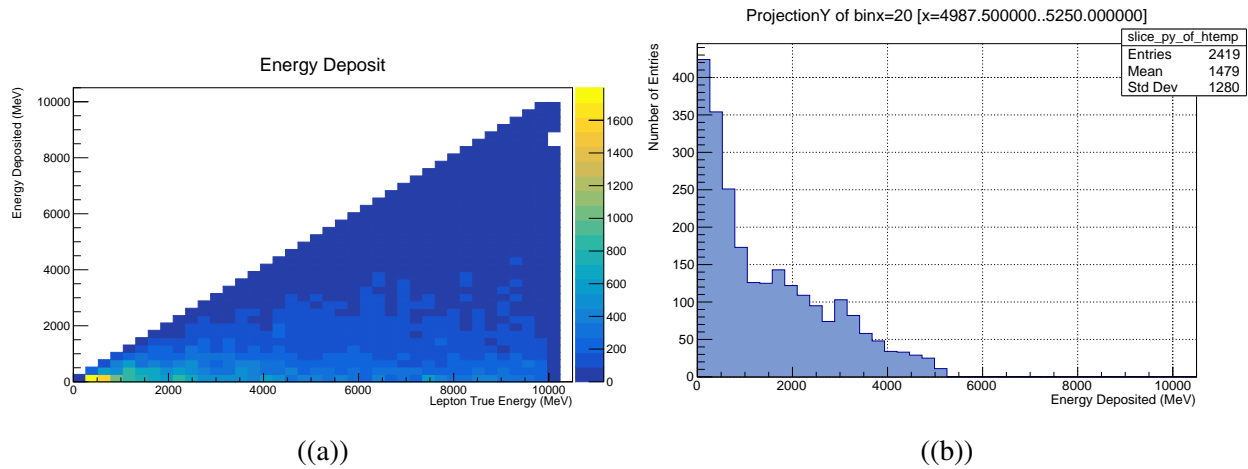


Figure 5.26: A comparison of ASIC resets vs the energy deposited into the LAr. Plot-(B) shows for Z-position=10 cm ends at ≈ 2 GeV since no ν_e events deposit this much energy into the LAr. Both plots indicate that the



((a))

((b))

Figure 5.27: Plot-(A) shows a comparison of the energy deposited into the LAr as a function of the input neutrino, which in this case is ν_e . Plot-(B) shows a projection against the y-axis for a single bin. The maximum allowed total energy deposited is limited to the total energy of the input neutrino. However, the lower bound for all energies is still, obviously, zero. Therefore, as the input neutrino energy increases the upper bound also increases. The mean value of Plot-(B) indicates that even for a maximum allowed total energy of 5 GeV the mean (average) energy deposited per event is 1479 MeV. Most interactions deposit less than 2 GeV into the LAr, as shown in Figure 5.27.

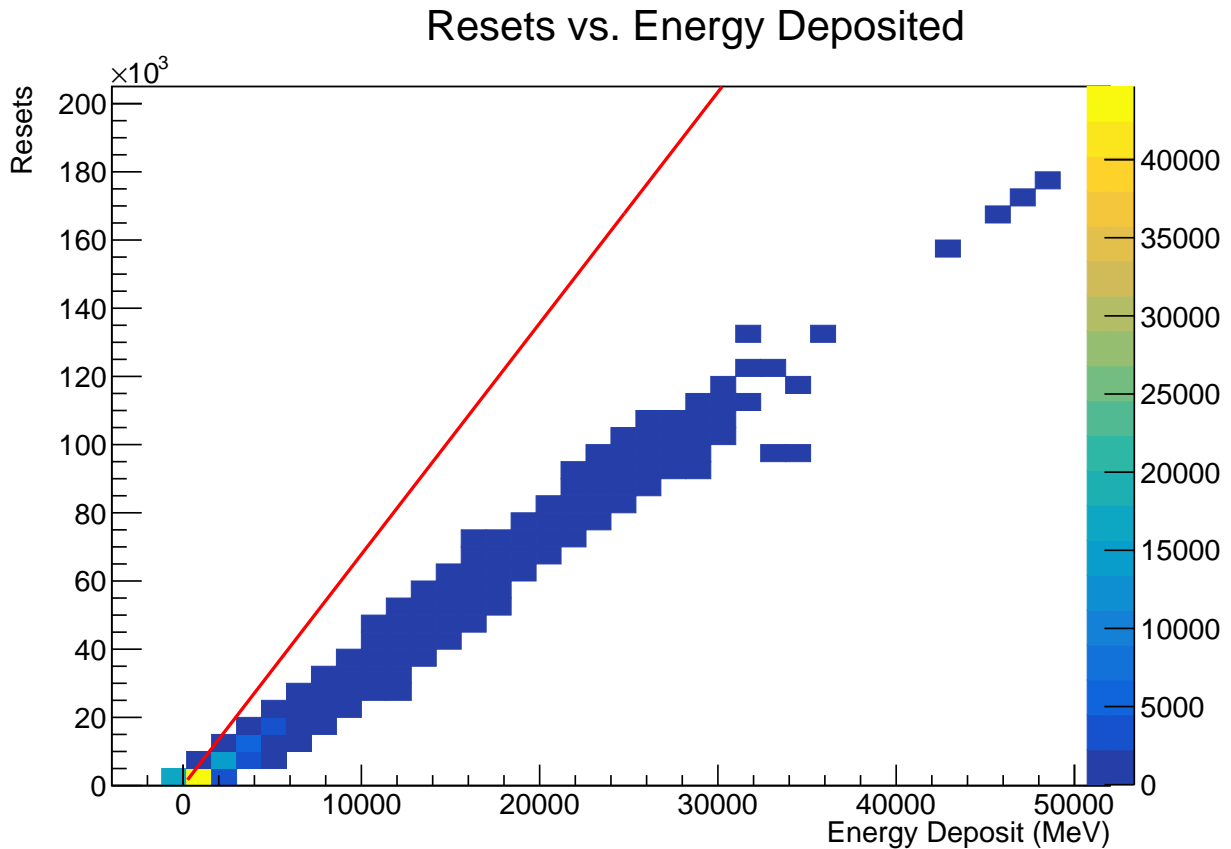
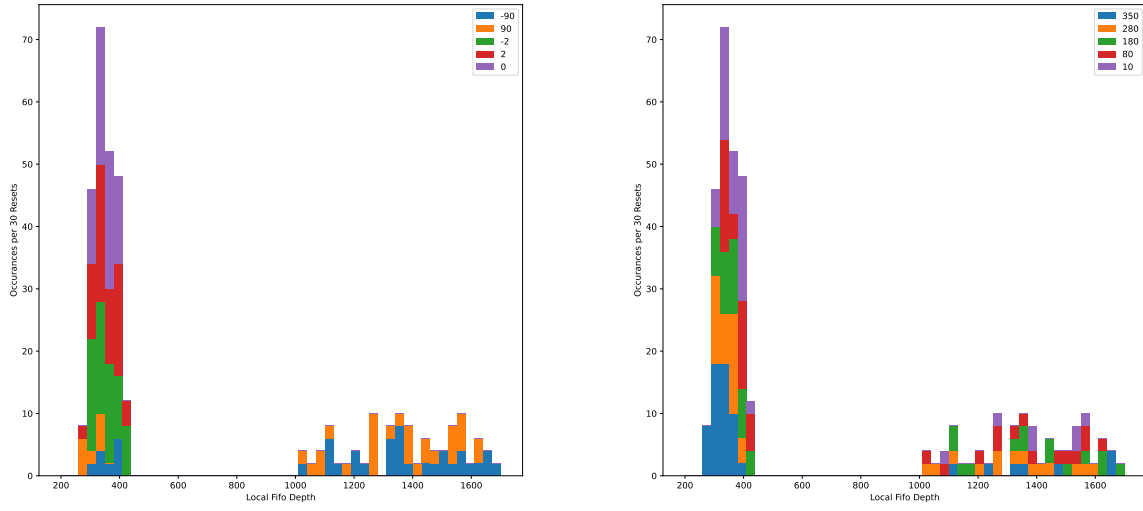


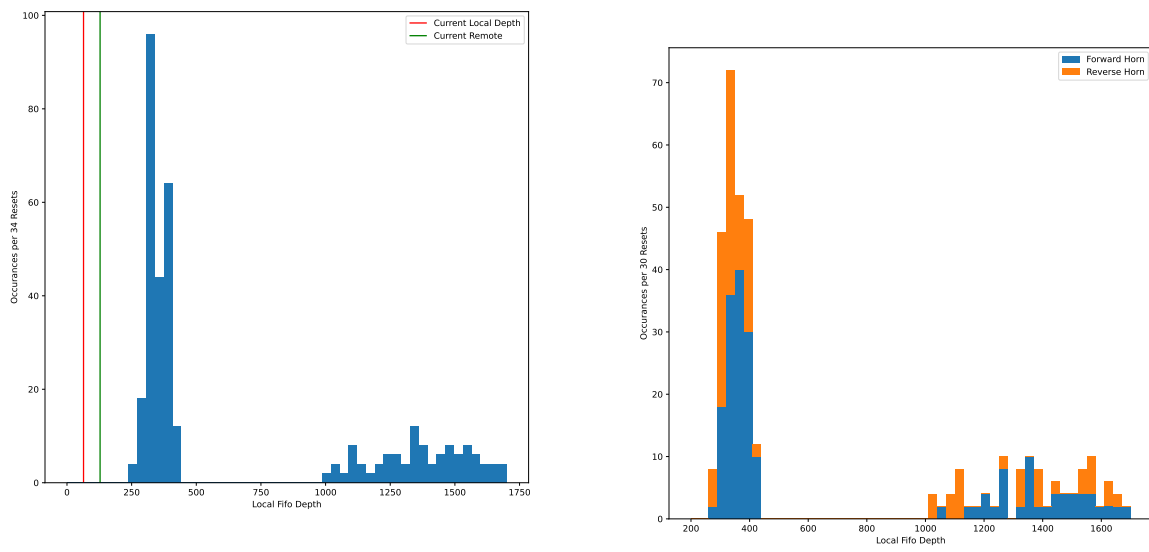
Figure 5.28: A relationship between the total number of resets detected in the APA and the energy deposited for ν_e interactions is shown. The solid red line indicates the maximum number of resets that could be measured for a given energy. The small distribution of energies below zero correspond to events that produced no resets. The energy deposited goes above the the threshold limit of 10 GeV. These events carry extra energy from additional leptons which are from pile-up at the DUNE-ND from the FNAL beam. These data are not included in the energy deposited analysis, or in the integrals as shown in Figure 5.21. These high energy deposit events are also not included in the FIFO depth analysis, since these events are beyond the energy range for oscillation measurements. These events are also removed from Figure 5.27.



((a)) Colored by θ_z direction.

((b)) Colored by Z-position

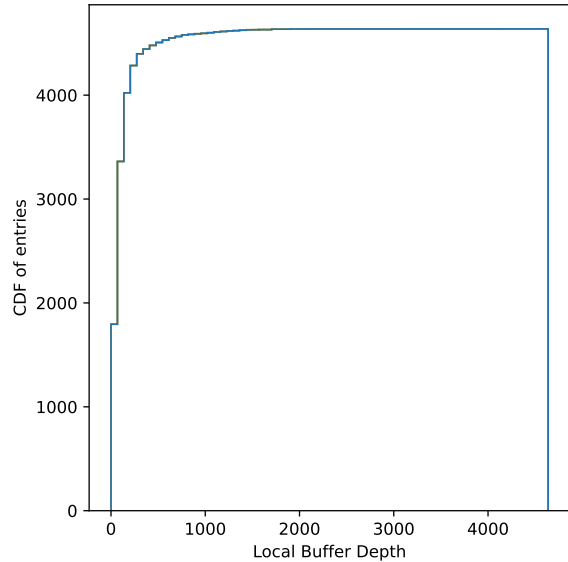
Figure 5.29: Comparison of Buffer depths as a function of energy for different parameters of θ_z and z-position. The most important result is shown in Plot-(A), which clearly indicates that only two different parameters account for the distribution of larger local FIFO depths. As expected, θ_z affects the localization of charge over individual ASICs which affect the local FIFO depth. Plot-(B) shows the distribution of resets indicated by different z-positions. Plot-(B) differs in that the second distribution of resets contains elements from each of the different z-positions.



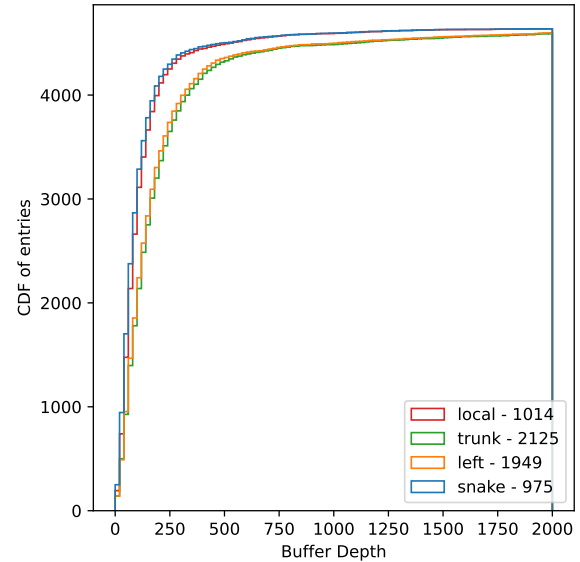
((a)) Comparison of all integrals to current prototype depths.

((b)) Colored by Z-position

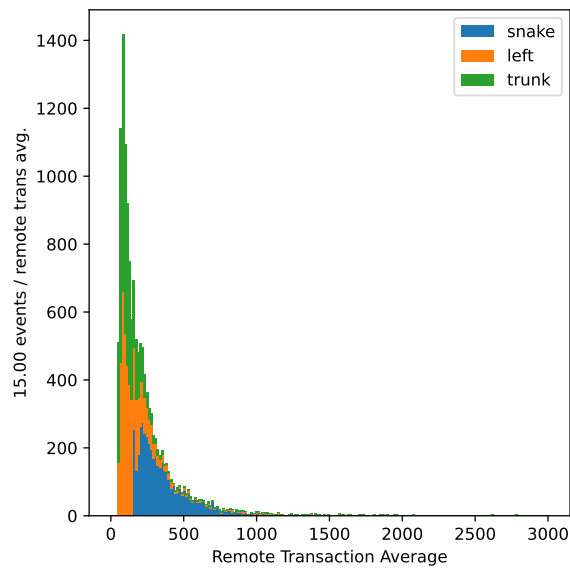
Figure 5.30: Comparison of Buffer depths as in incoming prototype and horn current direction from neutrino beam.



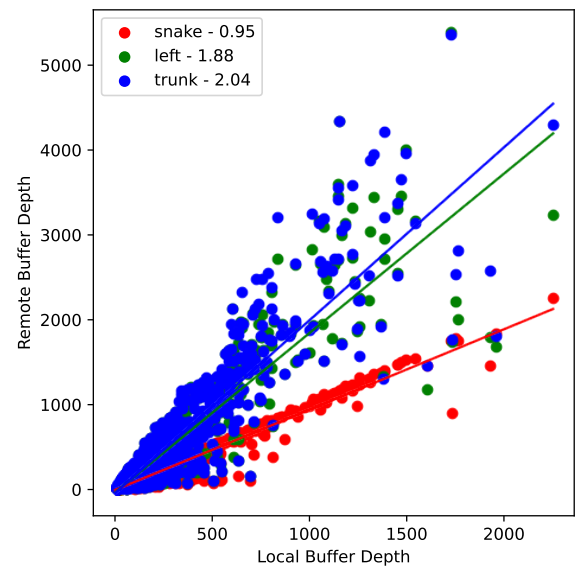
((a)) Network 1



((b)) remote stack

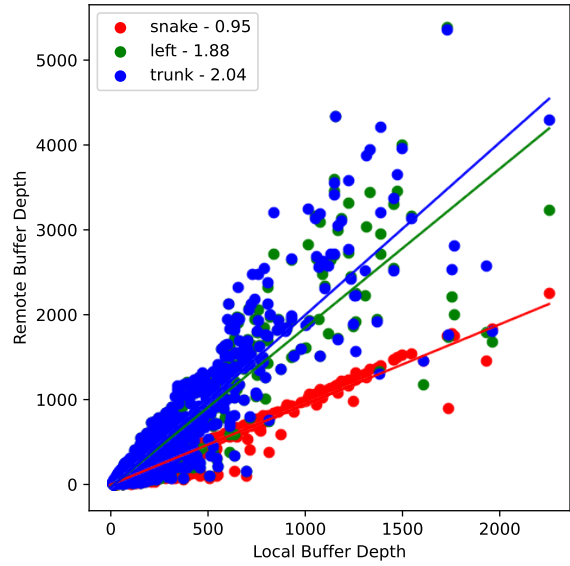


((c)) transact

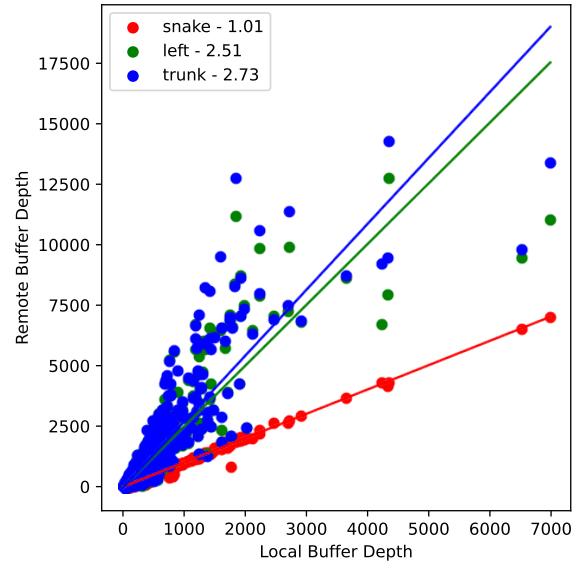


((d)) route fits

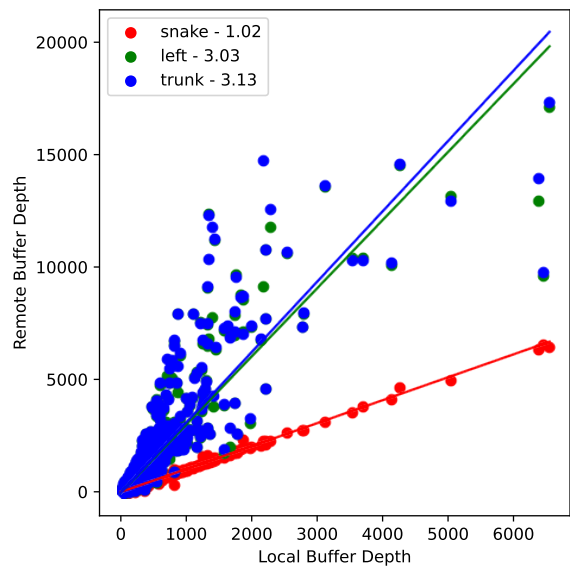
Figure 5.31: all of the data



((a)) 16 Sized Tile



((b)) 64 Sized tile



((c)) 140 Sized tile

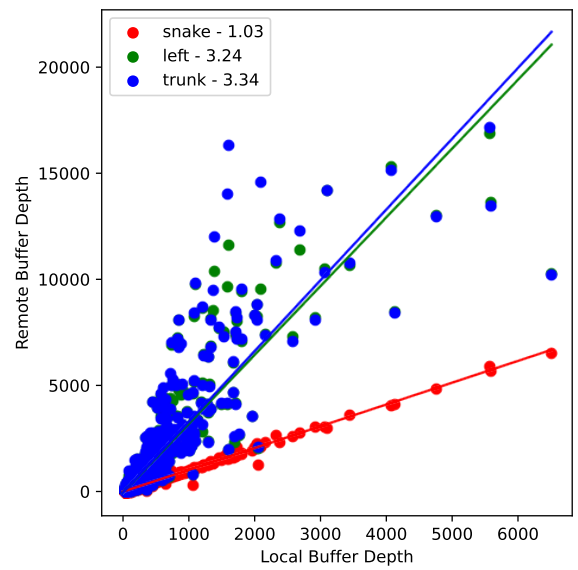
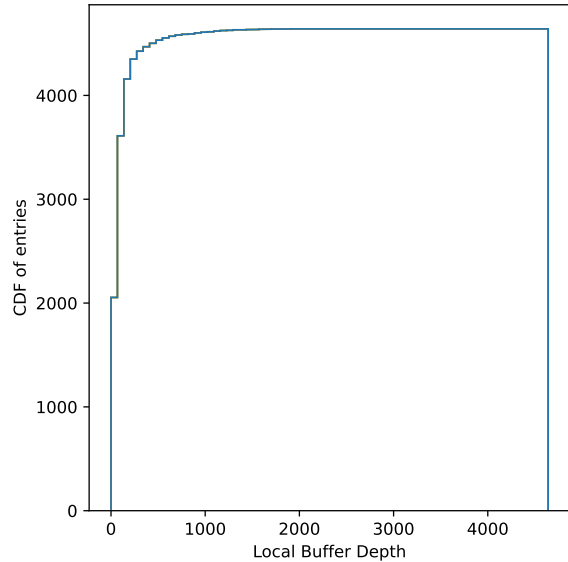
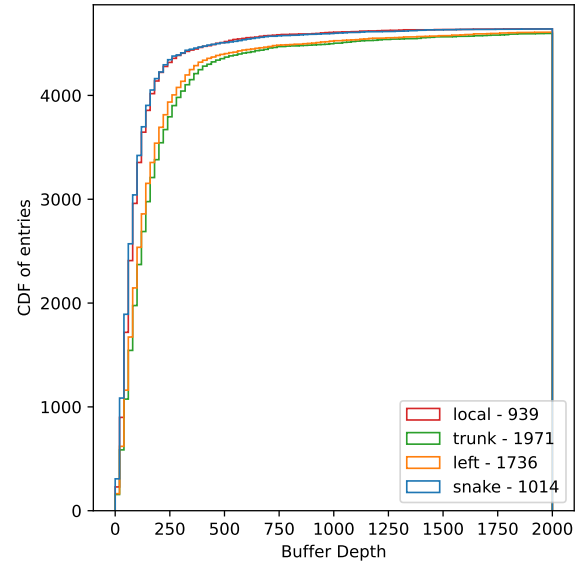


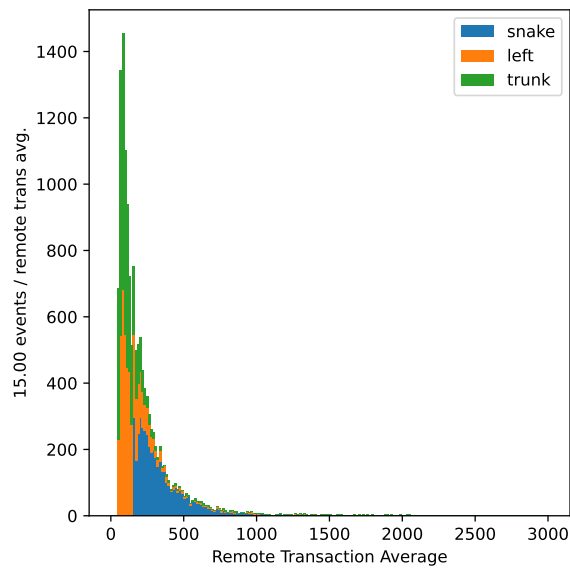
Figure 5.32: all of the data



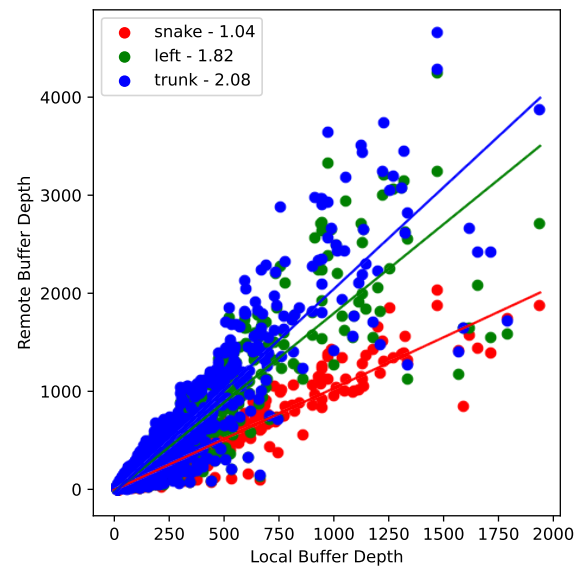
((a)) Network 1



((b)) remote stack

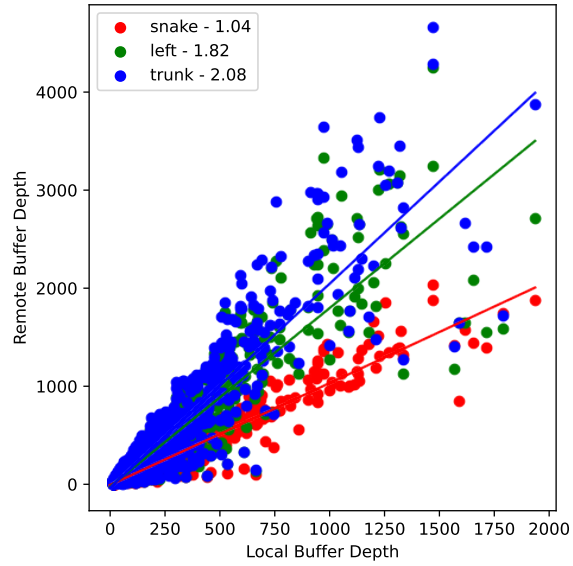


((c)) transact

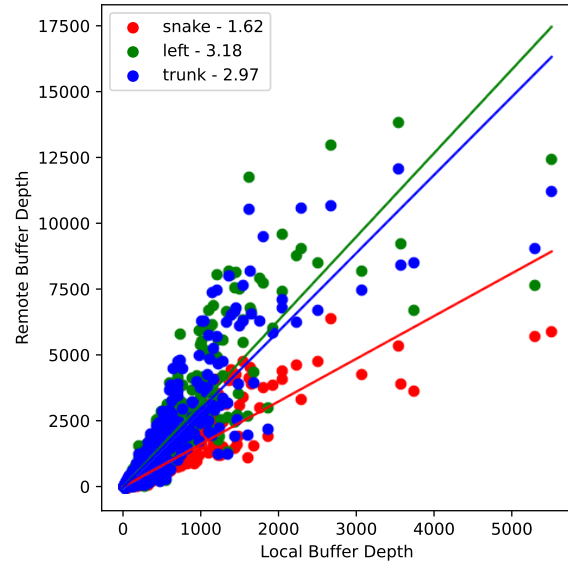


((d)) route fits

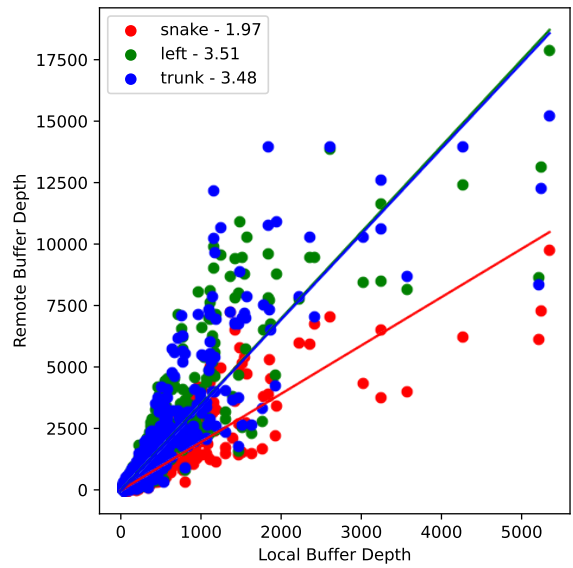
Figure 5.33: example plots for a 4×4 tile.



((a)) 16 Sized Tile



((b)) 64 Sized tile



((c)) 140 Sized tile

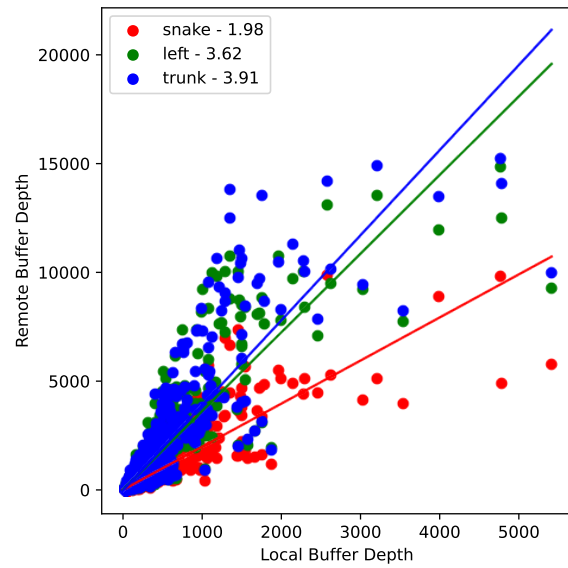


Figure 5.34: 16×16 tile of results

Chapter 6

SUMMARY AND OUTLOOK

Conclusions

The Future of Q-Pix

Recap of Qpix Requirements for DUNE APA here.

Recap of Qpix design concept testing within SAQ here.

Recap of QDB Results here

Recap of SAQ Results here

Recap of lessons learned on pixelated detectors

Discuss how combination of simulation / qdb / saq results motivate the next stage of development for QPix and incorporating the digital / analog ASICs for round two.

QPIX Layout: Integrator + Amplifier + Comparator

Size: 350um x 90 um

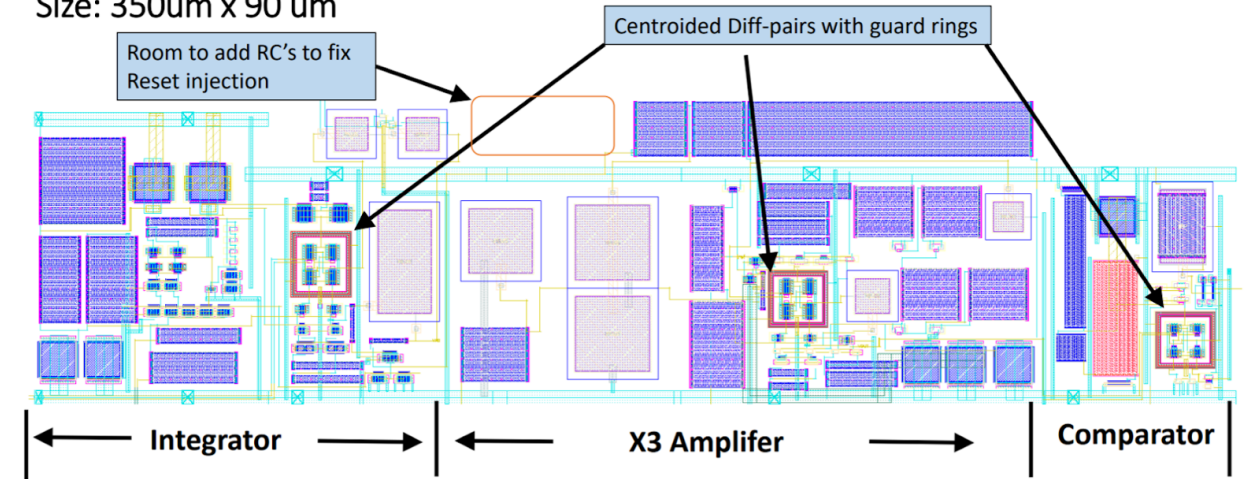


Figure 6.1: Full Schematic of the upcoming Q-Pix analog front-end ASIC.

BIBLIOGRAPHY

- ¹D. Dominguez, *Cern accelerating science*, 2015.
- ²J. L. Hewett et al., *Fundamental physics at the intensity frontier*, 2012.
- ³B. Abi et al., “Volume i. introduction to dune”, *Journal of Instrumentation* **15**, T08008 (2020).
- ⁴X. Qian and P. Vogel, “Neutrino mass hierarchy”, *Progress in Particle and Nuclear Physics* **83**, 1–30 (2015).
- ⁵R. Acciarri et al., *Long-baseline neutrino facility (lbnf) and deep underground neutrino experiment (dune) conceptual design report volume 1: the lbnf and dune projects*, 2016.
- ⁶D. Nygren and Y. Mei, *Q-pix: pixel-scale signal capture for kiloton liquid argon tpc detectors: time-to-charge waveform capture, local clocks, dynamic networks*, 2018.
- ⁷B. Abi et al., “Volume iv. the dune far detector single-phase technology”, *Journal of Instrumentation* **15**, T08010 (2020).
- ⁸M. Rooks, S. Abbaszadeh, J. Asaadi, M. Febbraro, R. W. Gladen, E. Gramellini, K. Hellier, F. M. Blaszczyk, and A. D. McDonald, *Development of a novel, windowless, amorphous selenium based photodetector for use in liquid noble detectors*, 2022.
- ⁹*Precision switched integrator transimpedance amplifier*, PDS-1329A, IVC 102 datasheet, Texas Instruments (1996).
- ¹⁰A. A. Abud et al., “Deep underground neutrino experiment (dune) near detector conceptual design report”, *Instruments* **5**, 10.3390/instruments5040031 (2021).
- ¹¹R. L. Workman and Others, “Review of Particle Physics”, *PTEP* **2022**, 083C01 (2022).
- ¹²*Liquid Argon Properties (Tables and Calculators) kernel description*, <https://lar.bnl.gov/properties/>, Accessed: 2023-01-04.
- ¹³I. Esteban, M. C. Gonzalez-Garcia, M. Maltoni, T. Schwetz, and A. Zhou, “The fate of hints: updated global analysis of three-flavor neutrino oscillations”, *Journal of High Energy Physics* **2020**, 178, 178 (2020).
- ¹⁴S. Kubota et al., “Enhanced low-energy supernova burst detection in large liquid argon time projection chambers enabled by q-pix”, *Phys. Rev. D* **106**, 032011 (2022).
- ¹⁵C. Andreopoulos et al., “The GENIE Neutrino Monte Carlo Generator”, *Nucl. Instrum. Meth. A* **614**, 87–104 (2010).

- ¹⁶B. Abi et al., *Deep underground neutrino experiment (dune), far detector technical design report, volume ii: dune physics*, 2020.
- ¹⁷S. L. Glashow, “Partial-symmetries of weak interactions”, *Nuclear Physics* **22**, 579–588 (1961).
- ¹⁸A. Salam and J. C. Ward, *Electromagnetic and weak interactions*, tech. rep. (IMPERIAL COLL OF SCIENCE and TECHNOLOGY LONDON (ENGLAND), 1964).
- ¹⁹S. Weinberg, “A model of leptons”, *Physical review letters* **19**, 1264 (1967).
- ²⁰M. Gell-Mann, “The Eightfold Way: A Theory of strong interaction symmetry”, [10 . 2172 / 4008239 \(1961\)](#).
- ²¹M. Gell-Mann, “A schematic model of baryons and mesons”, *Physics Letters* **8**, 214–215 (1964).
- ²²J. J. Aubert, U. Becker, P. J. Biggs, J. Burger, M. Chen, G. Everhart, P. Goldhagen, J. Leong, T. McCorriston, T. G. Rhoades, M. Rohde, S. C. C. Ting, S. L. Wu, and Y. Y. Lee, “Experimental observation of a heavy particle J ”, *Phys. Rev. Lett.* **33**, 1404–1406 (1974).
- ²³E. D. Bloom, D. H. Coward, H. Destaebler, J. Drees, G. Miller, L. W. Mo, R. E. Taylor, M. Breidenbach, J. I. Friedman, G. C. Hartmann, and H. W. Kendall, “High-Energy Inelastic e-p Scattering at 6° and 10° ”, *prl* **23**, 930–934 (1969).
- ²⁴M. Breidenbach, J. I. Friedman, H. W. Kendall, E. D. Bloom, D. H. Coward, H. Destaebler, J. Drees, L. W. Mo, and R. E. Taylor, “Observed Behavior of Highly Inelastic Electron-Proton Scattering”, *prl* **23**, 935–939 (1969).
- ²⁵S. W. Herb et al., “Observation of a dimuon resonance at 9.5 gev in 400-gev proton-nucleus collisions”, *Phys. Rev. Lett.* **39**, 252–255 (1977).
- ²⁶S. Abachi et al., “Observation of the top quark”, *Physical Review Letters* **74**, 2632–2637 (1995).
- ²⁷S. H. Neddermeyer and C. D. Anderson, “Note on the nature of cosmic-ray particles”, *Phys. Rev.* **51**, 884–886 (1937).
- ²⁸M. L. Perl et al., “Evidence for anomalous lepton production in $e^+ - e^-$ annihilation”, *Phys. Rev. Lett.* **35**, 1489–1492 (1975).
- ²⁹K. Kodama et al., “Observation of tau neutrino interactions”, *Physics Letters B* **504**, 218–224 (2001).
- ³⁰R. Brandelik et al., “Evidence for planar events in e+e- annihilation at high energies”, *Physics Letters B* **86**, 243–249 (1979).
- ³¹D. P. Barber et al., “Discovery of three jet events and a test of quantum chromodynamics at petra”, *Phys. Rev. Lett.* **43**, 830–833 (1979).

- ³²G. Arnison et al., “Experimental observation of isolated large transverse energy electrons with associated missing energy at $s=540$ gev”, *Physics Letters B* **122**, 103–116 (1983).
- ³³G. Arnison et al., “Experimental observation of lepton pairs of invariant mass around 95 gev/c² at the cern sps collider”, *Physics Letters B* **126**, 398–410 (1983).
- ³⁴P. Higgs, “Broken symmetries, massless particles and gauge fields”, *Physics Letters* **12**, 132–133 (1964).
- ³⁵G. Aad et al., “Observation of a new particle in the search for the standard model higgs boson with the atlas detector at the lhc”, *Physics Letters B* **716**, 1–29 (2012).
- ³⁶A. Airapetian et al., “ATLAS: Detector and physics performance technical design report. Volume 2”, (1999).
- ³⁷G. L. Bayatian et al., “CMS Physics: Technical Design Report Volume 1: Detector Performance and Software”, (2006).
- ³⁸T. Abe et al., *Belle ii technical design report*, 2010.
- ³⁹“Juno physics and detector”, *Progress in Particle and Nuclear Physics* **123**, 103927 (2022).
- ⁴⁰D. A. Glaser, “Some effects of ionizing radiation on the formation of bubbles in liquids”, *Phys. Rev.* **87**, 665–665 (1952).
- ⁴¹J. Chadwick, “The intensity distribution in the magnetic spectrum of beta particles from radium (B + C)”, *Verh. Phys. Gesell.* **16**, 383–391 (1914).
- ⁴²J. S. Chadwick, “Possible existence of a neutron”, *Nature* **129**, 312–312 (1932).
- ⁴³E. Fermi, “Versuch einer Theorie der β -Strahlen. I”, *Zeitschrift fur Physik* **88**, 161–177 (1934).
- ⁴⁴C. L. Cowan, F. Reines, F. B. Harrison, H. W. Kruse, and A. D. McGuire, “Detection of the free neutrino: a confirmation”, *Science* **124**, 103–104 (1956).
- ⁴⁵G. Danby, J.-M. Gaillard, K. Goulian, L. M. Lederman, N. Mistry, M. Schwartz, and J. Steinberger, “Observation of high-energy neutrino reactions and the existence of two kinds of neutrinos”, *Phys. Rev. Lett.* **9**, 36–44 (1962).
- ⁴⁶F. P. An et al., “Observation of electron-antineutrino disappearance at daya bay”, *Phys. Rev. Lett.* **108**, 171803 (2012).
- ⁴⁷Q. R. Ahmad et al., “Direct evidence for neutrino flavor transformation from neutral-current interactions in the sudbury neutrino observatory”, *Phys. Rev. Lett.* **89**, 011301 (2002).

- ⁴⁸M. A. Acero et al., “First measurement of neutrino oscillation parameters using neutrinos and antineutrinos by nova”, [Phys. Rev. Lett. **123**, 151803 \(2019\)](#).
- ⁴⁹K. Abe et al., “Indication of electron neutrino appearance from an accelerator-produced off-axis muon neutrino beam”, [Phys. Rev. Lett. **107**, 041801 \(2011\)](#).
- ⁵⁰J. K. Ahn et al., “Observation of reactor electron antineutrinos disappearance in the reno experiment”, [Phys. Rev. Lett. **108**, 191802 \(2012\)](#).
- ⁵¹S. Fukuda et al., “Determination of solar neutrino oscillation parameters using 1496 days of super-kamiokande-i data”, [Physics Letters B **539**, 179–187 \(2002\)](#).
- ⁵²K. Eguchi et al., “First results from kamland: evidence for reactor antineutrino disappearance”, [Phys. Rev. Lett. **90**, 021802 \(2003\)](#).
- ⁵³Y. Abe et al., “Indication of reactor $\bar{\nu}_e$ disappearance in the double chooz experiment”, [Phys. Rev. Lett. **108**, 131801 \(2012\)](#).
- ⁵⁴R. Davis, D. S. Harmer, and K. C. Hoffman, “Search for neutrinos from the sun”, [Phys. Rev. Lett. **20**, 1205–1209 \(1968\)](#).
- ⁵⁵G. Charpak, R. Bouclier, T. Bressani, J. Favier, and C. Zupancic, “The Use of Multiwire Proportional Counters to Select and Localize Charged Particles”, [Nucl. Instrum. Meth. **62**, 262–268 \(1968\)](#).
- ⁵⁶J. N. Marx and D. R. Nygren, “The time projection chamber”, [Physics Today **31**, 46–53 \(1978\)](#).
- ⁵⁷E. Aprile et al., “The XENON1t dark matter experiment”, [The European Physical Journal C **77**, 10.1140/epjc/s10052-017-5326-3 \(2017\)](#).
- ⁵⁸C. Rubbia, *The liquid-argon time projection chamber: a new concept for neutrino detectors*, tech. rep. (1977).
- ⁵⁹R. Acciarri et al., “Demonstration of mev-scale physics in liquid argon time projection chambers using argoneut”, [Phys. Rev. D **99**, 012002 \(2019\)](#).
- ⁶⁰R. Acciarri et al., “Design and construction of the microboone detector”, [Journal of Instrumentation **12**, P02017 \(2017\)](#).
- ⁶¹R. Acciarri et al., “The liquid argon in a testbeam (lariat) experiment”, [Journal of Instrumentation **15**, P04026 \(2020\)](#).
- ⁶²A. Friedland and S. W. Li, “Understanding the energy resolution of liquid argon neutrino detectors”, [Phys. Rev. D **99**, 036009 \(2019\)](#).

- ⁶³F. Arneodo, *The icarus experiment, a second-generation proton decay experiment and neutrino observatory at the gran sasso laboratory*, 2001.
- ⁶⁴K. Abe et al., “Search for proton decay via $p \rightarrow e^+\pi^0$ and $p \rightarrow \mu^+\pi^0$ in 0.31 megaton · years exposure of the super-kamiokande water cherenkov detector”, *Phys. Rev. D* **95**, 012004 (2017).
- ⁶⁵P. Nath and R. Arnowitt, “Limits on photino and squark masses from proton lifetime in supergravity models”, *Phys. Rev. D* **38**, 1479–1484 (1988).
- ⁶⁶H.-K. Proto-Collaboration et al., *Hyper-kamiokande design report*, 2018.
- ⁶⁷G. M. Fuller, R. W. Mayle, J. R. Wilson, and D. N. Schramm, “Resonant Neutrino Oscillations and Stellar Collapse”, *apj* **322**, 795 (1987).
- ⁶⁸K. Abe et al., “Measurements of neutrino oscillation in appearance and disappearance channels by the t2k experiment with 6.6×10^{20} protons on target”, *Phys. Rev. D* **91**, 072010 (2015).
- ⁶⁹B. Pontecorvo, “Inverse beta processes and nonconservation of lepton charge”, *Zh. Eksp. Teor. Fiz.* **34**, 247 (1957).
- ⁷⁰Z. Maki, M. Nakagawa, and S. Sakata, “Remarks on the Unified Model of Elementary Particles”, *Progress of Theoretical Physics* **28**, 870–880 (1962).
- ⁷¹L. Wolfenstein, “Neutrino oscillations in matter”, *Phys. Rev. D* **17**, 2369–2374 (1978).
- ⁷²A. Y. Smirnov, “The msw effect and matter effects in neutrino oscillations”, *Physica Scripta* **2005**, 57–64 (2004).
- ⁷³P Sadowski, B Radics, Ananya, Y Yamazaki, and P Baldi, “Efficient antihydrogen detection in antimatter physics by deep learning”, *Journal of Physics Communications* **1**, 025001 (2017).
- ⁷⁴P. Sadowski and P. Baldi, “Deep learning in the natural sciences: applications to physics”, in Braverman readings in machine learning (2017).
- ⁷⁵D. Dwyer, M. Garcia-Sciveres, D. Gnani, C. Grace, S. Kohn, M. Kramer, A. Krieger, C. Lin, K. Luk, P. Madigan, C. Marshall, H. Steiner, and T. Stezelberger, “Larpix: demonstration of low-power 3d pixelated charge readout for liquid argon time projection chambers”, *Journal of Instrumentation* **13**, P10007 (2018).
- ⁷⁶J. Asaadi, M. Auger, A. Ereditato, D. Goeldi, R. Hänni, U. Kose, I. Kreslo, D. Lorca, M. Luethi, C. R. von Rohr, J. Sinclair, F. Stocker, C. Tognina, and M. Weber, “A pixelated charge readout for liquid argon time projection chambers”, *Journal of Instrumentation* **13**, C02008 (2018).
- ⁷⁷B. Abi et al., “Volume iii. dune far detector technical coordination”, *Journal of Instrumentation* **15**, T08009 (2020).

- ⁷⁸L. Paulucci and on behalf of DUNE collaboration, “The dune vertical drift photon detection system”, *Journal of Instrumentation* **17**, C01067 (2022).
- ⁷⁹J. Joshi and X. Qian, *Signal processing in the microboone larpc*, 2015.
- ⁸⁰S. Agostinelli et al., “Geant4—a simulation toolkit”, *Nuclear Instruments and Methods in Physics Research Section A: Accelerators, Spectrometers, Detectors and Associated Equipment* **506**, 250–303 (2003).
- ⁸¹Zybo z7 board reference manual, Zybo Z7 Reference Manual, Digilent (https://digilent.com/reference/_media/reference/zybo-z7/zybo-z7_rm.pdf).
- ⁸²Y. Li, T. Tsang, C. Thorn, X. Qian, M. Diwan, J. Joshi, S. Kettell, W. Morse, T. Rao, J. Stewart, W. Tang, and B. Viren, “Measurement of longitudinal electron diffusion in liquid argon”, *Nuclear Instruments and Methods in Physics Research Section A: Accelerators, Spectrometers, Detectors and Associated Equipment* **816**, 160–170 (2016).
- ⁸³Lattice, *Ice40 ultraplus family data sheet*, lattice ice40up fpga data sheet, Lattice Semiconductor (<https://www.latticesemi.com/-/media/LatticeSemi/Documents/DataSheets/iCE/iCE40-UltraPlus-Family-Data-Sheet.ashx>).
- ⁸⁴N. None, “Study of reconstructed 39ar beta decays at the microboone detector”, [10.2172/1573057](https://doi.org/10.2172/1573057) (2018).
- ⁸⁵J. Shi, *Studies of radiological backgrounds in the dune far detector and the sensitivity to the solar neutrino day-night effect using the photon-detector system*, 2019.
- ⁸⁶R. Acciarri et al., “A study of electron recombination using highly ionizing particles in the ArgoNeuT Liquid Argon TPC”, *Journal of Instrumentation* **8**, P08005, P08005 (2013).
- ⁸⁷C. Marshall, K. McFarland, and C. Wilkinson, “Neutrino-electron elastic scattering for flux determination at the dune oscillation experiment”, *Physical Review D* **101**, [10.1103/PhysRevD.101.032002](https://doi.org/10.1103/PhysRevD.101.032002) (2020).
- ⁸⁸A. Galindo-Tellez, K. Keefe, E. Adamek, E. Brubaker, B. Crow, R. Dorrill, A. Druetzler, C. J. Felix, N. Kaneshige, J. G. Learned, J. J. Manfredi, K. Nishimura, B. Pinto Souza, D. Schoen, and M. Sweany, “Design and calibration of an optically segmented single volume scatter camera for neutron imaging”, *Journal of Instrumentation* **16**, P04013, P04013 (2021).

Appendix A

SVSC OS1

the work in this subsection details the work and results of [88].

Appenidx B

SVSC OS2

Put OS2 work here